SCUOLA DI DOTTORATO
UNIVERSITÀ DEGLI STUDI DI MILANO-BICOCCA

Department of Material Science

PhD program in Material Science and Nanotechnology Cycle XXXIII

QUANTUM ENGINEERING AT THE SINGLE PHOTON LEVEL

Surname: Guardiani Name: Antonio

Registration number: 835461

Tutor: Dr. Fognini Andreas

Supervisor: Prof. Sanguinetti Stefano

Coordinator: Prof. Bernasconi Marco

ACADEMIC YEAR 2020

CONTENTS

ACKNOWLEDGEMENTS

First of all, I want to thank Andreas for the incredible support, patience and tips given all along my experience as PhD fellow. It was great to give you a buzz whenever needed and find out that the solutions were often closer than I initially had though. So many things I have learned and so many others I still hope to discuss together. The amount of panettoni I still owe you is countless.

Next in line is Sander the great, the tsar of SQ. Thanks for letting me part of this family and give me the chance to work in such an exciting environment where a lot of things happen.

Of course, I cannot miss to thank all D-team and colleagues at SQ. It was great to work with you, helping each other whenever possible. Thanks to Micha for your insights about programming, sometimes you pulled my chestnuts out of the fire. Plus, I cannot forget all the "bro" love running on the 5th floor. Thanks to Monique and Annalisa to have backed me up when I was running out of time. I will try to make up for it. Special thanks to Ronan, it is great to ask for advice from the only other PhD "sur le marché". It was nice to be part of your experiments at the beginning of this adventure, from you I learned a lot of "dirty" hands-on work in the lab. I must admit that the amazing music you always chose was helping a lot during the "dark" life in the basement. A big thank to Gabriele, you are the one who got my application and trusted me first.

Thanks to Iman and Jin, the TU boys, for the great collaborations and the big amount of data shared with me.

I want to thank Val and Klaus for the warm welcome in Stockholm. It was very interesting to join your team and help out in the lab. Thanks to Lukas and Katha for showing me around and teach me tips on spectroscopy, cool optics and programming. It was amazing to see you always strive for perfection and never back down. A special mention goes to Samuel, it was fun to haunt you from Delft during the pandemic, maybe less fun for you. We managed to get some interesting stuff done, and I hope that my work will serve for your future experiments. We made it with the bloody card! Last, I want to thank also Artur, with his Siberian wisdom, you were a really great company during that time.

A huge thank goes to the all 4Photon community that made this project possible and prof. Sanguinetti who dealt with all the in-house matters.

I want to thank all my friends from home. Despite distance and years, every time I am back it feels like I never left. Thanks to the wizard of CAD Andrea Ripari for the consulting in 3D rendering. And I want to thank all my friends made in Rome. It is not so easy to catch up all together anymore, but each summit still feels like partying after exams.

I want to thank my family that has always supported me all along. This piece of paper is just a small proof of all the good work that you have done with me.

Above everyone I want to thank Laura, with you the time has passed fast, maybe too fast but this is what they say when you enjoy the ride.

SUMMARY

Advances in the field of quantum computation could disclose powerful means applicable in many areas of research such as life sciences and metrology among others. However, concerning the field of telecommunication, the so-called “quantum supremacy” in computational power provided by quantum computers poses a huge threat to classical encryption schemes making the transmission of sensitive data unsafe. Progress in Quantum Key Distribution has demonstrated to solve the issue of eavesdropping by using photon qubits but only in short-range transfer. In order to enhance the reliability and range of the quantum communication protocols, the source of photons have to comply with stringent requirements like high single-photon purity, near-to-perfect entanglement, high brightness and high operation rate.

With this thesis we have presented and confirmed a model that predicts consistently the entanglement evolution for an AlGaAs quantum dot. This system seems not to suffer from any dephasing mechanism if pumped with two-photon resonant excitation. The experimental results point out that the behavior of these solid-state emitters only depend on the exciton precession, especially considering that AlGaAs Qdots do possess significant nuclear spin. Thus, we could infer that the interaction between the charge carriers involved in the emission and the nuclei is not a relevant dephasing mechanism within the time of the exciton radiative decay. We show that, although no dephasing mechanism occurs for the quantum dot under investigation, reaching a steady concurrence level of one during the whole radiative decay, that indicates perfect entanglement, does still remain a challenge.

In light of these findings, we present here two possible workarounds. First, by improving the time resolution of the detection system we aimed at increasing the measurable degree of entanglement, because, according to the theoretical model, the concurrence is lowered by the timing jitter of the detection system. To this end, we have reported the realization of a new generation of cryogenic amplifiers coupled to superconducting nanowire single photon detectors that greatly improve the jitter performance of the detection system.

However, since the physical time resolution will always be finite and never reach zero, an entanglement measurement can never yield a steady value of one for the concurrence over the whole radiative lifetime of the quantum dot. This is why we introduce a second research direction which consists of engineering the properties of the exciton and biexciton emission by acting on their frequencies. This has the major benefit to avoid difficult post-growth fine-structure splitting compensation techniques. Here we present the idea of engineering single photons through sawtooth phase modulation and stress on the point that this technique is a valuable alternative to achieve fine-structure compensation. The thesis gives a preliminary evidence of feasible compensation with current commercial phase modulation technology by performing frequency translation experiments on a laser source. The measured spectra show that sawtooth phase modulation

can reach the target despite the technological limitations, but further improvements are needed. We explain one method to boost sawtooth phase modulation, namely with the use of the well-established phase-locked loop technology which, through signals synchronization, avoids the rise of undesired spurious components.

Despite the necessary development in quantum repeater technology, with this work we foresee the feasibility in the realization of a quantum photonic infrastructure where the photons are fully entangled enabling the exchange of photon qubits in long-range quantum communication.

RIASSUNTO

I progressi nel campo del calcolo quantistico potrebbero fornire rilevanti applicazioni in molte aree di ricerca come la biologia e la metrologia su tutte. Tuttavia, per quanto riguarda il campo delle telecomunicazioni, la cosiddetta "supremazia quantistica" nella potenza di calcolo del computer quantistico rappresenta un'enorme minaccia per gli schemi di crittografia classici, mettendo a rischio la riservatezza di dati sensibili. I progressi nella distribuzione delle chiavi quantistiche hanno dimostrato di poter risolvere il problema dell'*eavesdropping* utilizzando *qubit* di fotoni ma nel solo caso di trasferimento a corto raggio. Per migliorare l'affidabilità e il raggio dei protocolli di comunicazione quantistica, la sorgente dei fotoni deve soddisfare requisiti rigorosi come l'elevata purezza di singolo fotone, l'*entanglement* quasi perfetto, l'elevata luminosità e l'elevata velocità di funzionamento.

Con questa tesi abbiamo presentato e confermato un modello che predice in maniera consistente l'evoluzione dell'*entanglement* per un quantum dot di AlGaAs che sembra non soffrire di alcun meccanismo di sfasamento se pompato con un'eccitazione risonante a due fotoni. I risultati sperimentali sottolineano che il comportamento di questi emettitori a stato solido dipende solo dalla precessione degli eccitoni, soprattutto considerando che i quantum dots di AlGaAs possiedono uno spin nucleare significativo. Pertanto, si potrebbe dedurre che l'interazione tra i portatori di carica coinvolti nell'emissione e i nuclei non sia un meccanismo di sfasamento rilevante entro il tempo di decadimento radiativo dell'eccitone. Inoltre, in questo manoscritto si dimostra che, sebbene non si verifichi alcun meccanismo di sfasamento nel quantum dot in esame, il raggiungimento di un livello di concorrenza pari a uno, sinonimo di *entanglement* perfetto, rimane un compito difficile.

Alla luce di questi risultati, presentiamo due possibili soluzioni. Innanzitutto, il miglioramento della risoluzione temporale del sistema di rilevamento che è volto ad aumentare il grado di *entanglement*. Questo perchè, secondo il modello teorico, il valore della concorrenza è degradato dalla risoluzione temporale del sistema di rilevamento. A tal proposito riportiamo la realizzazione di una nuova generazione di amplificatori criogenici accoppiati a rivelatori a singolo fotone di nanofili superconduttori che migliorano notevolmente le prestazioni di risoluzione temporale del sistema di rilevamento.

Tuttavia, poiché la risoluzione temporale dello strumento sarà sempre finita e non raggiungerà mai lo zero, una misurazione di *entanglement* non potrà mai produrre un valore costante di concorrenza pari a uno durante l'intero decadimento radiativo del quantum dot. Per questo motivo, si introduce una seconda direzione di ricerca che consiste nell'ingegnerizzare le proprietà dell'emissione eccitonica e bieccitonica agendo sulle frequenze dei fotoni. Tale approccio consente di evitare difficili tecniche di compensazione post-crescita. L'idea centrale è di ingegnerizzare i singoli fotoni attraverso la modulazione di fase a dente di sega per compensare lo *splitting* di struttura fine. La tesi fornisce una prova preliminare della possibile compensazione con la tecnologia

di modulazione di fase già disponibile a livello commerciale riportando esperimenti di traslazione di frequenza su una sorgente laser. Gli spettri misurati mostrano che la modulazione di fase a dente di sega può raggiungere l'obiettivo nonostante i limiti tecnologici che necessitano di ulteriori miglioramenti. A tal fine si presenta un metodo per migliorare modulazione di fase utilizzando la consolidata tecnologia di *phase-locked loop*, che attraverso la sincronizzazione dei segnali, può evitare il sorgere di contributi spuri.

Nonostante lo sviluppo necessario nel campo dei ripetitori quantistici, con questo lavoro si intravede la possibilità di realizzare un'infrastruttura fotonica quantistica nella quale i fotoni sono completamente *entangled* consentendo lo trasferimento di *qubits* nella comunicazione a lungo raggio.

1

INTRODUCTION

The striking discoveries of quantum physics over the past century have shaped the future of our society by paving the way to numerous inventions that have revolutionized the contemporary world. The quantum description of the nanoscopic world exceeds the classical frame and have pushed a constant improvement in the field of electronics and optics among many others. The great example is the invention of the transistor in 1947 by John Bardeen, Walter Brattain, and William Shockley, that was the foundation of what would become the future semiconductor industry. With the fast-paced developments in chemical deposition and lithography techniques, the realization of faster, more reliable and cheaper components became possible, leading to the era of powerful miniaturized computers. Nowadays, fundamental technologies such as lasers, radio-frequency devices and fast computers are needed not only in cutting-edge research fields-but are already deployed in loads of industrial applications used in everyday life.

However, new technologies bring new challenges and scientists are now committed in the quest of a new device, the "quantum computer". The classical bit, the basic unit of information in computing and digital communication, is outperformed by another type of bit, the Quantum bit or "Qbit". In classical computation, a bit can take values of 0 or 1 and the calculations, in binary system, can only be performed sequentially. The breakthrough with Qbits comes because this special bit can simultaneously take the values of its classical counterpart at the same time and the computation process cannot be explained classically. This occurs again thanks to three quantum physical processes: superposition, interference, and entanglement.

Let's give a hint of what quantum computing could disclose by considering a system of N qubits. These N qubits represent a state given by the superposition of all of them. This physical mechanism enables to retain information for an amount equal to 2^N classical bits since the system can be simultaneously in a state of all the different classical configurations.

This feature enables high computational power and the realization of quantum algorithms in the foreseeable future which pose, for example, a great menace to classical encryption schemes that use standard public-key cryptography. However, this is where

quantum communication comes into play, which protects the information channel by exploiting the special laws of quantum physics like for instance quantum entanglement. Nowadays, sharing data among computers demands high security level which relies on the Public Key Infrastructure (PKI). PKI delivers and revoke digital certificates and each user in the network is identified with its own crypto-graphic key. Unfortunately, PKI is not always secure to cyber-attacks and as data is shared among devices, hackers can intercept the keys and decrypt the data, without the legitimate users noticing the breach.

Latest advancement in Quantum key distribution protocols (QKD) have been proven effective against these threats [1, 2] by using quantum entanglement correlation as a mean to reveal the presence of a hacker. This is because the process of eavesdropping perturbs the quantum state of the single photons shared over the network, making the infringement visible. In case the level of eavesdropping is below a certain threshold, a classical key can then be produced and transferred securely to the receiver, and safe communication of sensitive data can be established.

Nevertheless, the working examples of QKD around the world are restricted to the case where communication is short-haul because of several limitations. In fact, even if we can accomplish longer distance communication in the telecom C-band of optical fibers, where the attenuation is minimized, single photons will eventually not reach the end terminal - a complete loss of information. This limitation is exacerbated by the fact that single photon states cannot be amplified nor copied [3] and that creating photon emitters at telecom C-band is a very difficulty task. A possible workaround to C-band attenuation was proposed by interfacing the optical network with quantum memories/repeaters based on atomic vapor systems [4, 5]. This solution sets several stringent requirements on the single photon source in order to effectively store the information state carried by the photon into the gas of atoms [6, 7] such as the wavelength tunability of the emitted photons that also need to be transform-limited and match the atomic transition.

Additional challenges concern the realization of a single photon source capable of generating photons that are highly pure and highly entangled to allow for quantum key distribution protocols. Moreover, high photon rate is desired to enable faster quantum communication.

All these requirements have been investigated for many photon sources of entangled photons be them either non-linear optical process or photonic materials. At the early stage of this research field, spontaneous parametric down-conversion have provided good entanglement quality photons but the non-linear process that works thanks to a pump beam, suffers from a trade-off between efficiency and purity. This forces to work with a weaker pump beam which results in lower photon rates. However, other classes of emitters have entered the scene to lift the limitation of the spontaneous parametric down-conversion process. These can be atoms [8], molecules [9], defects in the solid state [10], and quantum dots [11]. They also bring the advantage of triggering the emission of a single photon on-demand, instead of generating them randomly as in the case of parametric down-conversion

The remarkable developments in semiconductor technology and post-growth engineering together with improvements in optical excitation schemes have led to proof of principle experiments in QKD using quantum dots. However, Qdots present one fun-

damental disadvantage, namely their fine-structure splitting which is represented by a random phase factor in the two-photon qubit state. This additional phase factor spoils the degree of measurable entanglement in time-integrated measurements [12, 13]. Until now, researchers have come up with a variety of approaches to minimize the impact of the fine-structure splitting onto the entanglement level with finer growth [14–16] and post-growth techniques [17–19] but also post-selection with spectral filtering [20] and timing selection [12].

Even if the fine-structure splitting has been incredibly reduced reaching values of less than a 1 μeV, the entanglement quality is anyway considerably decreased, and further reducing the fine-structure splitting becomes a very challenging task. Moreover, post-selection methods in frequency domain or time domain decrease significantly the rate of usable photons in quantum communication. Last but not least, all the available quantum dots on a sample do not show the same fine-structure splitting posing severe restriction on selection range of "good quality" quantum dots. For instance, quantum dots with large fine-structure splitting cannot be used even if they may have the advantage to emit in the telecom C-band

Novel fine-structure splitting compensation schemes based on electro-optical modulators may solve these problems pushing the measurable entanglement towards unity for all quantum dots on a sample. Several methods were proposed to achieve frequency translation [21–23] and all face some limitations in terms of collection efficiency and arbitrariness in the amount of compensation. Wang [24] proposed a theoretical scheme based on a linear voltage sweep that is infinitely long but it seems impractical due to the large electrical bandwidth needed to generate the radio-frequency signal. Two different but complementary solutions can though represent a workaround. These are sawtooth phase modulation [25] and fast rotating $\lambda/2$-waveplates [26, 27]. These methods, that can be implemented using current electro-optical modulators, achieve high conversion efficiency up to 95% [28] thanks to the great transparency of the electro-optic crystal, and it is only hindered by the coupling of the light between the optical fiber and the integrated waveguide. The incredible advantage is that the amount of compensation can be arbitrarily decided by the user.

The good performance of the QKD protocol does not only concern the generation of light with suitable properties, but does also depend strongly on the detection of these particles. The deployment of superconducting single photon detectors, that enable high detection efficiency with low dark count rates [29], is crucial to reach the lowest key error rate. Moreover, the high time resolution, in the order of tens of picoseconds, allows for a very fine time stamping of the photon arrival. If we could combine these properties with high count rate capabilities for increased payload capacity, this technology could disclose fast quantum communication at least for the receiving end. Since the discovery of photon revelation properties of superconducting materials by Gol'tsman in 2001 [30], this has become a very active field of research with impact on a lot of applications not only restricted to quantum information.

1

1.1. STRUCTURE OF THE THESIS

Chapter 2 describes the nature of photon entanglement from quantum dots under two type of excitation schemes: resonant and non-resonant. The experimental results reported show that the dephasing of the quantum state under resonant excitation becomes negligible. The main focus of the chapter is to discuss why perfect photon entanglement can be reached if the time resolution of the detection system is high even in the presence of fine-structure splitting and propose a model to describe the entanglement evolution probed during time-resolved measurements. This chapter points out that making a fully entangled photon pair becomes more a measurement challenge than a mere growth challenge. Results obtained with latest generation superconducting single photon detectors confirm this thesis and verifies the model proposed.

Chapter 3 presents the new generation of cryo-amplifiers designed at Single Quantum B.V. designed to enhance time resolution of superconducting single photon detectors and increase the degree of measurable entanglement for a quantum dot source. Electrical noise measurements, due to the decreased thermal motion of the carriers in the circuit, demonstrate that the cryogenic amplification improves the detection resolution up to 60% compared to the room temperature readout scheme. A simulation that highlights the impact of enhanced time resolution on the entanglement evolution will be shown at the end of the chapter.

Chapter 4 proves the feasibility of the fine-structure splitting compensation scheme based on sawtooth phase modulation. Experimental results demonstrate efficient photon frequency shift with a radio-frequency signal generated by using an affordable fast digital-to-analog converter coupled to a pattern generator. The chapter shows also simulations that match the experimental behaviour of the electro-optic modulator. Finally, the technological limitations are discussed but also possible solutions are provided to overcome undesired sideband shifting.

Chapter 5 compares two well-established technologies to acquire the spectrum from a source and introduce a novel approach to perform spectra analysis using a superconducting single photon detector. Then, it introduces the principles that have led to the wide deployment of web-based applications and presents two examples custom-made for the specific applications used in our laboratories, namely the control of the spectroscopy system Iris-S19 and the Fabry Perot tunable filter.

Chapter 5 summarizes the results obtained during the PhD work and presents an outlook for the possible advancements in this field of research.

REFERENCES

[1] A. Rubenok, J. A. Slater, P. Chan, I. Lucio-Martinez, and W. Tittel. Real-world two-photon interference and proof-of-principle quantum key distribution immune to detector attacks. *Physical Review Letters*, 111(13), 9 2013.

[2] J. Yin, YH. Li, SK. Liao, and al. Entanglement-based secure quantum cryptography over 1,120 kilometres. *Nature*, 582(7813):501 –505, 6 2020.

[3] W. Wootters and W. Zurek. A single quantum cannot be cloned. *Nature*, 299(9):802–803, 10 1982.

[4] LM Duan, M. Lukin, J. Cirac, and al. Long-distance quantum communication with atomic ensembles and linear optics. *Nature*, 414:413– 418, 11 2001.

[5] W. J. Munro, K. Azuma, K. Tamaki, and K. Nemoto. Inside Quantum Repeaters. *IEEE Journal of Selected Topics in Quantum Electronics*, 21(3):78–90, 5 2015.

[6] N. Sangouard, C. Simon, H. De Riedmatten, and N. Gisin. Quantum repeaters based on atomic ensembles and linear optics. *Reviews of Modern Physics*, 83(1):33–80, 3 2011.

[7] L. Schweickert, K. D. Jöns, M. Namazi, G. Cui, T. Lettner, K.D. Zeuner, Montaña Scavuzzo L., S. F. C. da Silva, M. Reindl, H. Huang, R. Trotta, A. Rastelli, V. Zwiller, and E. Figueroa. Electromagnetically Induced Transparency of On-demand Single Photons in a Hybrid Quantum Network. *arXiv preprint arXiv:1808.05921*, 8 2018.

[8] C Cohen-Tannoudji, S Reynaud, R K Bullough, and J M Vaughan. Atoms in Strong Light-Fields: Photon Antibunching in Single Atom Fluorescence [and Discussion]. *Philosophical Transactions of the Royal Society of London. Series A, Mathematical and Physical Sciences*, 293(1402):223–237, 1979.

[9] Th. Basche ', W. E. Moerner, M. Orrit, and H. Talon. Photon Antihunching in the Fluorescence of a Single Dye Molecule Trapped in a Solid. *Physical Review Letters*, 69(10):1516–1519, 9 1992.

[10] C. Kurtsiefer, S. Mayer, P. Zarda, and H. Weinfurter. Stable Solid-State Source of Single Photons. *Physical Review Letters*, 85(2):290–293, 7 2000.

[11] P. Michler, A. Kiraz, C. Becher, W. V. Schoenfeld, P. M. Petroff, L. Zhang, E. Hu, and A. Imamoğlu. A Quantum Dot Single-Photon Turnstile Device. *Science*, 290(5500):2282–2285, 12 2000.

[12] R. M. Stevenson, A.J. Hudson, A.J. Bennett, R. J. Young, C. A. Nicoll, D. A. Ritchie, and A. J. Shields. Evolution of entanglement between distinguishable light states. *Physical Review Letters*, 101(17):170501–170505, 10 2008.

[13] A. J. Hudson, R. M. Stevenson, A. J. Bennett, R. J. Young, C. A. Nicoll, P. Atkinson, K. Cooper, D. A. Ritchie, and A. J. Shields. Coherence of an entangled exciton-photon state. *Physical Review Letters*, 99(26):266802–266806, 12 2007.

[14] M. Gurioli, Z. Wang, A. Rastelli, T. Kuroda, and S. Sanguinetti. Droplet epitaxy of semiconductor nanostructures for quantum photonic devices. *Nature Materials*, 18(8):799–810, 8 2019.

[15] Y. H. Huo, A. Rastelli, and O. G. Schmidt. Ultra-small excitonic fine structure splitting in highly symmetric quantum dots on GaAs (001) substrate. *Applied Physics Letters*, 102(15):152105 – 152109, 4 2013.

[16] A. Küster, C. Heyn, A. Ungeheuer, G. Juska, S. Tommaso Moroni, E. Pelucchi, and W. Hansen. Droplet etching of deep nanoholes for filling with self-aligned complex quantum structures. *Nanoscale Research Letters*, 11(1), 12 2016.

[17] T. Kuroda, T. Mano, N. Ha, H. Nakajima, H. Kumano, B. Urbaszek, M. Jo, M. Abbarchi, Y. Sakuma, K. Sakoda, Ikuo Suemune, Xavier Marie, and Thierry Amand. Symmetric quantum dots as efficient sources of highly entangled photons: Violation of Bell's inequality without spectral and temporal filtering. *Physical Review B - Condensed Matter and Materials Physics*, 88(4), 7 2013.

[18] S. Seidl, M. Kroner, A. Högele, K. Karrai, R. J. Warburton, A. Badolato, and P. M. Petroff. Effect of uniaxial stress on excitons in a self-assembled quantum dot. *Applied Physics Letters*, 88(20), 5 2006.

[19] A. Muller, W. Fang, J. Lawall, and G. S. Solomon. Creating polarization-entangled photon pairs from a semiconductor quantum dot using the optical stark effect. *Physical Review Letters*, 103(21), 11 2009.

[20] N. Akopian, N. H. Lindner, E. Poem, Y. Berlatzky, J. Avron, D. Gershoni, B. D. Gerardot, and P. M. Petroff. Entangled photon pairs from semiconductor quantum dots. *Physical Review Letters*, 96(13), 4 2006.

[21] Z. Q. Zhou, C. F. Li, G. Chen, J. S. Tang, Y. Zou, M. Gong, and G. C. Guo. Phase compensation enhancement of photon pair entanglement generated from biexciton decay in quantum dots. *Physical Review A - Atomic, Molecular, and Optical Physics*, 81(6), 6 2010.

[22] W. A. Coish and J. M. Gambetta. Entangled photons on demand: Erasing which-path information with sidebands. *Physical Review B - Condensed Matter and Materials Physics*, 80(24), 12 2009.

[23] N.S. Jones and T. M. Stace. Photon frequency-mode matching using acousto-optic frequency beam splitters. *Physical Review A - Atomic, Molecular, and Optical Physics*, 73(3), 2006.

[24] C.X. Yang, Y.B. Liu, and X.B. Wang. On-demand Entanglement Source with Polarization-Dependent Frequency Shift. *Applied Physics Letters*, 96(20), 9 2009.

[25] I. Y. Poberezhskiy, B. Bortnik, J. Chou, B. Jalali, and H.R. Fetterman. Serrodyne frequency translation of continuous optical signals using ultrawide-band electrical sawtooth waveforms. *IEEE Journal of Quantum Electronics*, 41(12):1533–1539, 12 2005.

[26] A. Fognini, A. Ahmadi, S. J. Daley, M. E. Reimer, and V. Zwiller. Universal finestructure eraser for quantum dots. *Optics Express*, 26(19), 9 2018.

[27] C. Qin, H. Lu, B. Ercan, S. Li, and S.J.B. Yoo. Single-Tone Optical Frequency Shifting and Nonmagnetic Optical Isolation by Electro-Optical Emulation of a Rotating Half-Wave Plate in a Traveling-Wave Lithium Niobate Waveguide. *IEEE Photonics Journal*, 9(3), 6 2017.

[28] R. Noe and D.A. Smith. Integrated-optic rotating waveplate frequency shifter. *Electronics Letters*, 24(21), 10 1988.

[29] I. Zadeh, J. Los, R. Gourgues, V. Steinmetz, G. Bulgarini, S. Dobrovolskiy, V. Zwiller, and S. N. Dorenbos. Single-photon detectors combining high efficiency, high detection rates, and ultra-high timing resolution. *APL Photonics*, 2(11), 11 2017.

[30] G. N. Gol'tsman, O. Okunev, G. Chulkova, A. Lipatov, A. Semenov, K. Smirnov, B. Voronov, A. Dzardanov, C. Williams, and Roman Sobolewski. Picosecond superconducting single-photon optical detector. *Applied Physics Letters*, 79(6):705–707, 8 2001.

2

DEPHASING-FREE ENTANGLEMENT FROM A QUANTUM DOT SOURCE

This chapter discusses the nature of photon entanglement from quantum dots under non-resonant and resonant excitation schemes. In the latter case, experiments show that the route for perfect photon entanglement mostly depends on the time resolution of the detection system and the presence of fine-structure splitting. Dephasing of the quantum state becomes in fact negligible, making the entangled photon pair generation more a measurement than a growth challenge. Improvements in superconducting single photon detection technology represent the first milestone towards perfect photon entanglement for a broad range of quantum dot sources.

2.1. INTRODUCTION

A robust quantum information infrastructure for secure communication relies on the availability of photon sources with several key features [1]. These are high extraction efficiency and brightness, high-purity single photon emission, entanglement of the photon-pair, indistinguishability of the particles, the matching of the emission wavelength to the current network infrastructure that provides minimum losses, and last, the coupling with quantum memories. Semiconductor quantum dots embedded in nanowires have shown to be promising for some aspects. They can be tailored to have efficient light extraction thanks to the combination of two factors: the high refractive index material that encapsulates the quantum dot acting as a waveguide and the tapered structure [2]. Directionality is ensured by the nanowire itself that guides the emitted light towards the vertical direction. The extracted light can have a Gaussian profile [3] that is easily coupled to single-mode fibers and fed to the telecom fiber network for long-distance transfer of entangled photons [4].

This chapter investigates *first* InAsP quantum dots embedded in an InP nanowire grown by selective-area chemical beam epitaxy and *secondly* GaAs/AlGaAs Qdots embedded in a low Q-planar cavity. The aim is to show that Qdots can emit perfectly entangled photons via the biexciton–exciton radiative cascade. Group theory considerations predict nanowire structures grown along the [111] direction to have the same point group as Qdots with wurtzite crystal structure, leading the excitonic bright states towards a degenerate level that is the condition for vanishing fine-structure splitting [5]. The choice of selective-area chemical beam epitaxy was pursued given previous demonstration of defect-free, pure wurtzite nanowires that enabled longer single-photon coherence [6].

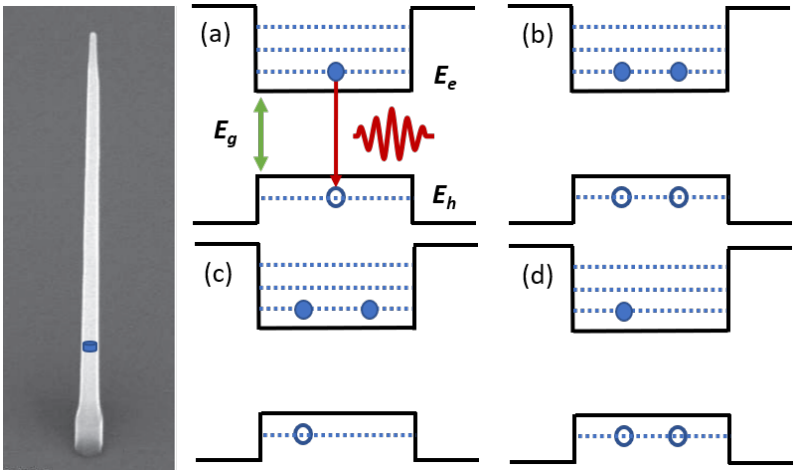

Figure 2.1: **(Left)** SEM image of tapered nanowire waveguide containing a single quantum dot drawn as a blue disk. **(Right)** Energy band diagram for excitonic transitions: (a) Energy levels in exciton (X) (b) biexciton (XX) (c) negatively charged exciton (X^-), and (d) positively charged exciton (X^+). E_g denotes the energy bandgap of the core semiconductor. E_e and E_h denote the lowest s-shell energy level for electron and hole respectively. All these transitions lead to the emission of a photon.

The simplified sketch in fig. 2.1 is taken as a reference to explain the single photon emission capabilities of Qdots. Thanks to their nanometric dimension, smaller than the exciton Bohr radius [7], Qdots can trap the charge within its confining potential. Charge carrier confinement is provided by creating an heterostructure where the core semiconductor material has lower bandgap compared to the surrounding material. When this happens, the wavefunctions of the charge carriers are indeed spatially confined in a potential well and and the energy level are discretized. The energy scale of the confinement have values up to several tens of mev [8] depending on the size of the Qdot structure. This physical mechanism ensures that only discrete energy levels can be occupied so that Qdots have an atom-like behaviour [9]. Based on these consideration, the behavior of the systems can be explained with an oversimplification, namely the particle in a box. More accurate approximations with harmonic potential well [10] better describe the atom-like energy orbitals involved but this goes beyond the scope of the thesis. In the simplified "world", sketched in fig. 2.1, there are several possible configurations for the Qdot to accommodate the charge carriers. Limiting ourselves to the cases that lead to a radiative decay, two electron-hole pair can either coexist at the same time within the Qdot forming a biexciton 2.1(b), or, if an extra electron or hole is trapped as in 2.1(a) the system has the form of a negatively charged 2.1(c) or positively charged exciton 2.1(d).

2.2. EXCITATION SCHEMES

To investigate the energy levels of the various excitonic configurations, photoluminescence experiments can be carried out by exciting the electrons in the Qdot from the valence band to the conduction band of either the InP walls or the Qdot's s-shell.

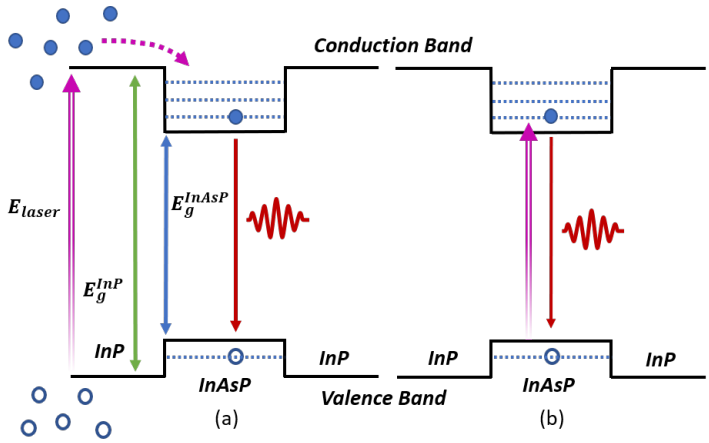

Figure 2.2: (a) In the non-resonant excitation, the laser (purple arrow) excites electrons (blue circles) and holes (hollow circles) across the bandgap of the host material. After phonon relaxation into the low energy states of the Qdot, the carriers recombine and yield a photon of energy equal to the Qdot bandgap. This process create a high concentration of extra carriers in the surrounding of the Qdot. (b) In the resonant case the laser is tuned to an energy that match exactly the Qdot transition. In this scenario extra carriers are suppressed. In both cases, using low laser power excites only one transition, namely the s-shells. As we increase laser power more carriers populate the dot and other shell transitions become visible.

In the case known as non-resonant excitation, sketched in fig. 2.2(a), the excitation laser's energy is larger than the InP bandgap of 1.344 eV. The carriers will diffuse into the Qdots and then relax towards their lowest energy states. Optical recombination within the Qdot can occur because scattering with phonons happens at times scales of several tens of ps whereas the radiative recombination takes at least 10 times longer. As such, the carriers have the time to relax into the Qdot [11]. As seen in [12], this approach generates also free charge carries in the surrounding of the Qdot with the onset of fluctuating electric fields that lead to dephasing of the quantum state. The solution to this issue is given by the so-called resonant excitation scheme [13] which is represented in fig. 2.2(b). The idea with resonant excitation is to promote the carriers directly to the Qdot s-shell within the conduction band ruling out phonon relaxation and excess in free carries in the surrounding of the Qdot. This reduces very efficiently the overall electric field into just a static component that is due to the asymmetries in the nanostructure [12, 13].

2.2.1. TWO-PHOTON RESONANT EXCITATION

Standard resonant excitation is the technique to lift an electron-hole pair into the excited state using a laser with precisely the same energy as the transition itself. Besides phonon relaxation suppression, the key feature of the resonant-type of excitation is to address the transition directly which makes the emitted photons as close as possible to the requirement of being emitted on-demand [14].

Another stringent requirement consists of controlling the pulse length of the excitation, that is crucial in creating the biexciton together with the simultaneous suppression of the exciton creation. This will be discussed later. Let's start first introducing the peculiar type of resonant excitation, where the promotion of the carrier into the excited state is mediated by two photons.

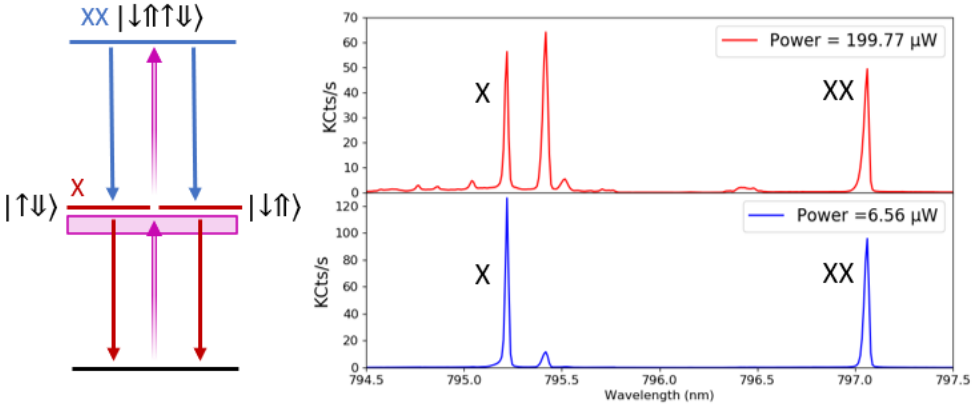

Figure 2.3: **(Left)** Sketch of the two-photon resonant excitation scheme. Since the X and XX do not exhibit same energy level, the laser must be resonant with a virtual level (purple box). **(Right)** Spectra of the AlGaAs Qdot acquired at two different power level: for higher power Qdot shell is populated and more transitions are observed. For low power the spectra shows the very clean decay for three configurations from the s-shell only (exciton, biexciton and one of the charged excitons).

Two-photon resonant excitation adds another property to the picture since it makes the biexciton (XX) and exciton (X) emissions readily available by deterministically populating the XX level. The XX level lies at lower energy than to the X due to the binding energy but even though the X is not driven resonantly, it will anyway follow the population probability of the XX state. This is demonstrated by the onset of Rabi oscillations for both transitions in fig. 2.4(Right). The core principle of resonant excitation is represented in fig. 2.3(Left). The system is promoted to the biexciton state by means of a virtual state that is created by tuning the laser to an equidistant energy from the X and XX transitions. The following Hamiltonian describes the mechanism for Qdots under two-photon resonant excitation:

$$H = \frac{1}{2}\Omega(t)(|g\rangle\langle x| + |x\rangle\langle xx|) + (\delta_x - \delta_{xx})|x\rangle\langle x| - 2\delta_{xx}|xx\rangle\langle xx| \tag{2.1}$$

where δ_x is the energy difference between the virtual level of the two-photon resonance and the energy of the exciton $|x\rangle$, δ_{xx} is the detuning between the laser energy and the two photon resonance level that is also the biexciton level $|xx\rangle$. $|g\rangle$ denotes the ground state and $\Omega(t)$ is the time-dependant amplitude of the excitation pulse. The energy scheme is sketched in fig. 2.4(Left).

As described by Rabi, the resonant system is based on the superposition between the ground and excited state of the exciton or the biexciton described by the two level system. The probability for this system to be in the excited state under resonant pumping, oscillates with excitation pulse power, namely the area under the excitation pulse peak with a characteristic frequency known as Rabi frequency [15, 16]. It is possible to monitor the probability at which the system is re-excited by varying the excitation intensity and monitoring the emission probability of a specific transition. Pulse areas depend on the average electric field applied via the laser pulse. For such a reason we increased the average optical power of the excitation and monitored the output intensity of each single transition using a spectrometer. Fig. 2.4(Right) shows the onset of Rabi oscillation derived from the area under the X and XX peaks recorded from the spectrogram.

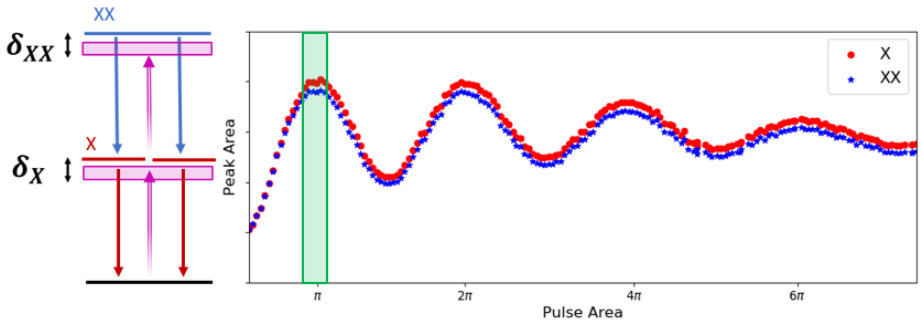

Figure 2.4: **(Left)** The energy scheme of the Qdot two-level system. δ_x is the offset energies between laser virtual level and exciton level and δ_{xx} is the offset energy with the biexciton resonant level. Note that pulse length adjustments with the pulse shaper avoid that the laser energy excitation spreads over the exciton level. **(Right)** Photoluminescence peak area of the X and XX emissions vs excitation pulse area. The probability of finding the system in the excited state oscillates with a variation of pulse area of π that demonstrates the onset of Rabi oscillations. The green-shaded represents the excitation point for the entanglement experiments.

An efficient and coherent excitation of the biexciton requires the elimination of the single exciton probability amplitude in the excitation pulse reaching at the same time the lowest possible degree of dephasing caused by the laser excitation. The fulfillment of these two requirements simultaneously leads to a trade-off between excitation pulse length and intensity. Ostermann et al. [17] proposed a model that explains the behavior of a two level-system when the system is driven by excitation pulses of different lengths. According to this model, for short pulses, due to the time-bandwidth product, the excitation of the exciton line is much more probable than for the biexciton whereas in the opposite case no full Rabi oscillation can be achieved for a given pulse area meaning that the exciton is excited while the biexciton is decaying. This motivates how crucial is to add a pulse shaper in the excitation path to be able to tune the time-bandwidth product of the excitation laser.

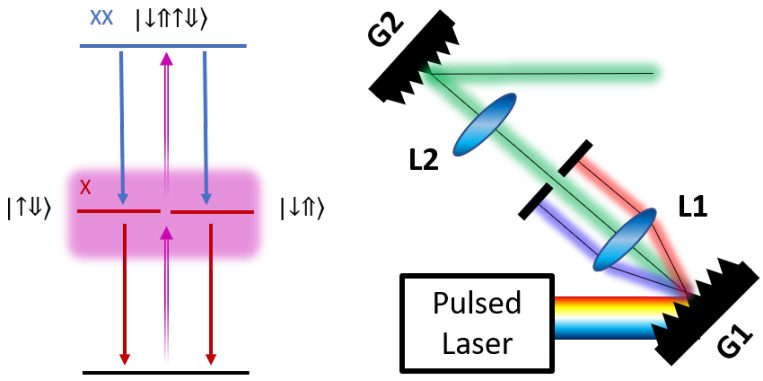

Figure 2.5: **(Left)** Two-photon resonant excitation where the pulse length is short. In this case the exciton transition is favored over the biexciton. If the pulse length is too short, the larger spectral width of the laser (purple area) that spreads over the exciton level tends to favor the promotion of the exciton. Pulse length adjustment is needed using a pulse slicer. **(Right)** Sketch of the pulse slicer consisting of a 4f lens-system with two gratings (G1 and G2) and two lenses (L1 and L2).

The used pulse shaper employs a 4f lens system consisting of two reflection gratings and two lenses arranged in a 4f geometry. A slit is placed at a distance of 2f, namely the Fourier plane. If no slit is present, each spectral component is dispersed by the first grating with an angle and then collimated to the Fourier plane by the first lens. In this plane, all the spectral components are spatially separated. Then, a second lens and a grating recombine all the frequencies into a single beam. If nothing is placed in the Fourier plane then the device is dispersion free and the output pulse shape is identical to the input one. By adding a slit in the Fourier plane, we could modify the optical density for each spectral component thus shaping the output pulse. With this technique, referred as STRUT (spectrally and temporally resolved up-conversion techniques) [18, 19], the 4f pulse shaper with a fixed slit produces a spectrally narrowed replica of the test pulse input pulse. Being the output pulse spectrally narrower than the input pulse, its pulse length will hence be larger. By the width of the aperture the pulse length can be adjusted.

2.3. THE ROLE OF SPIN-ORBIT IN THE TWO-PHOTON CASCADE

This chapter deals mainly with the generation of entangled photons from Qdots. In order to show that Qdots, despite their fine-structure splitting, can emit perfectly entangled photons, we first need to discuss in depth the physics of excitons within Qdots.

The photoluminescence spectra, presented for example in fig. 2.3 are governed by the optical selection rules depend on the electric dipole moment operator associated with the transition between the s-type state in the conduction band and p-type orbitals in the valence band of the Qdot. Transitions occur because the dipole moment operator, given its odd parity, will couple states that show opposite parity with the electron and hole wave function that are respectively even and odd for the conduction and the valence band. Recalling that the total angular momentum must be conserved in the electron-hole recombination process at all times, all transitions that violate this law can therefore be excluded.

At this point the relativistic effect of spin-orbit interaction enters the picture by coupling the carriers' angular momentum with their spin leading to the creation of ideally degenerate states within the valence band. Those states are defined by a specific total angular momentum value $J_{e,h}$. The optically active electron-hole pairs will have then a total angular momentum $J_{e,h} = L + S = \frac{\hbar}{2}$ and $\frac{3\hbar}{2}$ given that the carriers dwell in a s-type or p-type orbital respectively. The net result is that spin-orbit generates a split-off band for $j = \frac{1}{2}$ with an energy gap with several hundreds of meV difference [20]. On the other hand, the $j = \frac{3}{2}$ states form the light and heavy hole bands that are usually degenerate in the Γ point for bulk semiconductor [21].

In Qdots nanostructures, the confining potential lifts this degeneracy by splitting the two bands by several tens of meV and the heavy hole states ultimately become the ground state of the system. Once again, since the valence band is mainly constituted by s-type and p-type orbitals whereas the conduction band only by s-type orbitals, the recombination process can be mediated only by the emission of a circularly polarized photon with value $\pm\hbar$. The permitted optical transitions are shown schematically in fig. 2.6 and refer to the "bright" states $|\downarrow\Uparrow\rangle = \left|-\frac{1}{2}\right\rangle_e + \left|+\frac{3}{2}\right\rangle_h$ and $|\uparrow\Downarrow\rangle = \left|+\frac{1}{2}\right\rangle_e + \left|-\frac{3}{2}\right\rangle_h$. Fig.2.6 shows clearly the allowed optical transitions along with the occurrence probability which is lower for light hole states with higher energy gap.

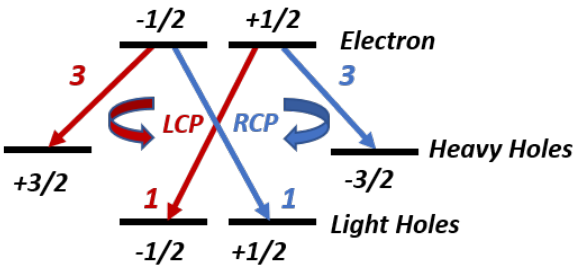

Figure 2.6: Allowed optical transitions in an ideal quantum dot with 3 and 1 being the transition rates. LCP, RCP denote the left and right circularly polarized photon.

The derivation of the permitted transitions and the representation of the excitonic energy levels stem from the misconception that the Qdots have a perfectly circular symmetrical shape and that the material responsible for the confining potential does not exert another potential. In reality, asymmetry in Qdots is easily introduced, be it either geometrical or crystallographic, leading to an energy splitting of the neutral exciton states known as fine-structure splitting. One example is given by the InP nanowire that affects the properties of the Qdot by creating a potential along the vertical direction that bends the symmetry of the wavefunctions.

2.4. THE RISE OF THE FINE-STRUCTURE SPLITTING

We have discussed how the optical excitation of a semiconductor Qdot lifts an electron across the band gap into the conduction band and leaves a hole in the valence band. This process leads to the formation of an exciton where the oppositely charged carriers are bound by mutual Coulomb interaction. The lowest-energy exciton shown in fig. 2.6 consists of two states which relate to different spin configurations of the carriers. At zero external magnetic field ($\vec{B} = 0$), although the two bright states $|\downarrow\Uparrow\rangle$, $|\uparrow\Downarrow\rangle$ are pictured as degenerate sharing the same energy level, in reality they exhibit a fine-structure splitting caused by spin-orbit coupling. This physical mechanism translate into two different effects: exchange and Rashba spin-orbit interactions. These two effects are similar in nature because they both arise from symmetry considerations and both depend on the coupling of spin and angular momentum operators leading as a consequence to the precession of the quantum state. Including the magnetic-field contribution into the frame with the Zeeman term, the full Hamiltonian for the exciton is represented by:

$$\begin{aligned} H_{tot} &= H_0 + H_{ex} + H_{RSOI} + H_{Zeeman} \\ &= -\frac{\vec{\nabla}_r^2}{2m_r} + V_{ex} + (\alpha_e \vec{\sigma}_e - \alpha_h \vec{\sigma}_h) \cdot (\hat{n} \times i\vec{\nabla}_r^2) + \frac{1}{2}\mu_B \vec{B} \cdot (g_e \vec{\sigma}_e - g_h \vec{\sigma}_h). \end{aligned} \tag{2.2}$$

Where V_{ex} is the electron-hole interaction, m_r is the reduced mass of the exciton, α_e and α_h are the Rashba coefficients for electron and hole and g_e and g_h are the g-factors for electron and hole. The Pauli matrices $\vec{\sigma}_e$ and $\vec{\sigma}_h$ account for the spin degrees of freedom in the conduction and valence band respectively [22]. At $\vec{B} = 0$ the last term in the Hamiltonian vanishes, demonstrating that the contribution to the energy levels is given only by the exchange interaction and the Rashba term. These together describe the rise of the fine-structure splitting at $\vec{B} = 0$. On the other hand, when $\vec{B}$ is increased the Zeeman splitting can eventually dominate over the Rashba and Exchange contributions. A linear increase in Zeeman splitting of the exciton peaks is predicted as the external magnetic field increments [23, 24]. In the following, we explain the two effects that give rise to the fine-structure splitting in the Qdot at $\vec{B} = 0$.

As stated earlier, symmetry breaking, that represents the root cause for the anisotropic exchange splitting and the Rashba effect, can be ascribed either to the inherent crystallographic properties of the material or the geometrical asymmetries arising from the growth process [22, 25].

2.4.1. ANISOTROPIC EXCHANGE SPLITTING

Exchange interaction, which is the direct consequence of both electric repulsion and Pauli exclusion principle, is linked to spin-orbit interaction in crystals. Its Hamiltonian H_{ex} stems from the analysis of the total angular momentum of the electron-hole pair system [23, 26]. It is found that:

$$H_{ex} = \sum_{i=x,y,z} (a_i J_{h,i} \cdot S_{e,i} + b_i J^3_{h,i} \cdot S_{e,i}), \tag{2.3}$$

where J_h and S_e are respectively the total angular momentum of the heavy-hole and the electron spin operators. The coefficients a_i and b_i are material-dependent. The magnitude of the exchange interaction is proportional to the exchange integral E_{ex} which accounts for the exchanged position of the two charged carriers [23].

$$E_{ex} = \int\int dr_1^3\, dr_2^3 \Psi^*_X(r_1 = r_e, r_2 = r_h) \times \frac{1}{|r_1 - r_2|} \Psi_X(r_2 = r_e, r_1 = r_h), \tag{2.4}$$

where Ψ_X is the exciton wave function and r_e and r_h are the electron and hole coordinates. This interaction energy is usually more than a factor of ten smaller than the splitting between heavy and light holes [26], hence the light holes can be still neglected to describe the cascade. Being only interested in the effect of exchange interaction on the "bright" states, that are the ones involving the emission of photons, and considering that H_{ex} does not involve a mixing of "bright" and "dark" states, its representation matrix in the bright exciton states $|\downarrow\Uparrow\rangle$ $|\uparrow\Downarrow\rangle$ basis, is given by:

$$H_{ex} = \begin{pmatrix} \delta_0 & \delta_1 \\ \delta_1 & \delta_0 \end{pmatrix} \tag{2.5}$$

In the ideal case of fully symmetrical Qdots, matrix 2.5 reduces to:

$$H_{ex} = \begin{pmatrix} \delta_0 & 0 \\ 0 & \delta_0 \end{pmatrix} \tag{2.6}$$

The latter matrix implies that $|\downarrow\Uparrow\rangle$ and $|\uparrow\Downarrow\rangle$ are degenerate eigenstates of H_{ex}. In this scenario the only possible polarizations for the photon emitted is either left of right circular as imposed by the optical selection rules. In case the Qdot shows asymmetry (as in matrix 2.5), the bright excitons will hybridize and give rise to the two new eigenstates that are symmetric and antisymmetric linear combinations of the two excitons $|\downarrow\Uparrow\rangle$, $|\uparrow\Downarrow\rangle$, split by the anisotropic exchange splitting δ_1. In this new scenario two orthogonal linearly polarized photons at different energies can interact with the dot. Moreover, from symmetry considerations in the calculation of the integral 2.4, the exchange interaction for the biexciton vanishes because the two electrons and the two holes together form a singlet state [23, 27]. Sketch 2.7 describes the above case where symmetry breaking induces an energy level splitting.

As a result, the energy of the emitted photons, which depends only on the energy of the ground state, can now be distinguished by the anisotropic exchange splitting δ_1. This contribution together with the Rashba effect was thought to ultimately hinder the generation of fully entangled photons in polarization space. However, we will show here that even with their presence, perfect entanglement is possible.

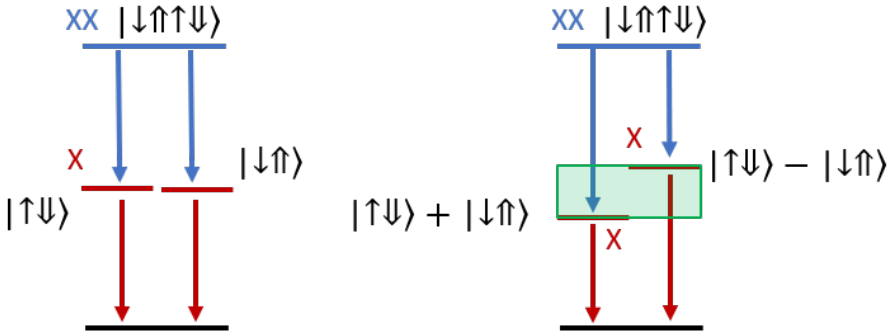

Figure 2.7: Sketch of the anisotropic exchange splitting. The biexciton and exciton are described by the combination of electron and hole spins as ↑, ↓ and ⇑, ⇓ respectively. **(Left)** With vanishing FSS, meaning that the Qdot is perfectly symmetric, the X energy level is degenerate for opposite spin configurations. **(Right)** With not vanishing FSS the exciton energy levels are split by the δ_1 (green box). The quantum state precesses between the two new states generated by the linear combination of the eigenstates $|\downarrow\Uparrow\rangle$, $|\uparrow\Downarrow\rangle$.

2.4.2. THE RASHBA EFFECT

If the crystal structure lacks space inversion symmetry due to crystallographic or geometrical reasons, spin-orbit coupling leads to a spin-based splitting of the energy bands. In fact, in the reference of a moving electron, the Rashba effect transforms into a magnetic field, coupling the electron spin with its momentum. This effective magnetic field lifts the degeneracy of the spin-degenerate bands.

In atomic physics, spin–orbit interaction is the relativistic coupling between the intrinsic magnetic dipole $\vec{\mu}$ of a moving charged particle and the electric field $\vec{E}$ produced by the atom. This motion of the particle within this potential landscape generates an effective magnetic field $\vec{B}_{eff}$ that interacts with $\vec{\mu}$. Given α the coupling strength constant, since the particle motion $\vec{p}$ is linked to the specific orbital motion $\vec{L}$ and that magnetic dipole $\vec{\mu}$ is linked to the particle's spin $\vec{S}$ the spin-orbit Hamiltonian reads:

$$H_{SOI} = -\vec{\mu}\vec{B}_{eff} = \alpha\vec{B}_{eff}\cdot\vec{S} = \alpha(\vec{E}\times\vec{p})\cdot\vec{S} = \alpha(\vec{r}\times\vec{p})\cdot\vec{S} = \alpha\vec{L}\cdot\vec{S} \tag{2.7}$$

The net result of Rashba spin-orbit interaction (RSOI) is to split an orbital energy state into two new states whose spin configuration is either aligned or anti-aligned to the orbital field. This consideration extends to the case of solid crystalline material, where the carriers moving in the lattice are affected by additional effects to just the orbital movement. These effects consist of the coupling between either the intrinsic potential of the lattice or the external potential arising from the shape of the nanostructured semiconductor with the electron spin. For wurtzite type of crystals, Rashba spin-orbit interaction is due to the intrinsic asymmetry of the uniaxial crystals or the inhomogeneity of the interfaces of the nanowire heterostructure that typically transduce into piezoelectric fields [28, 29].

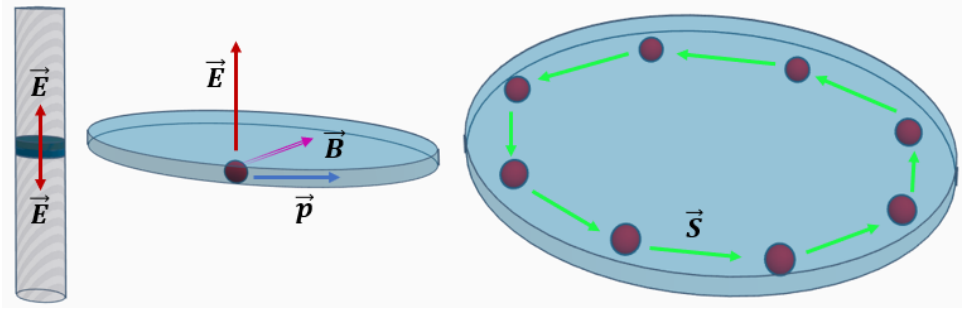

Figure 2.8: Classical frame of a moving particle (red sphere) with momentum $\vec{p}$ in the Qdot plane under the action of an external electric field $\vec{E}$. As the particle moves in the Qdot plane the spin vector $\vec{S}$ changes its orientation to adjust perpendicularly to the effective $\vec{B}$ field. This precession causes the entanglement evolution over time.

For sake of clarity, we can model the motion of the electron in the bi-dimensional Qdot plane in the presence of RSOI. The term $H_{RSOI} = (\alpha_e \vec{\sigma_e} - \alpha_h \vec{\sigma_h}) \cdot (\hat{n} \times i\vec{\nabla_r^2})$ in eq. 2.2 becomes [25]:

$$H_{RSOI} = \frac{\vec{p}^2}{2m_e} + \frac{\alpha}{\hbar}(\vec{s} \times \vec{p})_z \tag{2.8}$$

with its eigenvalues are given by:

$$E_{RSOI}(\vec{k}) = \frac{\hbar^2 k^2}{2m_e} \pm \alpha k = \frac{\hbar^2}{2m_e}(k \pm k_{SO})^2 \tag{2.9}$$

and eigenstates:

$$\Psi_{RSOI}(r) = \frac{e^{i\vec{k}\cdot\vec{r}}}{\sqrt{2}} \begin{pmatrix} 1 \\ \pm e^{\pm i \operatorname{atan}(k_y/k_x)} \end{pmatrix} \tag{2.10}$$

where $k = \sqrt{k_x^2 + k_y^2}$ is the norm of electron momentum and $k_{SO} = \frac{\alpha m_e}{\hbar}$ is defined as the RSOI constant. Its eigenvectors are described by two plane waves with its spinor term that depends on the (k_x, k_y) momentum components of the moving particle. Spin and momentum are locked to each other. The spin-dependant states are always perpendicular to the motion direction. For an electron moving along $\hat{x}$, the spinor part of the eigenvectors become (1, i) and (1, -i) meaning that the spin-up and spin-down are along $\hat{y}$. By contrast, for an electron moving along $\hat{y}$, the eigenvectors become (1, 1) and (1, -1) with spin-up and spin-down states laying along $\hat{x}$ and the exciton precesses with frequency $\hbar$ divided by the fine-structure splitting.

2.5. INTERPLAY OF DETECTOR TIME RESOLUTION AND FSS

To summarize, counter-propagating electrons have opposite spins. Since spin and momentum are locked to each other, the consequence of the Rashba effect in photon pair generation may yield distinguishable photons. The term "may" has to be explained in more details. In case of zero fine-structure splitting the total wavefunction of the XX and X photon decay is time independent and reads:

$$|\Psi\rangle = \frac{1}{\sqrt{2}}\left(|HH\rangle + |VV\rangle\right), \tag{2.11}$$

that is a maximally entangled Bell state. Thus, perfect entanglement, which relies on the generation of indistinguishable photons, necessitates for a Qdot source with no fine-structure splitting. As such, the quantum state of the photon pair in polarization space will become totally independent from the exciton spin dynamics.

Nevertheless, the combined effect of Rashba and anisotropic exchange splitting cause the two photons polarization state to depend on a phase factor that accounts for the exciton precession between $|{\downarrow}\Uparrow\rangle + |{\uparrow}\Downarrow\rangle$ and $|{\downarrow}\Uparrow\rangle - |{\uparrow}\Downarrow\rangle$ Bell states. This is represented by plugging the fine-structure splitting into a phase factor:

$$|\Psi(t,\delta)\rangle = \frac{1}{\sqrt{2}}\left(|HH\rangle + e^{-i\frac{\delta}{\hbar}t}|VV\rangle\right) \tag{2.12}$$

The speed of the state precession between the two maximally entangled Bell states is governed by the phase factor with period dependant on the fine-structure splitting δ.

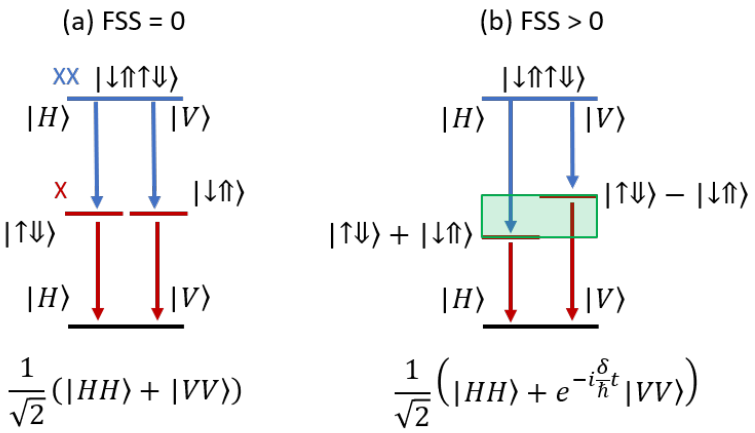

Figure 2.9: Sketch of the two-photon decay path. (a) With zero FSS the exciton energy levels are degenerate for both spin configurations and the two electron-hole recombination processes are totally indistinguishable. Thus, the two-photon state is time-independent and the emitted photons are fully entangled at all times. (b) With non-vanishing FSS the quantum spin state dynamics leads to precession of the two-photon state. This is described by the action of a time-dependent phase factor within the wavefunction.

The phase factor in eq. 2.11 leads to interesting physics. In fact, the time resolution of the detection system τ is crucial to measure entanglement: imagine, with a very slow detector $\tau >> \frac{\hbar}{2\delta}$ the complete phase factor in eq 2.12 is averaged out and no entangled correlations can be measured. In the opposite case where $\tau << \frac{\hbar}{2\delta}$, following Heisenberg uncertainty, the two decay paths cannot be distinguished anymore in energy because the measurement happens too fast and does not allow for the fine-structure splitting to be resolved.

Moreover, the phase factor evolves with time and the fast detector enables to probe the evolution of the correlations at consecutive time frames whose length is dictated by the time resolution of the instrument. Nevertheless, the detection system always presents a finite time resolution that leads to an unavoidable, although much suppressed, averaging of the phase factor. This will be later discussed in more detail.

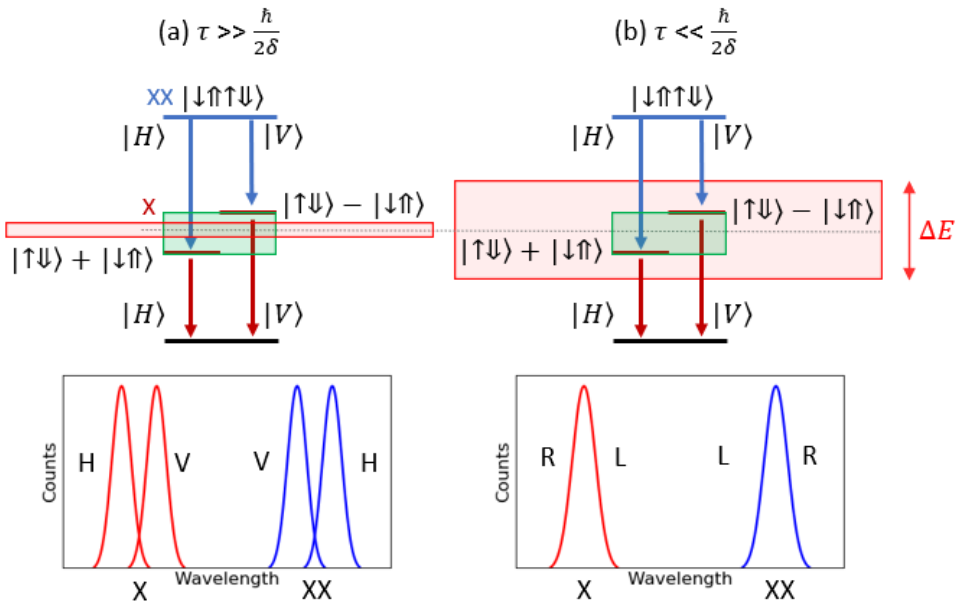

Figure 2.10: In sketch (a), the detector time resolution τ is much lower than the characteristic time precession constant of the quantum state. Stemming from the Heisenberg uncertainty principle, low uncertainty in energy resolution ΔE (red box) is predicted with a slow detection and the exciton energy levels, that are split by the fine-structure splitting δ (green box), can then be resolved, thus reducing the number of entangled correlations. In sketch (b), the two electron-hole recombination processes become totally indistinguishable and the emitted photons are fully entangled in polarization space. In fact, with a fast detection, the uncertainty in energy resolution is much higher, and the two non-degenerate states cannot be anymore resolved, pushing the degree of entanglement toward higher values.

So far, we have discussed the generation of entangled photon pairs, resonant and non-resonant excitation schemes and we highlighted the effect on two different Qdot systems, namely Qdots embedded in a nanowires and self-assembled planar Qdots.

In the following sections we will first assess the impact of the InP *nanowire waveguide* on the entanglement level through the investigation of the morphology of the po-

larization state of the X and XX transitions: this will tell whether we can expect high entanglement from a nanowire Qdot. This will be done by performing Zeeman spectroscopy showing the onset of birefringence and/or polarization. As a matter of fact, the nanowire is polarizing the Qdot light leading to a partial collapse of the quantum state on one direction and compromising the quality of the entanglement.

Once these drawbacks are worked out we will switch to another single photon source, namely *AlGaAs* Qdots, that can show emission lines at the Rubidium transition. This is of interest regarding the attempt to construct and test the single photon source combined with a quantum memory in a long-haul quantum entanglement experiment.

2.6. POLARIZING NANOWIRE: IMPACT ON ENTANGLEMENT

The rationale behind research on Qdots embedded in nanowire waveguides is their ability to push the light-extraction efficiency near to unity, a fundamental requirement to achieve deterministic single-photon emission. A promising approach was shown in [30] where single Qdots were grown along the axis of a tailored nanowire waveguide using bottom-up growth. Compared to self-assembled Qdots, these have the advantage to be more reproducible and fabricated in a much more controllable manner. However, in a non-symmetric nanowire, birefringence or polarization of the Qdot light emission can occur due to unwanted strain or material variation. In this regard, birefringence would not alter the quantum state during the passage of the photon through the nanowire. In fact birefringence acts only as an operator which rotates the two-photon polarization state $|HH\rangle + |VV\rangle$ into another unknown one. In contrast acts polarization, that, due to nanowire shape anisotropy, "measures" the quantum state before exiting the nanostructure, leading unfortunately to higher classical correlations.

Our investigation started with Zeeman spectroscopy on the exciton and biexciton emissions to study the influence of the external magnetic field $\vec{B}$ applied in Faraday configuration, namely with $\vec{B}$ parallel to the nanowire direction (see fig. 2.11). Zeeman interaction couples the external magnetic field with the spin of the carriers inducing a change in the polarization of the emitted photons. In the presence of a magnetic field the term H_{Zeeman} dominates in eq. 2.4.

$$H_{Zeeman} = \frac{1}{2}\mu_B \vec{B} \cdot (g_e \vec{\sigma}_e - g_h \vec{\sigma}_h) \tag{2.13}$$

In Faraday geometry the B-field is applied parallel to the rotational symmetry axis of the Qdot and the relative Hamiltonian projected onto the bright exciton states $|\downarrow\Uparrow\rangle$ and $|\uparrow\Downarrow\rangle$ is given by:

$$H_{Zeeman} = \frac{\mu_B B}{2}\begin{pmatrix} +(g_e + g_h) & 0 \\ 0 & -(g_e + g_h) \end{pmatrix} \tag{2.14}$$

Since rotational symmetry is preserved in this configuration, the matrix has diagonal form and no mixing between the basis states occurs. At low magnetic fields the Rashba effect and the exchange interaction dominate, and the emitted photons will have linear polarizations due to hybridization of the $|\downarrow\Uparrow\rangle$ and $|\uparrow\Downarrow\rangle$ states according to eq. 2.5. On the other hand, at higher magnetic fields, the diagonal matrix elements in matrix 2.14, that are proportional to the B-field, start to become dominant over the zero magnetic field contributions. As a result the $|\downarrow\Uparrow\rangle$ and $|\uparrow\Downarrow\rangle$ exciton states become the new eigenstates of the Hamiltonian. Each of the two states will have a different energy level and the emitted photons will be circularly polarized as imposed by the value of the total angular momentum of the exciton $S_{e,h}$ equal to ± 1. Thus, by knowing that a Qdot in the nanowire will emit perfectly circular polarized light, we want to probe the photonic effects of the nanowire such as birefringence and polarization by measuring the polarization state of the light emitted from the nanowire waveguide itself.

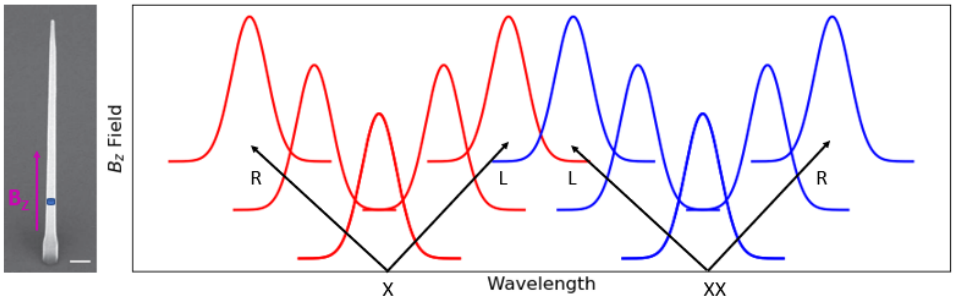

Figure 2.11: Zeeman spectroscopy in Faraday configuration: with increasing magnetic field B_z the bright exciton and the biexciton transitions split. The cascaded photons have opposite circular polarization due to total angular momentum conservation.

The Zeeman photoluminescence spectra show a clear separation between orthogonal emission lines demonstrating the effect of opposite spin configurations in the exciton biexciton decay process.

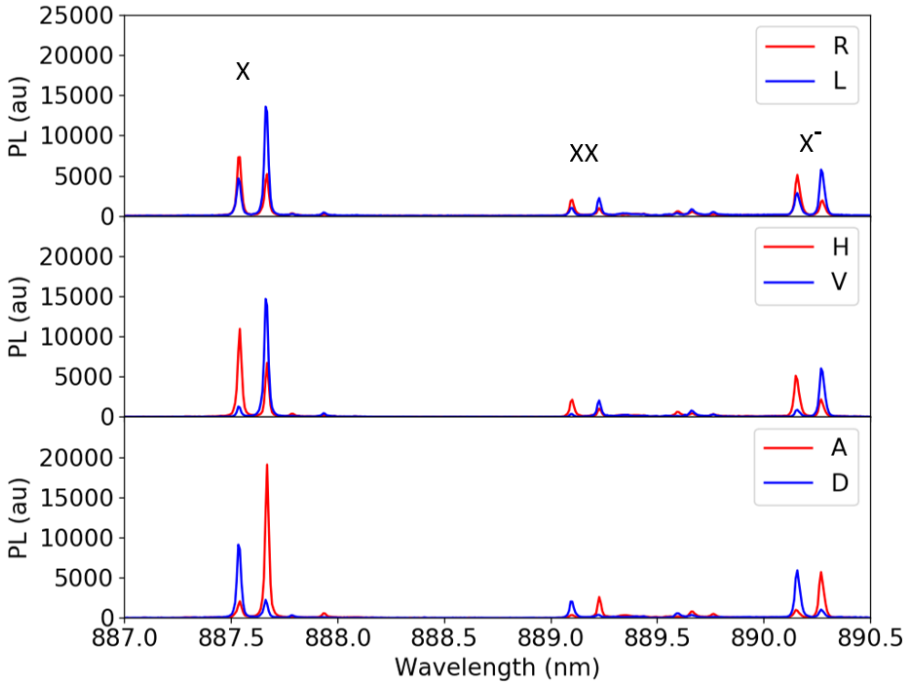

Figure 2.12: Photoluminescence spectra of an InAsP Qdot under 0.93 Tesla external magnetic field. Zeeman splitting is visible from the separation between cross-polarized emission lines for the measurement basis: $\{R,L\}$, $\{H,V\}$, $\{A,D\}$. The magnetic field is applied along the optical axis (Faraday configuration). Opposite spin projections undergo an energy splitting and optical selection rules reduce the number of transitions to two for the neutral exciton. The fact that we do not see a complete R or L polarized peaks indicate birefringence or polarization in the nanowire.

Although the prediction of perfectly circularly polarized photons emission, the *Zeeman spectra show something else*: the onset of both birefringence and polarization due to the nanowire shape anisotropy. Because of them, an interesting feature occurs in the measured spectra in fig. 2.12, namely the partial suppression of orthogonal emission lines. Due to the birifrengence caused by the nanowire, orthogonal waves of the radiation field experience different refractive indices leading to a phase change of one component compared to its orthogonal counterpart [31]. However, total suppression is never reached for any chosen basis. This is the indication that the Qdot light is impacted by the polarizing properties of the nanowire.

2.6.1. DEGREE OF POLARIZATION

The degree of polarization (DOP) describes the fraction of an electromagnetic wave with a specific polarization component. A perfectly polarized wave has a DOP of 100%, while an unpolarized wave has a DOP of 0%. A partially polarized wave, represented by a superposition of a polarized and unpolarized component, will have a DOP between 0 and 100%. DOP is calculated as the fraction of the total power that is carried by the polarized wave component and is extracted by the Stokes parameters according to:

$$DOP = \frac{\sqrt{S_1^2 + S_2^2 + S_3^2}}{S_0}, \tag{2.15}$$

where S_i is computed from the measured intensities of each polarized component I_i of the electromagnetic wave:

$$\begin{aligned} S0 &= (I_H + I_V + I_D + I_A + I_R + I_L)/3, \\ S1 &= I_H - I_V, \\ S2 &= I_D - I_A, \\ S3 &= I_R - I_L. \end{aligned}$$

Since we inferred that the nanowire shape anisotropy may polarize the light linearly, it is interesting to compute another quantity, namely the degree of linear polarization:

$$DOLP = \frac{\sqrt{S_1^2 + S_2^2}}{S_0} \tag{2.16}$$

In order to measure the projected intensities on each axis we sequentially placed a $\lambda/2$ and $\lambda/4$ wave retarders along the optical path of the PL emitted signal along and a polarizer just before the entry slit of the spectrometer. The polarizer axis is set along the H direction. For different combinations of angles (table 2.1) that give specific retardation values, all polarization states are rotated into H which is transmitted by the polarizer. The outcome of the experiment is reported in fig. 2.12 with the waveplates controlled using the code ElConRom available on GitHub [32].

State	$\lambda/2$	$\lambda/4$
$\|V\rangle$	0	0
$\|H\rangle$	$\frac{\pi}{4}$	0
$\|A\rangle$	$\frac{\pi}{8}$	0
$\|D\rangle$	$-\frac{\pi}{8}$	0
$\|R\rangle$	0	$-\frac{\pi}{4}$
$\|L\rangle$	0	$\frac{\pi}{4}$

Table 2.1: Required angles for $\frac{\lambda}{2}$, $\frac{\lambda}{4}$ waveplates for state analysis of each polarization $|i\rangle$ with i = V, H, A, D, R, L.

2.6.2. MEASUREMENT SETUP

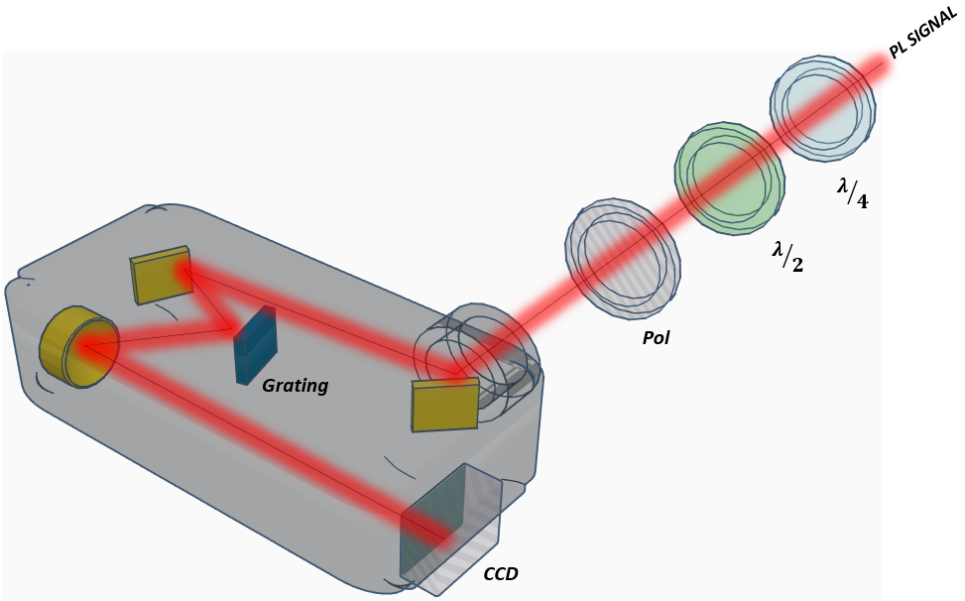

Figure 2.13: Schematic of the Polarization Tomography experiment used to assess the suppression of orthogonal emission lines. The photoluminescence signal collected by the microscope is sent to the spectrometer after its polarization state is analyzed by the wave retarders and a polarizer.

The embedded InAsP Qdot in InAs nanowire was placed in a helium bath cryostat reaching a base temperature of 4.2K. The cryostat is an open-cycle system and requires nitrogen and helium refill once a week. A dipstick is used to mount the sample along with an objective lens and nanopositioners. The inertial piezoelectric nanopositioners allow for a fine displacement of the sample in three directions with an increment of less than 100 nm to accurately place the Qdot in the focal point of the objective. The dipstick incorporates an optical window to image the sample. We used a pulsed laser at 830 nm that was collimated and directed through a round variable neutral density filter (NDF) and sent to the objective microscope via a combination of mirrors towards the bottom of

the dipstick. The emitted photons from the Qdots are collected with the same objective and directed towards a spectrometer. A filter is placed in the optical path to block the excitation light reflected from the sample. A white light source and a CCD camera were added to image the sample's surface and allowed to position the nanowires accurately. To resolve the Zeeman Spectra we used a high resolution spectrometer with dispersion length of 75 cm and equipped with three diffraction gratings. For the detection we used a back illuminated CCD detector by Princeton Instruments which, in combination with the 1800 l/mm grating, gives a spectral resolution of about 30 μeV.

2.6.3. RESULTS

Although the quantum state in eq. 2.12 is not affected by the birifrengence, that acts as a unitary phase transformation, shape anisotropy leads to the polarization of the X and XX emissions. Birefringence leads only to a different state reconstructed matrix but shape anisotropy reduces the measurable entanglement significantly.

To investigate the effect of shape anisotropy the total degree of polarization and the linear degree of polarization were calculated by means of the Stokes parameters and rendered in a polar plot (see fig. 2.14). This graph gives insight on the polarization state of light, be it either unpolarized or linearly polarized for the X and XX transitions.

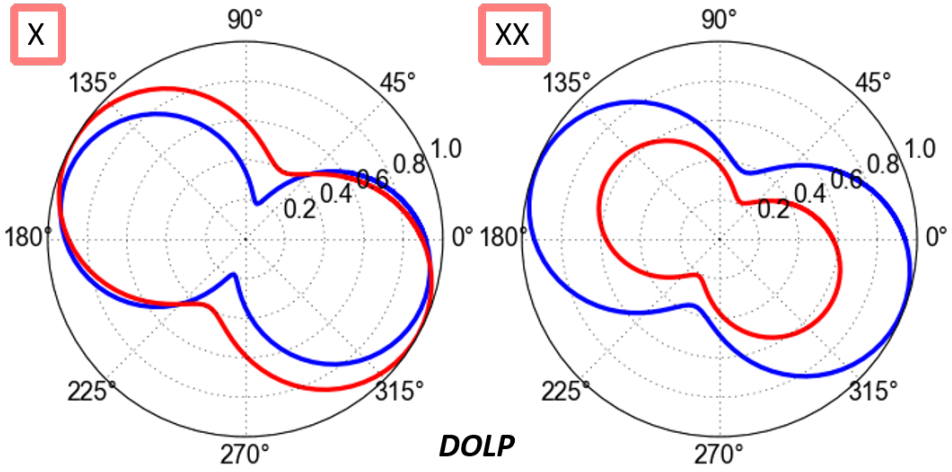

Figure 2.14: DOLP of the X and XX orthogonal emission lines when an external magnetic field of 0.93 Tesla is applied. The light is partially linearly polarized.

Although the optical selection rules dictate complete circular polarization due to the nature of electron-hole recombination regarding carriers with opposite spin, the linear degree of polarization indicates that at least to 70% of the light exiting the nanowire is linearly polarized. It is also interesting to note that one of the biexciton emissions shows a relevant fraction of either unpolarized or circularly polarized light as pointed out by the lower magnitude (red curve in the XX plot of fig. 2.14). Similar physics was previously reported in [31] and [33]. With new insight on properties of the InP nanowire, we will

demonstrate how the entanglement quality of the single photon emitter is degraded by the nanowire waveguide. Then we will compare the results with another sample consisting of self-assembled AlGaAs Qdots that is not impacted by the polarization mechanism of the embedding nanostructure.

2.7. SINGLE PHOTON SOURCE PURITY

The generation of fully entangled photon pairs is limited by the "purity" of the single photon source. Generally a light pulse is described with the state of number of photons in each mode, known as Fock state. In the case of a photon wavepacket with specific spatial frequency and polarization, a "pure" single photon source will generate light pulses containing one single photon with a Fock state described as $|n\rangle = |1\rangle$. During the exciton-biexciton cascade unwanted multiphoton emission by the impure source will spoil the degree of entanglement. This is because there will be a fraction of photon counts that cannot be ascribed to the quantum entangled two-photon state generated in the cascade process.

As discussed in [12], the estimation of the full density matrix used to evaluate the concurrence level must account for the amount of "impure" emissions which is done by adding the contribution of uncorrelated light with two additional terms. This will be explained in details in section 2.8, where we will use the extracted parameters of single photon purity to predict the concurrence evolution for the AlGaAs Qdot sample.

2.7.1. SECOND ORDER CORRELATION FUNCTION

Time-resolved measurements enable to probe whether the Qdot light field does not contain more than one photon at a time. This is done with a Hanbury Brown and Twiss (HBT) experiment that measures the second-order intensity correlation function $g^2(\tau)$. This quantity estimates the single-photon purity of the source and its expression reads:

$$g^2(\tau) = \frac{\langle n_1(t) n_2(t+\tau)\rangle}{\langle n_1(t)\rangle \langle n_2(t+\tau)\rangle} \tag{2.17}$$

where $n_{1,2}$(t) is the number of counts measured on each detector at time t. Simply stated, a light field with no more than one photon a time leads to $g^2(0) = 0$ whereas a laser field gives $g^2(0) = 1$. Intensity-autocorrelation can be measured using either pulsed or continuous wave excitation.

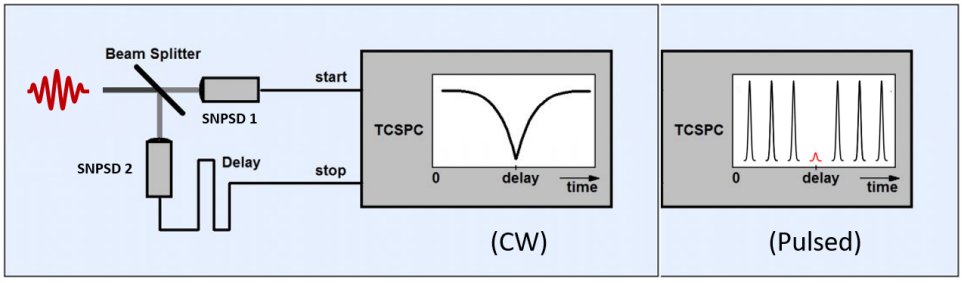

Figure 2.15: Sketch of the HBT setup for continuous-wave and pulsed excitation schemes using a Time-Correlated Single Photon Counting device. The light pulse (red signal) is split by a beam splitter. The spatially separated light pulses trigger the operation of two superconducting single photon detectors: SNSPD 1 feeds the start pulse to the counting electronics whereas SNSPD 2 delivers the stop pulses. A delay line of is used to place the coincidence point in the centre of the recording-time interval [34].

In both cases, after excitation, the emitter cannot be re-excited and delivers a second

photon until it has relaxed into the ground state. As a result, the emission of several photons becomes increasingly unlikely as the time between the photons gets shorter than the excited-state lifetime. In case of pulsed excitation, with the emission triggered on-demand, the light field is sent to a beamsplitter and two single-photon detectors measure each output. The superconducting nanowire single photon detector (SNSPD) pulse triggers the correlation electronics and measures the time delay τ between coincident detection events. Correlations are observed at multiples of the laser repetition time, corresponding to coincidences for photons emitted in different pulses. At zero delay, a coincidence peak arises if only more than one photon travels in the same light pulse. In case of continuous wave excitation, the system is continuously promoted into the excited state and we witness instead a dip at times $\tau = 0$. Once again this demonstrates that the system cannot be re-excited within times shorter than the lifetime of the emitter with the rise of the $g^2(\tau)$ dictated by the lifetime of the Qdot source.

2.7.2. RESULTS

In this section we show the Intensity-autocorrelation measurements on the X and XX transitions performed in pulsed and continuous wave excitation. Both schemes prove a good quality of single photon purity the InAsP nanowire and AlGaAs Qdots.

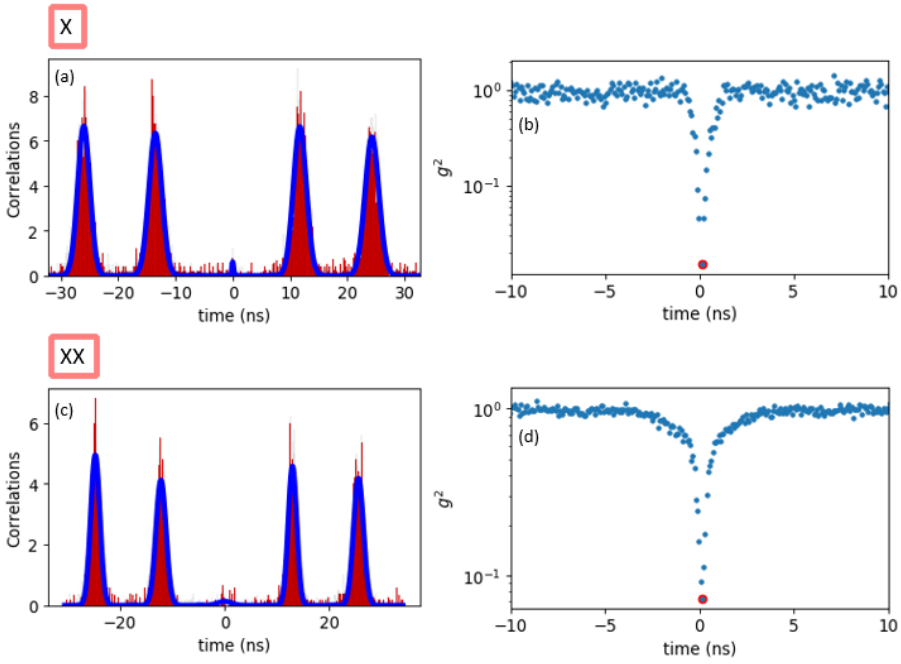

Figure 2.16: (a) Intensity-autocorrelation measurement of the X transition for the InAsP Qdot excited with a pulsed laser at 80 MHz repetition rate fitted with a Gaussian function. $g^2(0) = 0.012$. In (b), $g^2(0) = 0.015$ (red dot) was measured using non-resonant continuous wave excitation at 830 nm. (c) Intensity-autocorrelation measurement of the XX transition. $g^2(0) = 0.04$. In (d), $g^2(0) = 0.07$(red dot) was also measured using non-resonant continuous wave excitation at 830 nm.

The two excitation schemes yield similar values for the $g^2(0)$. Continuous wave excitation shows a slightly higher number due to the fact that more carriers will populate the Qdot compared to the pulsed excitation scheme, thus leading to higher multi-photon emission. In addition, it has to be noted that for the continuous wave excitation, the dip at $\tau = 0$ cannot be fully resolved because the measurement accounts for the convolution of the correlations with the response function of the detection.

Lastly we present the results for the AlGaAs sample where the Intensity autocorrelation measurement was measured under π-pulse two-photon resonant excitation.

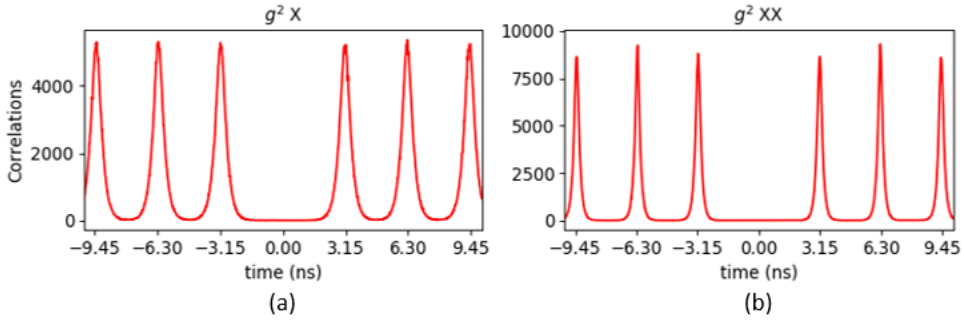

Figure 2.17: Intensity-autocorrelation measurement of the X (a) and XX (b) transitions showing the coincidences plotted over the delay time. Very pure single-photon emission is confirmed with $g^2(0)$ of a just few coincidences. Similar findings were reported by Schweickert et al. in [35]

As expected, the g^2 functions for both the X and XX are extremely clean because resonant excitation generates very little additional charge carriers in the vicinity of the Qdot which could spoil the single-photon emission.

In the next section we will make use of the $g^2(0)$ value to construct a model that explains the evolution of the measured entanglement. A complete picture must in fact take into account the multi-photon emission which degrades the two-photon entanglement.

2.8. ENTANGLEMENT ANALYSIS

Two different entanglement analysis setups were used. With the first one we measured InAsP/InP nanowire Qdots whereas the second was used to measure GaAs/AlGaAs Qdots. The two measurements were carried out at TU Delft labs and KTH Quantum NanoPhotonics Group respectively.

InP/InAsP Qdot have shown their limitations regarding the generation of highly entangled photons. We then focused our attention on GaAs/AlGaAs Qdots that were proven to offer a deterministic wavelength control and ultra-narrow wavelength distribution, specifically tailored to match the optical transitions of Rubidium [36]. This is interesting in the perspective of a hybrid quantum repeater that interfaces entangled photon qubits with a rubidium vapour-based quantum memory.

2.8.1. QUANTUM STATE TOMOGRAPHY MEASUREMENTS

To probe the time evolution of the quantum state we performed a quantum state tomography measurement and measured the polarization dependent cross-correlation between XX and X emissions. Density matrix reconstruction was done using 36 possible correlation basis given by the combination of H,V,A,D,R,L polarization directions. Correlations were measured within a single time bin with time discretization imposed by the time resolution of the detection system.

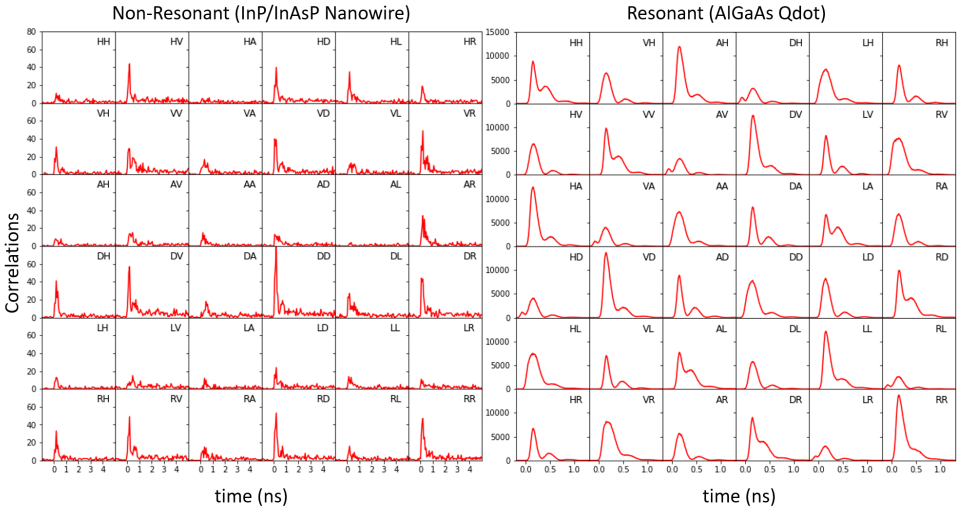

Figure 2.18: Retrieved data from the quantum state tomography of all the 36 possible basis. **(Left)** InAsP/InP nanowire: Integration time per basis was 1200 s. Level of correlations are below 20 over the InAsP exciton decay time. **(Right)** AlGaAs Qdot: Integration time per basis was 600 s. Level of correlations are around 10000 for all measurement basis. The nanowire was excited non-resonantly at 830 nm (see spectrum in fig. 2.12) whereas the Qdot was excited resonantly at 796.3 nm (see spectrum in fig. 2.3).

2.8.2. STATE PRECESSION

The theoretical probability of measuring a correlation event for each basis within one time bin is given by the convolution of the quantum state projection squared damped by the radiative lifetime of the Qdot, and the instrument response function $g(t)$.

$$p_{ij} = \left(|\langle ij|\Psi(t)\rangle|^2 n(t,\tau_x)\right) * g(t)dt \tag{2.18}$$

where $n(t,\tau_x)$ is the damping factor accounting for the exciton decay time τ_x. Eq. 2.12 predicts the precession of the quantum state between two maximally entangled Bell States $|\Phi^+\rangle = \frac{1}{\sqrt{2}}(|HH\rangle + |VV\rangle)$ and $|\Phi^-\rangle = \frac{1}{\sqrt{2}}(|HH\rangle - |VV\rangle)$ with period $\hbar/\delta$. Plotting the difference of the coincidences of the quantum state projected onto these two states as in eq. 2.19 provides a mean to indirectly measure the fine-structure splitting.

$$\langle\Phi^+|\Psi(t,\delta)\rangle - \langle\Phi^-|\Psi(t,\delta)\rangle = e^{-i\frac{\delta}{\hbar}t} \tag{2.19}$$

2.8.3. CONCURRENCE

The concurrence is a quantity used to determine the degree of the measured entanglement in any quantum correlated system. It is a particularly useful figure of merit because it is not looking to match a particular quantum state, like for instance fidelity, and it is therefore independent of the frame of reference. Concurrence values range from 0.5 to 1 meaning that the photonic pair of qubits are either completely classical or fully entangled. Concurrence yields these values by performing a basic operation: the dot product between the product state of the two qubits and the same state after the applying the state flip operator.

Let's imagine a pair of qubits described by a pure product state. In this case, the state flip operation applied to a pure product state will rotate it into the orthogonal state which is diametrically opposite on the Bloch sphere. Therefore, the dot product of these two vectors will yield a concurrence value of 0.5. On the other hand, a completely entangled state such as a maximally entangled Bell state is left invariant by the state flip and therefore the dot product yields a concurrence of 1 [37]. Physically, concurrence is evaluated from the quantum state tomography measurements [38]. Experimental fluctuations in measured correlations result in errors affecting quantum state reconstruction. Nevertheless, the statistical technique used to quench these errors is the maximum likelihood estimation which is based on the following protocol:

- From the tomographic measurements of the quantum state, guess a physical density matrix (Hermitian with unit trace and non-negative eigenvalues).
- Simulate a state tomography measurement based on the guessed density matrix and compute the difference (χ^2) between the guessed and experimental data.
- Correct for the guessed density matrix that minimizes χ^2.

This procedure allows to reconstructs the real and imaginary components of the density matrix and ensures that it meets the criteria required to be physical, namely being Hermitian with non-negative eigenvalues. To perform all the above steps, we used the quantum tomography code provided in [39].

2.8.4. INASP/INP NANOWIRE

The quantum entanglement setup at TU Delft was built by adding a polarizing beam splitter to the polarization tomography setup in fig. 2.13. The photoluminescence signal, coming from the nanowire excited non-resonantly at 830 nm, was directed towards two spectrometers of the same kind. Their gratings were tuned to reflect either the X or the XX emission lines respectively towards two SNSPDs that showed each a time resolution of 50 ps and a dark count rate of nearly 0 Hertz. Lastly, the picoHarp time-correlated single photon counting (TCSPC) module was used to probe the X-XX cross correlations.

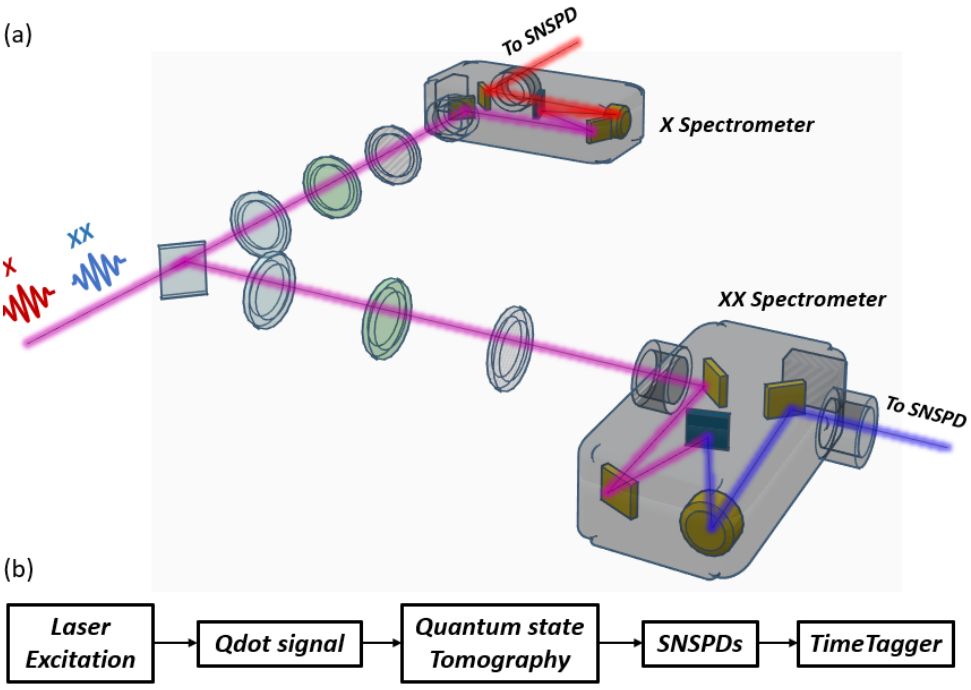

Figure 2.19: (a) Quantum State Tomography stage. The photoluminescence signal is split at the beam splitter with the X and XX transitions selected at each arm by two spectrometers. Once the signals have left the spectrometer, they are coupled to the respective SNSPD that triggers the operation a PicoQuant TimeTagger. (b) Diagram of the setup from Qdot excitation to the measurement of photon correlations.

Unfortunately we were unable to sample a large number of correlations (as seen in fig. 2.18) and we attribute it to both the low brightness of the source and the not perfect alignment/coupling of setup/fibers. However, thanks to the very high time-resolution of the detection system (50 ps) and a long integration time, we could still resolve the dynamics of the state precession between the two maximally entangled Bell states $|\Phi^+\rangle = \frac{1}{\sqrt{2}}(|HH\rangle + |VV\rangle)$ and $|\Phi^-\rangle = \frac{1}{\sqrt{2}}(|HH\rangle - |VV\rangle)$. Meaningful evaluation of the concurrence evolving with time was not possible since the maximum likelihood estimation necessitates stronger photon counts statistics as the density matrix reconstruction will be impacted more by false correlations and dark counts. However, the concurrence was extracted at the time bin where the correlations hit the peak value, being 75.2%. With

hindsight, it is clear that the degradation of concurrence may depend on the polarizing behaviour of the nanowire shown in section 2.6.

The fine-structure splitting was extrapolated by fitting the quantum oscillation with the equation of a damped oscillator (see fig 2.20(a)) that resulted in a value of 1200 ± 18 MHz. Once again the relatively high uncertainty value has to be ascribed to the poor photon count statistics.

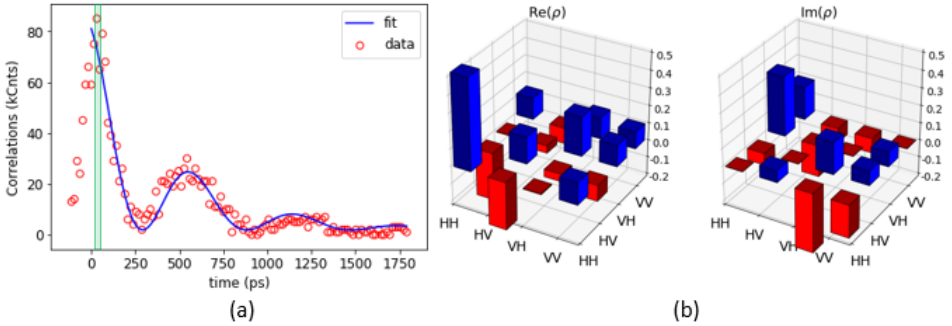

Figure 2.20: (a) Plot of (RL) coincidences of the two-photon correlation measurements between X and XX emissions showing quantum oscillations in coincidences in a 1.5 hours measurement. Red dots indicate measured data and blue trace shows the fitting with a damped oscillator. The oscillation appear because the quantity $(RL+LR)-(RR+LL)$ coincidences describes the state precession between the two maximally entangled Bell states as predicted in eq. 2.19. Plot of $(RL+LR)-(RR+LL)$ is not showed because of the low level of correlations for all combinations of polarization basis.(b) Real and imaginary components of the density matrix evaluated at the time bin where the correlations reach maximum value (see green-highlighted bin in (a)).

Given the not satisfactory results provided by this nanowire sample we moved onto another class of materials, namely GaAs/AlGaAs Qdot. The Qdots can be tailored to emit at the Rubidium transition energy and hence are very interesting for quantum memory applications. We also expect that the absence of a nanowire around the Qdot will give negligible impact on the polarization of the emitted photons. With this in mind there are great hopes for the generation of highly entangled photonic qubits.

2.8.5. GAAS/ALGAAS QDOT

The quantum entanglement setup built at KTH QNP labs, compared to the previous one reported in fig. 2.19, allowed to perform two-photon excitation. The sample of GaAs quantum dots surrounded by AlGaAs, provided by the collaborators at Nanoscale Semiconductors Group at the JKU in Linz, was grown with Molecular Beam Epitaxy. The key feature of these structures is that they are grown in droplet-etched nanometer-sized holes. The fabrication consists of depositing AlGaAs onto a GaAs substrate. The etching process occurs because the Al droplets first condense on the surface and then desorb [40]. In a second step the holes are filled with GaAs followed by an annealing to let the GaAs diffuse into the holes. Finally, the holes are capped with more AlGaAs. This process enables the creation of highly symmetric holes and consequent Qdot structures with low fine–structure splitting.

The sample was placed in a closed–cycle cryostat and cooled to 10 K. Excitation was

provided by a tunable pulsed laser which generates short ps pulses with a repetition rate of 320 MHz. In order to resonantly pump the biexciton state with a two-photon process, the laser was tuned to 796.1 nm, that is the energy corresponding to half the energy difference between the ground state and the biexciton state. Next, a pulse slicer, made of a 4f-lens system with two gratings, was used to adjust the length of the laser pulses to a maximum value of 100 ps as discussed in sec. 2.2.1. This was of particular use to maximize the biexciton population and to suppress the exciton population. The emitted photoluminescence signal was collected and sent to the entanglement analysis setup where tunable notch filters with 0.7 nm spectral bandwidth were used to block the excitation laser and to reflect a selected Qdot transition and separate XX from X line. The notch filters were placed to direct the photoluminescence signal towards the quantum state tomography stage where the waveplates in combination with a polarizer served the purpose of setting the measurement basis for the quantum state tomography measurement. Finally, the light on each arm was coupled into single mode fibers connected to two SNSPDs with time resolution of approximately 60 ps, efficiencies of roughly 80% and dark count rate around 1 Hz. Timestamps and correlations triggered by the SNSPD pulses were acquired with a Time-Correlated Single Photon Counting module provided by PicoQuant. The complete setup is sketched in fig. 2.21

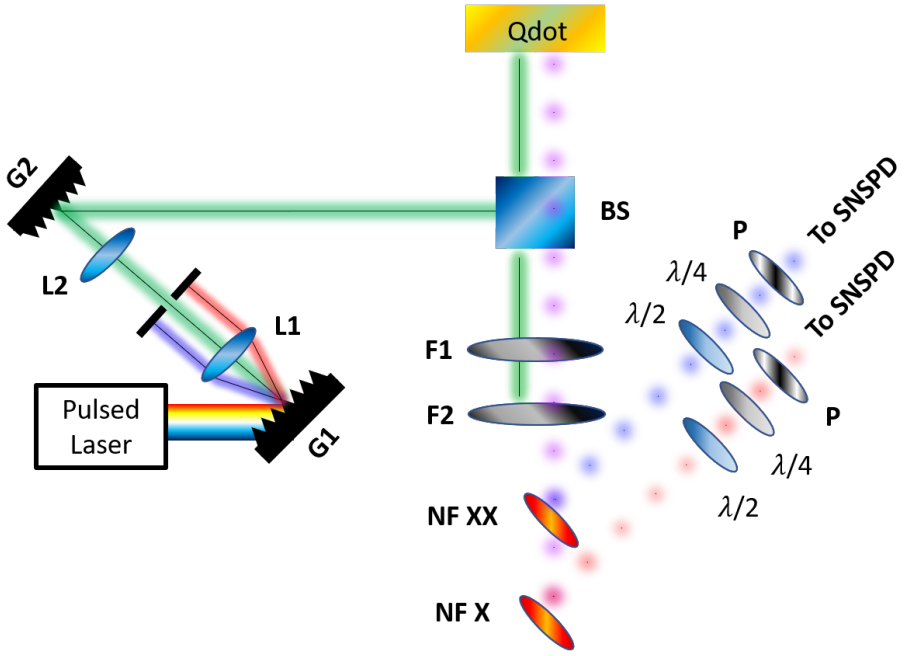

Figure 2.21: Entanglement setup consisting of pulsed laser excitation, pulse shaper made of a 4f-lens system with two gratings (G1, G2) and two lenses (L1, L2), cryogenically cooled AlGaAs Qdot sample. The excitation path is made of a beam splitter BS and a pair of filters (F1, F2) to block laser scattering. XX and X lines are selected with a sequence of two notch filters (NF XX, NF X). State tomography is performed with waveplates ($\lambda/2$, $\lambda/4$) and polarizers (P). Light travels in single mode fibers towards two SNSPDs for time-resolved measurements.

For this sample, the photoluminescence (PL) spectra in fig. 2.3 have shown good brightness for both exciton and biexciton emission lines with a value around 120000 and 80000 counts per second under π pulse excitation. Lastly, we remind the outstanding single photon purity $g^2(0)$ provided by the Qdot in combination with the excitation scheme in fig. 2.17. Regarding the Quantum State Tomography measurement, this has yield much higher correlations although the integration time was halved compared to the InAsP/InP nanowire (600 s) as seen in fig. 2.18. In contrast to the InAsP/InP nanowire sample, this time the measurement has let us see the whole entanglement evolution over the radiative decay time of the Qdots. This will be shown in next section. Now, focusing on the quantum oscillations, we can retrieve the value of the fine-structure splitting.

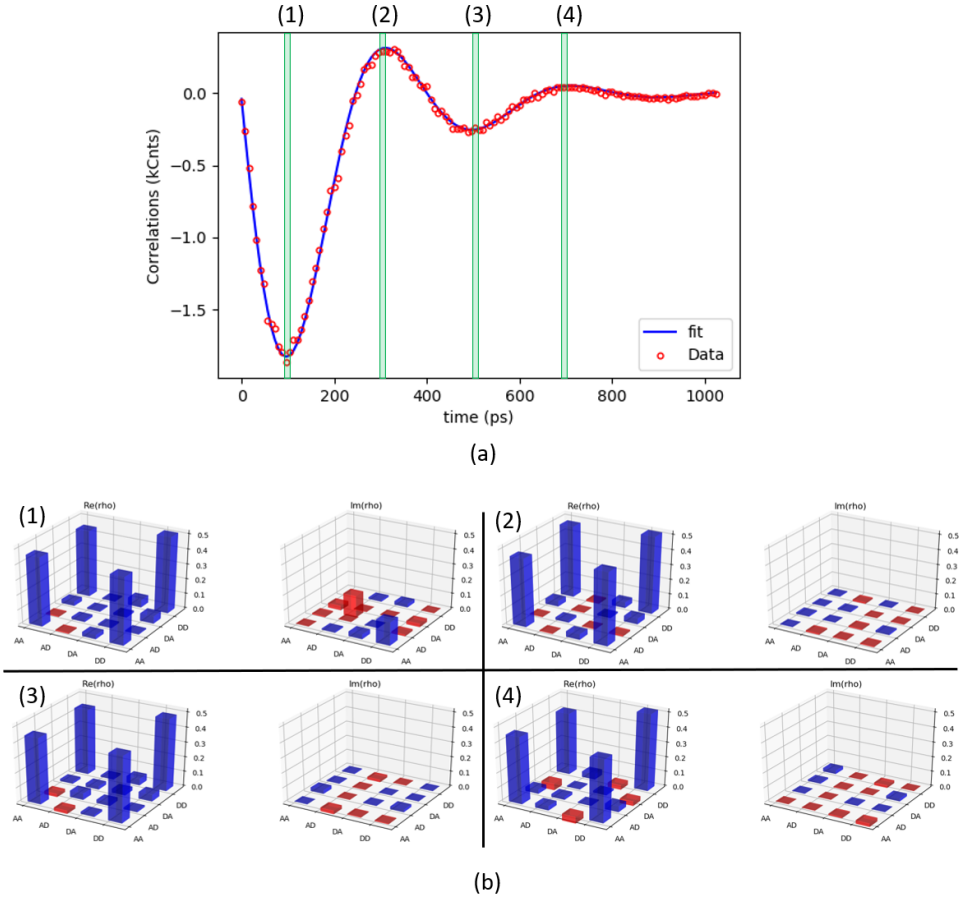

Figure 2.22: (a) Plot of $(AD+DA)-(DD+AA)$ coincidences after two-photon correlation measurements between X and XX with quantum state oscillation between Bell States. Red dots indicate data and blue trace show the fitting with a damped oscillator. The oscillations appear because $(AD+DA)-(DD+AA)$ depicts the state precessing between the two maximally entangled Bell states as predicted in eq. 2.19. The green vertical lines relate to the local maxima and minima of $(AD+DA)-(DD+AA)$ and highlight the time bin with highest concurrence (1) and time bins where the imaginary value of the density matrix is the lowest as depicted in (b). Plot of real and imaginary parts of density matrices.

This was done by fitting the quantum oscillation using the equation of a damped oscillator with the period as a free parameter. This is shown in fig. 2.22 that let us extrapolate a value for the fine-structure splitting of 2598.456 ± 0.04 MHz. The good match between fit and data yield a coefficient of determination R^2 of 0.873. This is a strong indication that precession and lifetime represent the only variables to describe the quantum state evolution. For this set of data, quantum state precession refers to the quantity $(AD+DA)-(DD+AA)$ since the sample's crystallographic orientation was mounted with an offset angle compared to the H,V direction of the quantum state tomography setup. In fact, the exciton, which is approximated by a charged dipole, has its moment lying on a well-defined crystallographic direction onto which the PL emission locks. Along with quantum oscillations, fig. 2.22 shows four density matrices for each of the minima and maxima of the oscillation. They were calculated by maximum likelihood approximation [38], [39] using all 36 possible projections bases for quantum state reconstruction. The higher number of basis enabled a finer calculation of the density matrices although a minimum set of 16 basis is necessary. Density matrices were calculated within the radiative exciton decay with a time bin of 16 ps.

Since the system has undergone a coordinate transformation caused by the offset angle between the sample orientation and the H,V direction analysis, the photons, originally emitted in HV basis, are detected in an unknown state. First, using the tomography code [39], a unitary transformation through a virtual waveplate is applied to rotate the coordinate system towards the target basis AD and secondly the density matrix is calculated using the maximum likelihood approximation. Density matrices evaluated at the peaks of the oscillation in fig. 2.22 exhibit mainly real parts where the outer diagonal elements are dominant. On the other hand, the imaginary parts are negligible except for the case shown in fig. 2.22(b)(1), with opposite sign on the outer diagonal. This is the point where the peak of concurrence is reached. Why is it so?

It can be explained by recalling that the concurrence peak in fig. 2.22(b)(1) occurs right at the beginning of the Qdot decay. Why is the complex part of the density matrix at this specific point the only one that shows a not negligible contribution among all ?

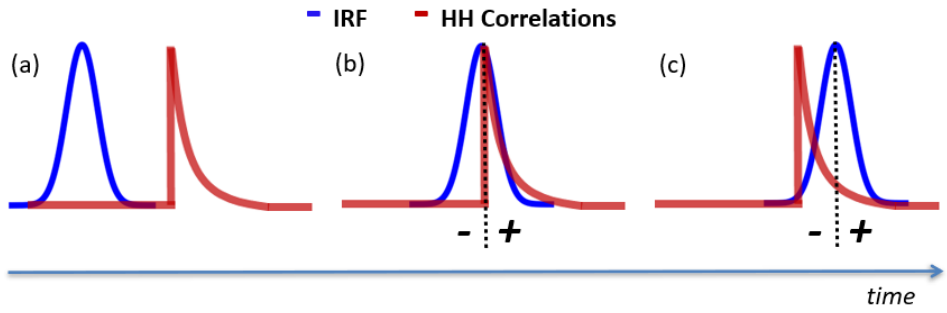

Figure 2.23: Convolution between detector response function (blue trace) and theoretical HH correlations (red trace). Only HH is considered for sake of simplicity. **(a)** No correlations are detected. **(b)** Asymmetric convolution between Detector Response function and emitted photons. Here, there is an unbalanced contribution to the complex part of density matrix. **(c)** Left and right side of the response function can sample photon counts. Here, the phase factor is averaged to zero during convolution.

This fact arises because, once again, the phase factor of the quantum state plays a role in the convolution between the response function and photon correlations during the Qdot radiative decay. In fact, as the detector samples the initial correlations, the convolution records small "frames" of the precession. These "frames" are snapshots of the phase factor at specific time bins. So, at the beginning, the convolution is not balanced due to the asymmetry in emission. As we probe later photons during the decay time, the convolution is balanced and the complex parts of the density matrices are balanced out as confirmed in fig. 2.22(b)(2), (b)(3) and (b)(4). Sketch 2.23 describes this mechanism.

2.8.6. ENTANGLEMENT EVOLUTION

The time evolution of the concurrence was extracted using again the same quantum state tomography code [39]. The concurrence peak value is 94.7%.

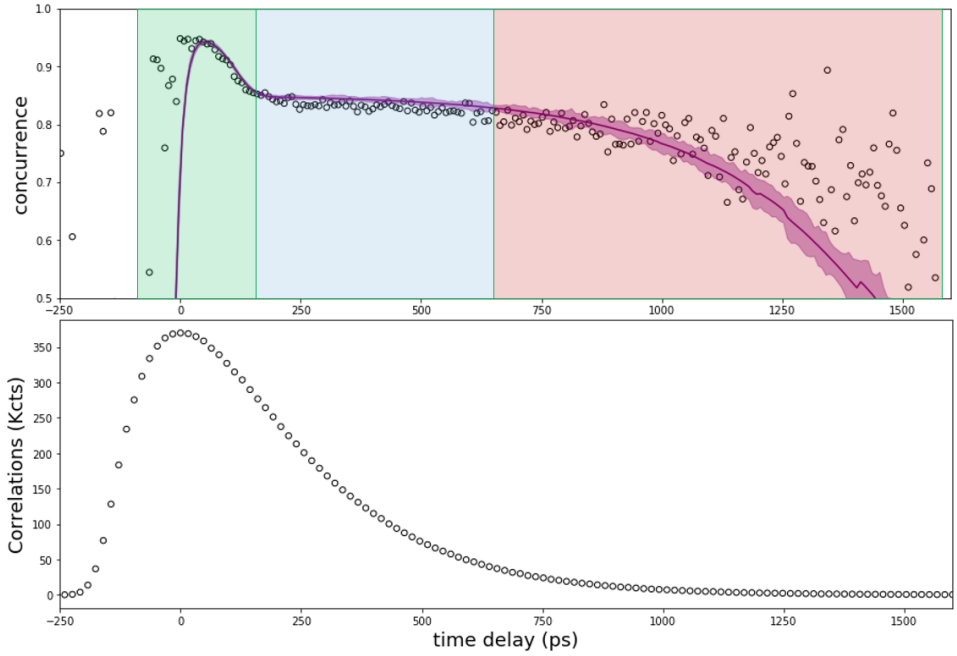

Figure 2.24: (Top) Concurrence from the quantum state tomography measurements. the maximum value is 94.7% and occurs at the limit of the green shaded part that highlights the steep early rise in sampled correlation by the detection system. In the blue section of the graph the impact of the phase term on eq. 2.18 drops down the concurrence above 80%. At last, meaningful coincidences are not probed anymore and the concurrence oscillates up and down (red part). Simulation landscape (purple line) demonstrates the combined effect of finite detection time resolution, fine-structure splitting and the not perfect single photon emission. Trend in simulation well follows the behavior shown in measurement. (Bottom) Exciton lifetime.

The agreement of the concurrence model proposed by Fognini et al. [12] with the concurrence evolution shown from the measurement demonstrates how the degree of entanglement does indeed mainly depend on the fine-structure splitting and the detection system resolution. The model predicts the presence of three different regions in the

concurrence landscape and is further highlighted in this experiment. To simulate the concurrence evolution, we applied the maximum likelihood approximation using the experimentally measured photon rate for both biexciton and exciton transitions. The concurrence C is mathematically described by:

$$C(\rho(p_{ij}))_{\Delta t} = C\left(\rho\left(|\langle ij|\Psi(t)\rangle|^2 n(t,\tau_x)\right) * g(t)dt\right) \tag{2.20}$$

where ρ is the reconstructed density matrix per time bin Δt from the state tomography measurement p_{ij}. As the state is evolving with time, $C(\rho(p_{ij}))_{\Delta t}$ will be reduced by the exponential phase factor that acts as an averaging term. This explains why, at the beginning, the concurrence landscape shows an early steep part. Here, the coincidences rise quickly due to the detector response function $g(t)$ that samples increasing number of correlations immediately after excitation. Later in time, the phase averaging of the exponential term in eq. 4.1 starts to impact the convolution, that is where the concurrence falls to an average value around 85%. In the end, the amount of meaningful correlations drops significantly because of the finite lifetime of the exciton decay and the dark counts. This is where false correlations start to matter. It is interesting to note that the plateau region extends over a long time interval although the number of detected correlations keeps dropping. Moreover the error is also negligible until 1000 ps indicating that the concurrence can be computed and yield meaningful results even if the exciton and biexciton photons drop significantly.

For the sake of completeness, we also define a time-averaged concurrence $\bar{C}(\rho)$ that is weighted with the amount of detected photon per time bin $n(t)$ [41]:

$$\bar{C}(\rho) = \lim_{T\to\infty} \frac{1}{N_0} \int_{-T}^{T} n(t) C(\rho(p_{ij}))_{\Delta t} dt \tag{2.21}$$

Since entanglement is a time-integrated quantity, $\bar{C}(\rho)$ provides us with a figure of merit to quantify the amount of usable photons over the Qdot's radiative decay time during an entanglement experiment. This particular case has yielded $\bar{C}(\rho)$ of 86.0%.

It is important to note that the simulation is only based on measured variables such as single-photon purity from second-order correlation function, fine-structure splitting from quantum oscillation, exciton and biexciton brightness from the spectra, and finally dark counts. So, the simulation *does not contain any free fitting parameters*. Since it describes the entanglement evolution so precisely we can conclude that the Qdot does not dephase over its entire lifetime. Below we list the values that we cast in the model.

We used a fine-structure splitting value and exciton lifetime of 2598.456 MHz and 204 ps respectively, both extracted from fitting in fig. 2.22, a dark count rate of 0.5 and 1.0 Hz for the exciton and biexciton detector and $g^{(2)}_{XX}(0) = 0.05$. Both dark counts and $g^{(2)}_{XX}(0)$ lower the entanglement level. Dark counts were included with the term p_{dc} that was added on top of the noiseless simulated correlations. Spoiled $g^{(2)}_{XX}(0)$ was added by using the density matrix for uncorrelated light to the already reconstructed density matrix. We did not add the contribution of exciton $g^{(2)}_{X}(0)$ that is negligible compared to the biexciton $g^{(2)}_{XX}(0)$:

$$\rho_{\Delta t} = \rho(p_{ij} + p_{dc})_{\Delta t} + \frac{g^{(2)}_{XX}(0)}{4}\mathbb{1} \tag{2.22}$$

The number of cross correlations to be cast into the density matrix evaluation algorithm was normalized by both the laser repetition rate of 320 MHz and integration time of 600 seconds. Count rates for exciton and biexciton decay were 90kC and 78kC per second respectively. The error of the concurrence was estimated based on a Monte-Carlo simulation assuming counting statistics of $\sqrt{N}$. For each concurrence value the error was simulated with 10 repetitions.

Convolution in eq. 2.18 was computed with the instruments response function $g(t)$ evaluated from measurement with a similar approach explained in [12]. Let us take a closer look. We know that simulation is very sensitive to the detection response function g(t). Direct measurement will fall short because the pulsed laser generates wave packets that are too different in spectrum compared to the Qdot's emission profile. The reason is that chirp introduced within the notch filters will stretch the picosecond pulses in an undefined manner. The solution to this matter is to extract the response function directly from the set of the tomography measurements. Let's consider the rising part of the correlations with the least oscillations, such as RR and LL in our case that resemble the following equation:

$$f(t) = \Theta(t)e^{\frac{t}{\tau_x}} * g(t) \approx \Theta(t) * g(t) \tag{2.23}$$

where, $\Theta(t)$ is the Heaviside function, τ_x the exciton lifetime, and * denotes the convolution operator. Approximation is allowed around $t = 0$ because the $g(t)$ half width at half maximum, that is roughly 60 ps, is shorter than the Qdot lifetime τ_x (204 ps). Finally, the differentiation of $f(t)$ yields $g(t)$.

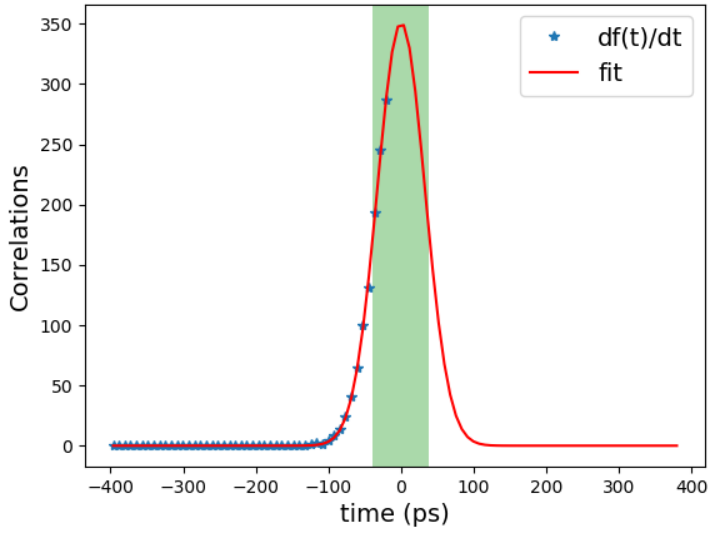

Figure 2.25: Gaussian fit of the mirrored smoothed $RR + LL$ correlations. The shaded green area represents the Full Width Half Maximum with value 65.6 ps.

Bearing in mind these steps, we started by summing the RR and LL correlation to retrieve a higher signal to noise ratio, than only RR and LL alone. We applied Savitzki-Golay filter to smoothen the shape of $f(t)$ and to be less affected by noise before performing a stepwise differentiation of $f(t)$. From $\frac{df(t)}{dt}$ we select the portion from negative times until the maximum which contains the full information of the instrument response function $g(t)$. Knowing that both SNSPDs present symmetric Gaussian timing jitter, we can reconstruct the raw $g(t)$ by mirroring $g(t)$ along its maximum towards positive times and performing a Gaussian fit. The outcome was properly normalized before being cast into the algorithm.

With the above experimental analysis we have presented a model that *does not require any free fit parameters* and allows to predict the entanglement evolution to very high degree of accuracy. The model predicts a peak concurrence of 95.3% that is slightly off compared to the measured value of 94.7%. Showing good match between theory and data, we can conclude that this model can explain entanglement evolution without the need of taking into account any dephasing mechanism at the Qdot level. Hence, we can conclude that the measured Qdot is basically dephasing free.

2.9. CONCLUSION

We have demonstrated the validity of the model reported in [12] that predicts dephasing free entanglement over the entire exciton decay time for an AlGaAs Qdot. Especially Gallium contains significant nuclear spin which confirms how that interaction with the nuclei is not a relevant dephasing mechanism within the exciton radiative decay time. Nevertheless, reaching a steady peak concurrence level of one all along the exciton decay does still remain a challenge. The measured degree of entanglement is dampened by the timing jitter and the dark counts of the detection system on one hand, and the single photon emission purity of the X and XX together with the fine-structure splitting of the Qdot on the other. Although the entanglement measurement relied on state-of-the-art detection system, the quest for perfect entanglement from a Qdot source does still necessitates another piece to be complete. As we will see in chapter 4 this missing part can be provided by non-linear crystals that are capable of compensating the quantum state precession by modulating the phase of the Qdot emission.

REFERENCES

[1] P. Senellart, G. Solomon, and A. White. High-performance semiconductor quantum-dot single-photon sources. *Nature Nanotechnology*, 12(11):1026–1039, 11 2017.

[2] J. Claudon, J. Bleuse, N. S. Malik, M. Bazin, P. Jaffrennou, N. Gregersen, C. Sauvan, P. Lalanne, and J. M. Gérard. A highly efficient single-photon source based on a quantum dot in a photonic nanowire. *Nature Photonics*, 4(3):174–177, 3 2010.

[3] G. Bulgarini, M. E. Reimer, M. Bouwes B., K. D. Jöns, D. Dalacu, P. J. Poole, E. P.A.M. Bakkers, and V. Zwiller. Nanowire waveguides launching single photons in a Gaussian mode for ideal fiber coupling. *Nano Letters*, 14(7):4102–4106, 7 2014.

[4] A. Rubenok, J. A. Slater, P. Chan, I. Lucio-Martinez, and W. Tittel. Real-world two-photon interference and proof-of-principle quantum key distribution immune to detector attacks. *Physical Review Letters*, 111(13), 9 2013.

[5] R. Singh and G. Bester. Nanowire quantum dots as an ideal source of entangled photon pairs. *Physical Review Letters*, 103(6), 8 2009.

[6] M. E. Reimer, G. Bulgarini, A. Fognini, R. W. Heeres, B. J. Witek, M. A.M. Versteegh, A. Rubino, T. Braun, M. Kamp, S. Höfling, D. Dalacu, J. Lapointe, P. J. Poole, and V. Zwiller. Overcoming power broadening of the quantum dot emission in a pure wurtzite nanowire. *Physical Review B*, 93(19), 5 2016.

[7] J. Cassidy and M. Zamkov. Nanoshell quantum dots: Quantum confinement beyond the exciton Bohr radius. *Journal of Chemical Physics*, 152(11), 3 2020.

[8] K. Brunner, U. Bockelmann, G. Abstreiter, M. Walther, G. Bohm, G. Trankle, and G. Weimann. Photoluminescence from a Single GaAs/AlGaAs Quantum Dot. *Physical Review Letters*, 69(22), 11 1992.

[9] R. Bratschitsch and A. Leitenstorfer. Artificial atoms for quantum optics. *Nature Materials*, 5(11):855–856, 11 2006.

[10] P. Hawrylak. Excitonic artificial atoms: Engineering optical properties of quantum dots. *Physical Review B*, 60(8), 8 1999.

[11] L. Jacak, A. Wójs, and P. Hawrylak. *Quantum Dots*. Springer Berlin Heidelberg, 1998.

[12] A. Fognini, A. Ahmadi, M. Zeeshan, J. T. Fokkens, S. J. Gibson, N. Sherlekar, S. J. Daley, D. Dalacu, P. J. Poole, K. D. Jöns, V. Zwiller, and M. E. Reimer. Path to perfect photon entanglement with a quantum dot. *arXiv preprint arXiv:1710.10815*, 10 2017.

[13] D. Huber, M. Reindl, J. Aberl, A. Rastelli, and R. Trotta. Semiconductor quantum dots as an ideal source of polarization-entangled photon pairs on-demand: A review. *Journal of Optics*, 20(7), 7 2018.

[14] H. Jayakumar, A. Predojević, T. Huber, T. Kauten, G. S. Solomon, and G. Weihs. Deterministic photon pairs and coherent optical control of a single quantum dot. *Physical Review Letters*, 110(13), 3 2013.

[15] T. H. Stievater, Xiaoqin Li, D. G. Steel, D. Gammon, D. S. Katzer, D. Park, C. Piermarocchi, and L. J. Sham. Rabi oscillations of excitons in single quantum dots. *Physical Review Letters*, 87(13), 2001.

[16] S. Stufler, P. Machnikowski, P. Ester, M. Bichler, V. M. Axt, T. Kuhn, and A. Zrenner. Two-photon Rabi oscillations in a single Inx Ga1-x As GaAs quantum dot. *Physical Review B - Condensed Matter and Materials Physics*, 73(12), 2006.

[17] L. Ostermann, T. Huber, M. Prilmüller, G. S. Solomon, H. Ritsch, G. Weihs, and A. Predojević. Coherent two-photon excitation of quantum dots. In *Quantum Optics*, volume 9900, page 99000T. SPIE, 4 2016.

[18] A. Galler and T. Feurer. Pulse shaper assisted short laser pulse characterization. *Applied Physics B: Lasers and Optics*, 90(3-4):427–430, 3 2008.

[19] A. Monmayrant, S. Weber, and B. Chatel. A newcomer's guide to ultrashort pulse shaping and characterization. *Journal of Physics B: Atomic, Molecular and Optical Physics*, 43(10), 5 2010.

[20] M. Gong, K. Duan, C. F. Li, R. Magri, G. A. Narvaez, and L. He. Electronic structure of self-assembled InAs InP quantum dots: Comparison with self-assembled InAs GaAs quantum dots. *Physical Review B - Condensed Matter and Materials Physics*, 77(4), 1 2008.

[21] C. Weisbuch and B. Vinter. *Quantum semiconductor structures : fundamentals and applications*. Academic Press, 1991.

[22] M. Isarov, L. Z. Tan, J. Tilchin, F. T. Rabouw, M.I. Bodnarchuk, R.J.A. Van Dijk-Moes, R. Carmi, Y. Barak, A. Kostadinov, I. Meir, Daniel Vanmaekelbergh, Maksym V. Kovalenko, Andrew M. Rappe, and Efrat Lifshitz. Polarized emission in II-VI and perovskite colloidal quantum dots. *Journal of Physics B: Atomic, Molecular and Optical Physics*, 50(21), 10 2017.

[23] M. Bayer, G. Ortner, O. Stern, A. Kuther, A. A. Gorbunov, A. Forchel, P. Hawrylak, S. Fafard, K. Hinzer, T. L. Reinecke, S. N. Walck, J. P. Reithmaier, F. Klopf, and F. Schäfer. Fine structure of neutral and charged excitons in self-assembled In(Ga)As/(Al) GaAs quantum dots. *Physical Review B - Condensed Matter and Materials Physics*, 65(19):1953151–19531523, 5 2002.

[24] B. J. Witek, R. W. Heeres, U. Perinetti, E. P.A.M. Bakkers, L. P. Kouwenhoven, and V. Zwiller. Measurement of the g-factor tensor in a quantum dot and disentanglement of exciton spins. *Physical Review B - Condensed Matter and Materials Physics*, 84(19), 11 2011.

[25] D. Bercioux and P. Lucignano. Quantum transport in rashba spin–orbit materials: A review. *Reports on Progress in Physics*, 78(10), 9 2015.

[26] H W Van Kesteren, E C Cosman, W A J A Van Der Poel, and C T Foxon. Fine structure of excitons in type-II GaAs/AlAs quantum wells. *Physical Review B Condensed Matter*, 41(8):15–1990, 3 1990.

[27] V D Kulakovskii, G Bacher, R Weigand, T Kümmell, A Forchel, E Borovitskaya, K Leonardi, and D Hommel. Fine Structure of Biexciton Emission in Symmetric and Asymmetric CdSe ZnSe Single Quantum Dots. *Physical Review Letters*, 82(8), 2 1999.

[28] T. Campos, P. E. Faria, M. Gmitra, G. M. Sipahi, and J. Fabian. Spin-orbit coupling effects in zinc-blende InSb and wurtzite InAs nanowires: Realistic calculations with multiband kp method. *Physical Review Letters B*, 97(245502), 6 2018.

[29] Y. A. Bychkov and E.I. Rashba. Oscillatory effects and the magnetic susceptibility of carriers in inversion layers. *J. Phys. C: Solid State Phys*, 17:6039–6045, 4 1984.

[30] M.E. Reimer, G. Bulgarini, N. Akopian, M. Hocevar, M. B. Bavinck, M. A. Verheijen, E.P.A.M. Bakkers, L. P. Kouwenhoven, and V. Zwiller. Bright single-photon sources in bottom-up tailored nanowires. *Nature Communications*, 3(737), 3 2012.

[31] M. A.M. Versteegh, M. E. Reimer, K. D. Jöns, D. Dalacu, P. J. Poole, A. Gulinatti, A. Giudice, and V. Zwiller. Observation of strongly entangled photon pairs from a nanowire quantum dot. *Nature Communications*, 5(5298), 10 2014.

[32] Andreas Fognini ElConRoM. Available at https://github.com/afognini/.

[33] C. H. Teng, L. Zhang, T. A. Hill, B. Demory, H. Deng, and P. C. Ku. Elliptical quantum dots as on-demand single photons sources with deterministic polarization states. *Applied Physics Letters*, 107(19), 11 2015.

[34] Hanbury-Brown and R.Q. Twiss. Correlation of photons in two coherent beams of light. *Nature*, 177(4497):27–29, 1 1956.

[35] L. Schweickert, K. D. Jöns, K. D. Zeuner, S. F. Covre Da Silva, H. Huang, T. Lettner, M. Reindl, J. Zichi, R. Trotta, A. Rastelli, and Val Zwiller. On-demand generation of background-free single photons from a solid-state source. *Applied Physics Letters*, 112(9), 2 2018.

[36] R. Keil, M. Zopf, Y. Chen, B. Höfer, J. Zhang, F. Ding, and O. G. Schmidt. Solid-state ensemble of highly entangled photon sources at rubidium atomic transitions. *Nature Communications*, 8, 5 2017.

[37] E. Toninelli, B. Ndagano, A. Vallés, B. Sephton, I. Nape, A. Ambrosio, F. Capasso, M.J. Padgett, and A. Forbes. Concepts in quantum state tomography and classical implementation with intense light: a tutorial. *Advances in Optics and Photonics*, 11(1):67, 3 2019.

[38] D. F.V. James, P.G. Kwiat, W. J. Munro, and A. G. White. Measurement of qubits. *Physical Review A - Atomic, Molecular, and Optical Physics*, 64(5):15, 2001.

[39] T. Fokkens, A. Fognini, and V. Zwiller. Tjeerd Fokkens, Andreas Fognini, Val Zwiller Optical Quantum Tomography Code. Available at https://github.com/afognini/Tomography/., 2017.

[40] Y. H. Huo, A. Rastelli, and O. G. Schmidt. Ultra-small excitonic fine structure splitting in highly symmetric quantum dots on GaAs (001) substrate. *Applied Physics Letters*, 102(15):152105 – 152109, 4 2013.

[41] A. Fognini, A. Ahmadi, S. J. Daley, M. E. Reimer, and V. Zwiller. Universal finestructure eraser for quantum dots. *Optics Express*, 26(19), 9 2018.

3

REDUCING TIMING-JITTER WITH LOW-NOISE AMPLIFIERS

This chapter presents the new generation of cryo-amplifiers designed at Single Quantum B.V. with particular focus on their impact on time resolution. The lower electrical noise of these cryo-amps due to decreased thermal noise at low temperatures combined with fine radio-frequency engineering have enabled the realization of detection systems with an improvement of up to 60% in timing-jitter compared to the standard room temperature readout scheme.

3.1. REDUCING TIMING-JITTER WITH LOW-NOISE AMPLIFIERS

In the previous chapter we analyzed the detrimental impact of the timing-jitter on the level of the measurable entanglement. This led us to investigate how the RF amplification stage of the readout circuit affects the overall time resolution provided by the SNSPD detection system in response to the arrival of a single photon.

Cryogenic amplifiers provide the advantage over standard room temperature amplifiers that the Johnson–Nyquist electrical noise is decreasing significantly. This noise is linearly dependant on the temperature and does intrinsically depend on the thermal motion of the electrons and holes inside the electronic components [1]. Given the lower operating temperature, cryo-amplifiers drastically reduce the noise, hence improving the signal-to-noise ratio. As a result, the timing-jitter, which is highly dependant on the signal-to-noise ratio, benefits from such amplifiers. A rough schematic of the amplification circuit is depicted in 3.1.

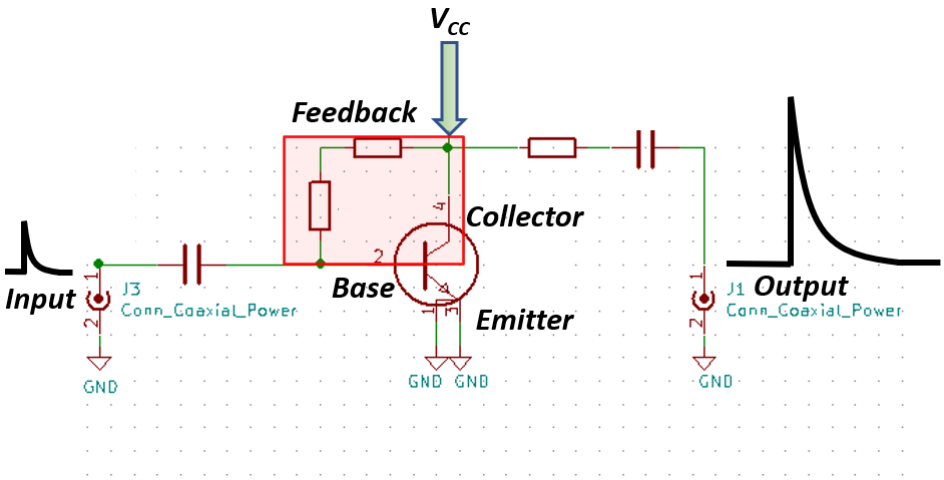

Figure 3.1: (a) Schematic of the broadband amplifier in common emitter configuration. Red box highlights the feedback network, V_{cc} is the voltage applied to base and collector. Values of the elements and parts cannot be disclosed.

The amplifier deploys an NPN bipolar junction transistor (BJT) in a negative feedback common emitter (CE) configuration. In the CE mode, the SNSPD output signal enters the circuit in (J3) and is therefore applied between the base and the emitter. The output amplified version of the input signal exits the circuit at the collector terminal (J1). The negative feedback from collector to base is added to increase temperature stability, lowering the amount of distortion and flattening the gain over a wide bandwidth [2]. Bandwidth is critical to achieve amplification of broadband SNSPD signal pulses up to several GHz. The amplified SNSPD output pulse needs to be amplified on a second stage at room temperature by an additional 40 dB since the peak voltage from the SNSPD is typically in the order of a few mV. The rising question now is, does the second amplification stage worsen the signal-to-noise ratio given that it works at room temperature?

The answer is that its contribution to noise is completely negligible. Why? This result stems from Friis's formula for noise used to calculate the signal-to-noise ratio of a multistage amplifier. The formula states that the first amplifier in a chain has the most significant effect on the total noise figure because the noise figures of the following stages are reduced by their stage gains [3]. In case of a two stage amplifier the total Noise Factor reads:

$$F_{tot} = F_1 + \frac{F2-1}{G_1} \tag{3.1}$$

F_1 and F_2 are the Noise Factors for the cryo-amplifier and the room-temperature amplifier respectively and G_1 is the power gain of the cryo-amplifier. The Noise Factor is a parameter describing the degradation of the signal-to-noise ratio for the device under test and is basically the ratio between the signal-to-noise ratio at the input and the signal-to-noise ratio at the output [4]. The Noise Factor is also conveniently expressed in Decibels and is referred as noise figure (NF):

$$NF = 10log_{10}\left(\frac{SNR_{In}}{SNR_{Out}}\right) \tag{3.2}$$

Lowest Noise Factors mean that the amplification stage does not enhance noise so that more accurate and precise time stamping is possible.

From Friis's formula follows that the first amplifier must show the lowest possible noise figure. For such reason the room-temperature second stage amplifier does not play a role in noise enhancement. The signal at the second stage has typically a value of few hundreds of mV and is high enough to trigger a comparator and the consequent counting electronics. This is shown in fig. 3.2.

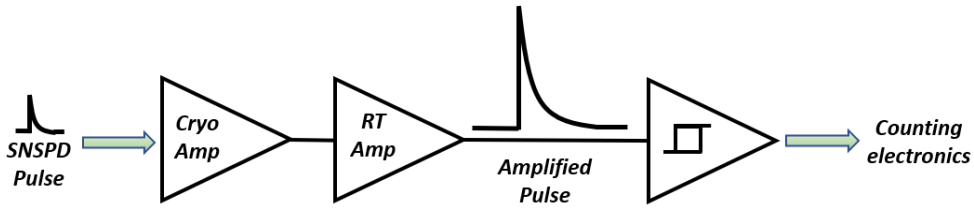

Figure 3.2: RF chain consisting of first stage cryo-amplifier, second stage room-temperature amplifier, and a comparator that outputs a digital signal when the pulse higher than an arbitrary trigger level set by the user.

A Vector Network Analyzer (VNA) from Rhode & Schwarz was used to characterize the performance of the broadband amplifier. The VNA allows to measure the Scattering parameters to quantify losses and transmission over a network. The VNA performs such measurements by injecting a sweep of single tone waves into the amplifier under test and probes the response to this stimuli. As sketched in fig. 3.3, the VNA measures the scattering parameters S_{11} (input reflection) and S_{22} (output reflection) that indicate the reflection characteristics at either ports 50 ohm terminated and also the reflection characteristics from one port to the other in forward S_{21} (gain)and reverse reflection S_{12} (reverse isolation).

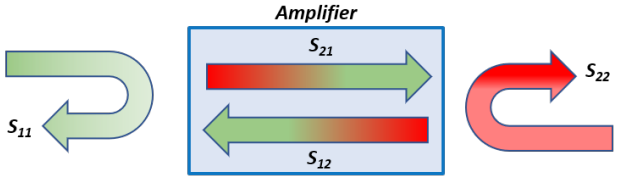

Figure 3.3: Scattering parameters: S_{11} (input reflection), S_{22} (output reflection), S_{21} (forward reflection/gain) and S_{12} (reverse isolation).

Moreover, the Smith Chart enables to perform a quantification of the signal reflections due to the impact of the input and output impedance along the signal travel path. Since the impedance can be represented by the sum of a real and an imaginary part, the VNA uses this format to plot the complex reflection coefficient in a vector form where magnitude and phase are shown.

The amplifier was designed to match the 50 ohm transmission line in order to maximize the power transmission. From the maximum power transfer theorem [5] which states that "maximum power transfer occurs when the load impedance is equal to the complex conjugate of the source impedance", the source and load impedances were properly tuned with an adequate combination of passive elements for the matching network. The fine tuning of these elements was possible by real-time investigation of the Smith Chart. The addition of the right elements in the matching network pushes the matching into the center point of the Smith Chart (50 Ω point).

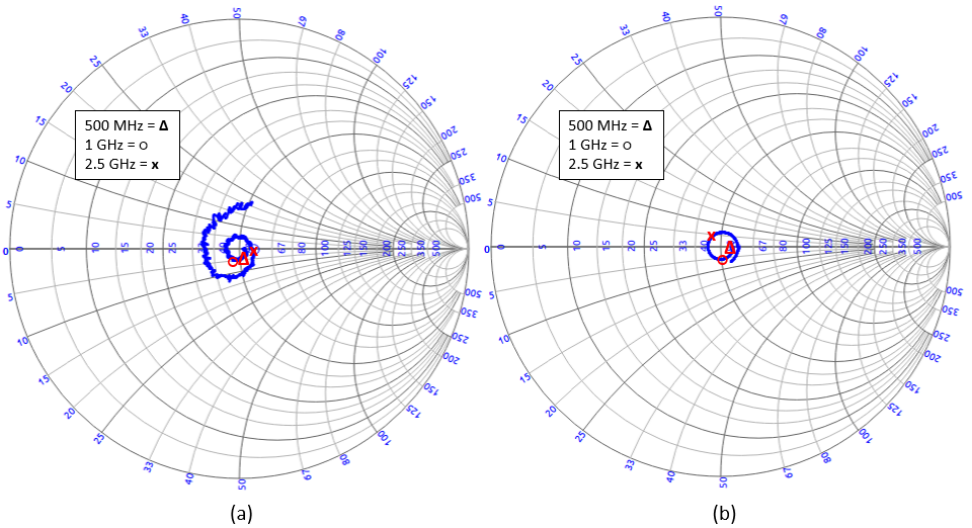

Figure 3.4: Smith chart of S_{11} (a) and S_{22}(b). In (a) the matching deteriorates towards higher frequencies. Starting at the middle of the Chart the matching spirals slightly outward from 2.5 Ghz on. Above this values, the RF waves are reflected more. In (b) there is a clear indication on how much of the output signal is delivered to the load. Signal reflections draw a tight circle around the center proving good matching at the output port.

At high frequencies, RF traveling waves are comparable to the length of the wiring. If the transmission line is not terminated with the characteristic impedance for each spectral component, that specific signal tone will not be fully absorbed by the load and partially reflected back to the source. As a consequence, the envelope of the RF signal along the transmission line will show the profile of standing waves.

Standing waves due to impedance mismatch are quantified by the standing wave ratio (VSWR), that is the ratio of the partial standing wave's amplitude between its maximum and minimum value along the line. The VNA can measure the incident and reflected waves directly during a frequency sweep, and the voltage standing wave ratio (VSWR) is displayed to clearly show at which wavelengths reflections occur.

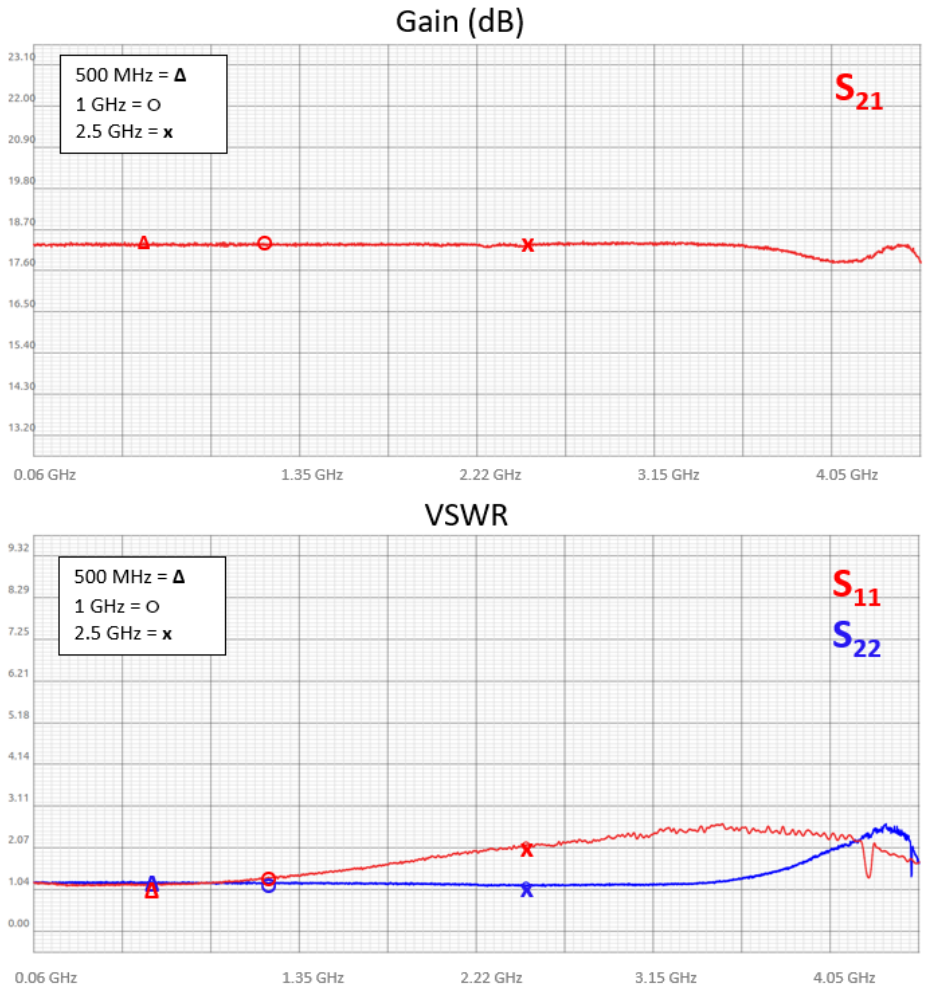

Figure 3.5: **(Top)** Magnitude of S_{21} parameter (gain). The amplification of the cryo-amplifier is roughly 18 dB. **(Bottom)** VSWR for S_{11} (red trace) (a) and S_{22} (blue trace). Both traces demonstrate the presence of standing waves due to reflections at either ends of the amplifier. Input reflection is higher than output reflection.

The graph 3.5 of the VSWR highlights the amazing properties of the amplifier for the output reflection that is basically 1 up to 3 GHz. Input reflection instead deviates from perfect behavior starting at 1 GHz and reaches a value of 2 at 2.5 GHz meaning that roughly 30% of the spectral components of the signal are reflected back. The mismatch losses, that tell us how much of the reflected signal is transmitted through the device, reach a level of about 5% of the reflected signal, namely 1.5% of the initial input signal. In this sense the amplifier rules out any afterpulsing.

3.1.1. NOISE FIGURE MEASUREMENT

With the help of a spectrum analyzer we measured the noise figure at 77 K and room temperature (see fig. 3.6). The noise floor stands well below 1 dB until 2 GHz. The peaks present in the noise figure are due to external noise sources, for instance Bluetooth at 2.5 GHz and WiFi signals at 900MHz. These are completely suppressed by proper shielding in the cryostat.

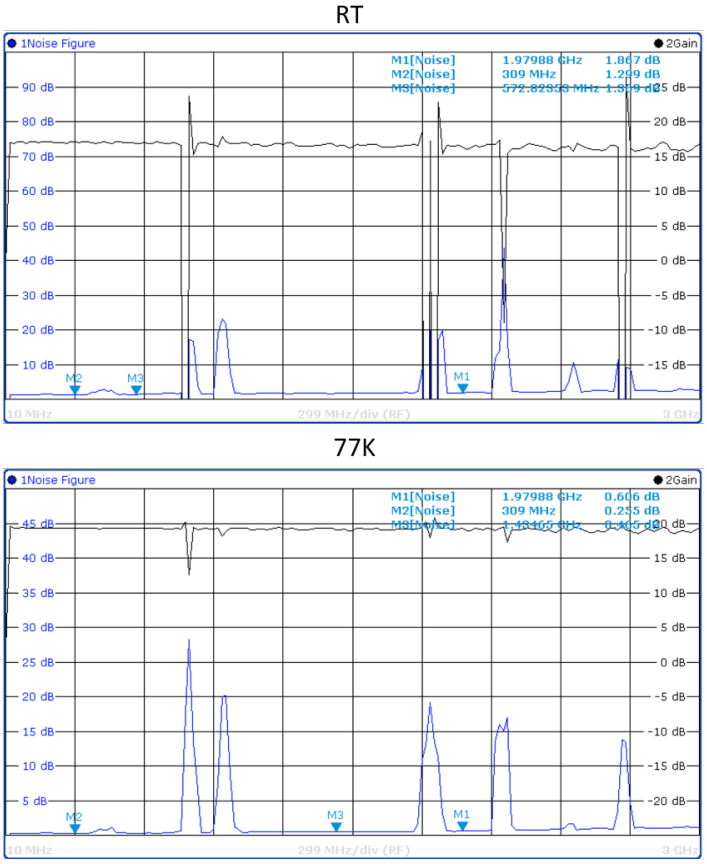

Figure 3.6: **(Top)** Noise figure with span until 3 GHz (Blue trace) at 77K. **(Bottom)** Noise figure with span until 3 GHz at room temperature. Black trace shows the power gain.

The comparison shows that cryo-cooling makes the amplification between 3 to 5 times less noisy as shown in the noise figure measurements in fig. 3.6. These values from the comparison are highlighted by the markers M1 and M2 set at 309 MHz and 1.98 GHz respectively. We can now demonstrate how noise reduction improves the time resolution of the SNSPD detection system.

3.1.2. JITTER MEASUREMENTS

Now we will examine the influence of the reduced noise on the SNSPD's jitter. The setup to measure timing-jitter is shown in fig. 3.7. A pulsed laser at a center wavelength of 1064 nm with a width of 4.2 ps and repetition rate of 48 MHz was fiber coupled to an optical attenuator to decrease the laser power down to the single-photon regime. To perform jitter measurement we used a fast oscilloscope with 4 GHz bandwidth and 40 GS/s to sample the laser trigger and the SNSPD pulse. Timing-jitter is given by the time-difference histogram of the the two signals. This usually follows a Gaussian distribution.

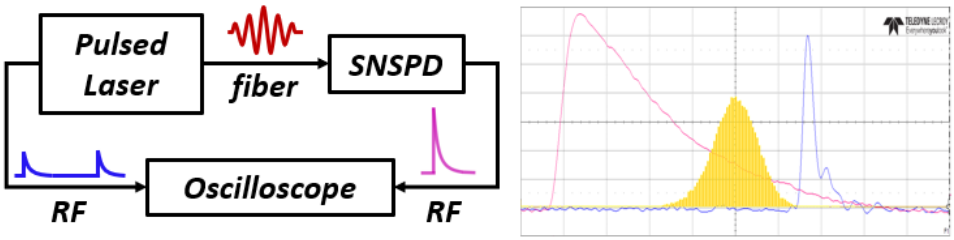

Figure 3.7: **(Left)** Simplified sketch of the timing-jitter measurement setup. **(Right)** Recorded pulses by scope and reconstructed timing-difference histogram.

Fig. 3.8 shows a comparison between two jitter measurements using the same detector. The SNSPD was biased at the same bias current for both cases. The pulse response signal is either amplified by means of a cryo-amplifier or by a RT-amplifier. The measured jitter is roughly 60% better for the cryo-amplifier case.

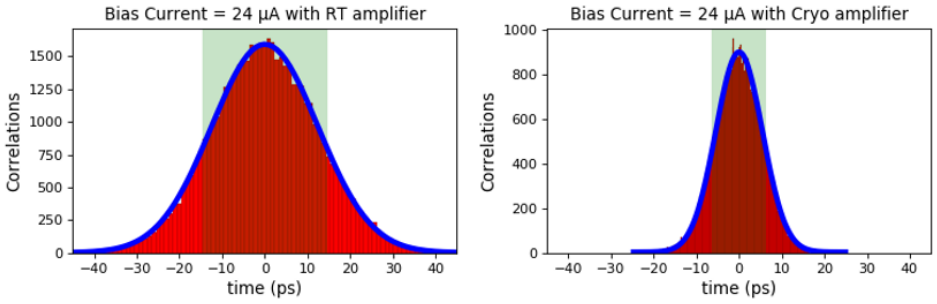

Figure 3.8: **(Left)** System jitter distribution using room temperature amplifiers fitted with a Gaussian function with FWHM equal to 29.3 ps. **(Right)** System jitter distribution using cryogenic amplifiers fitted with a Gaussian function with FWHM equal to 12.9 ps.

Fig. 3.9 shows a comparison between the jitter measured for the same detector at

different bias currents once the pulse response signal is amplified either by means of a cryo-amplifier or a room temperature one. For the same bias current the time resolution enhancement varies always between 55% and 60%. This can be understood by recalling the values of the noise figure. Taking as an example the 309 MHz point, the noise figure read 0.255 dB and 1.299 dB at 77 K and room temperature respectively.

It is also interesting for us to benchmark our device with the ones commercially available such as the LNA 1000 from MiniCircuit whose noise figure at 300 MHz is 3 dB or the LNA amplifier PE15A1007 whose noise figure at 300 MHz is always above 2.2 dB up to 3 GHz. Hence, we can claim that our solution outperforms the amplifiers available on the market.

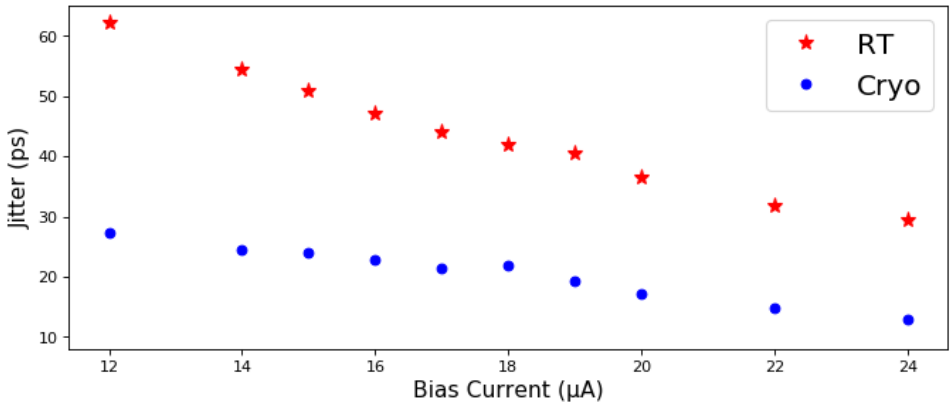

Figure 3.9: System jitter dependence on bias current for the same detector measured at room temperature (RT) and cryo-environment (77 K).

Furthermore, as argued in [6], a higher bias current amplifies the photon response pulse and improves the signal-to-noise ration. This is because the noise generated by the amplifier remains constant whereas the pulse amplitude produced by the SNSPD is proportional to the bias current. Thus, this effect decreases the jitter for larger bias currents. Fig. 3.9 reveals this mechanism by highlighting how the increase in bias current lowers the system jitter.

Moreover we see that the decay in system jitter tends to a plateau at high bias currents which is when the main contribution to the system jitter is not given anymore by the electrical noise but by the the intrinsic photon detection mechanism within the SNSPD.

3.1.3. IMPACT OF JITTER OF THE ENTANGLEMENT EVOLUTION

In the previous chapter, we discussed how the time resolution has an impact on the entanglement evolution. In light of the improvements on the amplification stage, we can predict the entanglement evolution of the Qdot source using the "dephasing free Quantum dot" model by varying the timing-jitter of the detection system.

The three curves in fig. 3.10 show the effect of Gaussian detection response func-

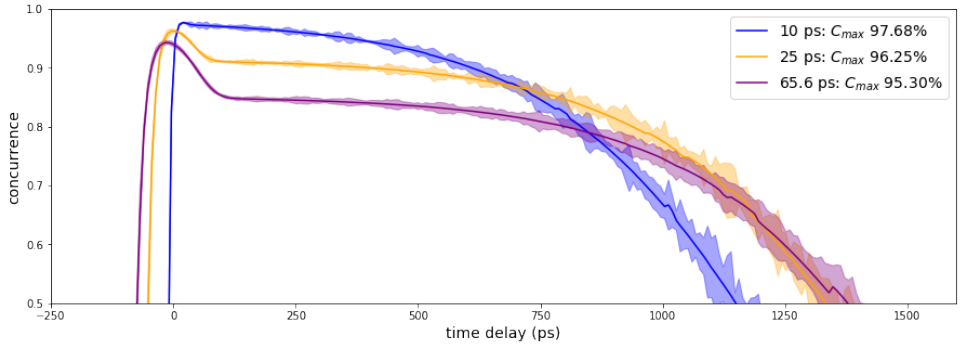

Figure 3.10: Curves of the free-dephasing Qdot simulation using 10, 25 and 65.6 ps time resolution for comparison. A steeper instrument response function leads to faster and higher ascend to the initial peak value. The ascend occurs at earlier times for higher FWHM because the detection can probe initial correlations at its tails.

tions at 10, 25 and 65.6 ps FWHM. All other variables were kept equal to the ones of the AlGaAs Qdot. Higher timing-jitter lowers the peak and the plateau value in the concurrence evolution. Moreover, unity entanglement is never reached due the imperfect signal photon purity $g^2(0) = 0.05$. However, the plateau lays closer to the peak value for narrower FWHM. This finding is encouraging because of the higher amount of usable entangled photons. To confirm this, we calculated the time-averaged concurrence $\bar{C}(\rho)$ for these new curves. With 10 ps and 25 ps FWHM we can reach average concurrence values $\bar{C}(\rho)$ of 93.4% and 90.1% that is over 4% enhancement compared to the real experimental case. Lastly, we note that the concurrence drops to 0.5 denoting that the transition towards the classical regime occurs faster for narrower FWHMs. This is because the measurable entanglement becomes more sensitive to the dark counts level.

In order to understand the significance of these results and what they imply, we refer to the application of entanglement in the E91 QKD protocol [7]. To ensure correct operation of the protocol the photon pair must be perfectly entangled because the transmitter and the receiver have to always measure orthogonal polarizations with no error. If this condition occurs, any attempt of eavesdropping will compromise quantum entanglement. In fact, the trasmitter and receiver perform a Bell test experiment [8, 9] to spot the presence of an eavesdropper by knowing that maximally entangled photons will violate the Bell inequality. The presence of an eavesdropper will otherwise introduce local realism that is detected as classical correlations. However, if the experimental conditions do not provide perfectly entangled photons, Bell inequality is either never violated or error rate becomes not tolerable making the protocol useless or unsafe.

Fig. 3.10 indicates that an overall detection time resolution as low as 10 ps could provide almost fully entangled photons. However, the laser excitation together with all the elements in the optical photons path and the counting electronics are themselves sources of jitter. Combining all of these we already reach an overall jitter value of several picoseconds. For this reason an alternative solution is needed and can be found in the fine-structure splitting compensation schemes.

3.2. CONCLUSION

In this chapter we have demonstrated the benefit of a new generation of cryogenic amplifiers over standard room temperature ones. Jitter measurements show that RF signal matching and decreased thermal noise have a great impact onto the detection time resolution. Finally, through simulation, we have seen that improving the time resolution will possibly allow for higher measurable entanglement. However, given the impossibility to wash out completely the sources of jitter in an entanglement measurement, a possible correction to this drawback is to compensate the quantum state precession by phase modulating the Qdot light. This topic will be the focus of next chapter.

REFERENCES

[1] H. Nyquist. Thermal agitation of electric charge in conductors. *Physical Review*, 32(1), 7 1928.

[2] P. Horowitz and W. Hill. *The Art Of Electronics*. Cambridge University Press, 2nd edition edition, 1989.

[3] Friss H.T. Noise Figures of Radio Receivers. *Proceedings of the IRE*, 32(7):419–422, 7 1944.

[4] H.A. Haus. Noise Figure Definition Valid From RF to Optical Frequencies. *IEEE Journal of selected topics in quantum electronics*, 6(2):240–247, 3 2000.

[5] C S Kong. A General Maximum Power Transfer Theorem. *IEEE Transactions on education*, 38(3), 9 1995.

[6] L. You, X. Yang, Y. He, W. Zhang, D. Liu, W. Zhang, L. Zhang, L. Zhang, X. Liu, S. Chen, Z. Wang, and X. Xie. Jitter analysis of a superconducting nanowire single photon detector. *AIP Advances*, 3(7), 8 2013.

[7] A. . Ekert. Quantum Cryptography Based on Bell's Theorem. *Physical Review Letters*, 67(6), 8 1991.

[8] J. S. Bell. On the Problem of Hidden Variables in Quantum Mechanics. *Reviews of Modern Physics*, 38(3):447–452, 8 1964.

[9] A. Ling, M. Peloso, I. Marcikic, A. Lamas-Linares, and C. Kurtsiefer. Experimental E91 quantum key distribution. In *Advanced Optical Concepts in Quantum Computing, Memory, and Communication*, volume 6903, page 69030U. SPIE, 2 2008.

4

FINE-STRUCTURE SPLITTING ERASURE SCHEME WITH SAWTOOTH PHASE MODULATION

This chapter aims at proving the feasibility of the fine structure splitting compensation scheme based on serrodyne phase modulation. Experiments, carried out at KTH Quantum Nano-Photonics group, demonstrated efficient photon frequency shift with an RF signal generated by the use of a fast digital-to-analog converter coupled to a pattern generator. Together, they enable the generation of arbitrary waveforms with sampling rate just below 9 Gigasamplepersecond (Gsps). The striking feature of this device lies within its clocking module that has the ability to phase align any arbitrary waveforms with an external clock. In this particular application, the external clock is the laser trigger of a picosecond laser source centered at 80 MHz repetition rate.

4.1. MOTIVATION

The holy Grail that quantum optical information has been questing for, is a source of entangled pairs of single photons to be generated on-demand, namely just when requested. Over the decades many schemes have been proposed ranging from spontaneous parametric down conversion, color center in diamonds, single dye molecules to semiconductor nanocrystal quantum dots. Each of these technologies face some physical limitations that hinder the realization of the ideal entangled single photon source whose photons must be pure, indistinguishable, perfectly entangled and bright [1], [2].

Here, we focus on III-V semiconductor quantum dots which do allow for the generation of entangled photon pairs in polarization space. Unfortunately, they are not maximally entangled. As explained in the previous chapter, this is due to the inner asymmetry of the exciton trapping potential [3]. When the carriers move in a potential that breaks the inversion asymmetry, spin-orbit interaction removes the spin degeneracy even without the presence of an external magnetic field. The consequent splitting of the exciton state consists of several tens of μev. Even though Qdots structure engineering has minimized the fine-structure splitting and improved the degree of entanglement, the complete erasure of the fine-structure splitting contribution to the quantum state dephasing still remains a tough technological challenge. To date post-growth techniques [4–6] based on external strain field, magnetic and electric fields have been developed, but unfortunately these techniques usually act on the whole sample and do not readily compensate each and any of the Qdots present.

Even in case of successful tailoring of strain engineering of a single Qdot device as in [7], it remains a challenge to apply it to photonic nanostructures like Qdots embedded in nanowires [8] and micropillar cavities [9]. Efficient transfer of strain tuning is indeed very difficult since the strain field in such nanostructures cannot be easily transferred. Therefore, a universal fine-structure splitting compensation technique seems a practical alternative to still consider Qdots as good candidates for the realization of a "quantum network".

Here, we investigate a fine-structure compensation scheme based on optical frequency shifters (OFS). These need to comply with several stringent requirements: they must show near-to-one carrier suppression, they need to have high conversion efficiency into the desired sideband, and they must avoid any spurious sideband generation.

One possible way to achieve frequency shifting is by acousto-optic modulation (AOM). It is generally used for MHz range shifts and its tuning range is only a small fraction of its center frequency. AOM can also provide GHz shifts but this increased bandwidth comes at the cost of lower diffraction efficiency.

Broadband state-of-the-art electro-optic phase modulators (EOMs) avoid many of the bandwidth and tuning range limitations given by AOMs [10]. EOM-based OFS make use of non linear anisotropic crystals. These devices exploit the so-called linear electro-optic effect also known as Pockels effect. When an electric field is applied to the media, a variation in refractive index occurs along the crystal axes. This change has an impact on the velocity of the polarized light components travelling inside the crystal. The Pockels effect can then be used to build electrically controllable optical devices such as phase modulators and wave retarders. The former is used to deterministically shift the phase

of the wave packet and the latter to change polarization properties of light. As for wave retarders, Qin et al. demonstrated a frequency-shifting device emulating a rotating half-wave plate up to 2 GHz with sideband suppression greater than 20 dB [11]. This scheme can be used to produce a fully entangled Bell state as anticipated by Fognini et al. [12].

In the present work, we opted for the phase modulator approach since these EOMs devices are readily available commercially and according to our simulations can deliver above 90% conversion efficiency at 1.5 GHz modulation frequency even if driven with standard RF generation equipment.

4.2. INTRODUCTION

The degree of entanglement from a Qdot light source can be represented in many ways, like fidelity, concurrence or entropy. As discussed in chapter 2, we find concurrence to be the most useful for this application since, as an entanglement metric for a given state, it has the advantage to be independent of a reference state. Its values range from 0.5, if the state is separable, to 1 for a maximal entangled state. Let's recall fig. 2.10:

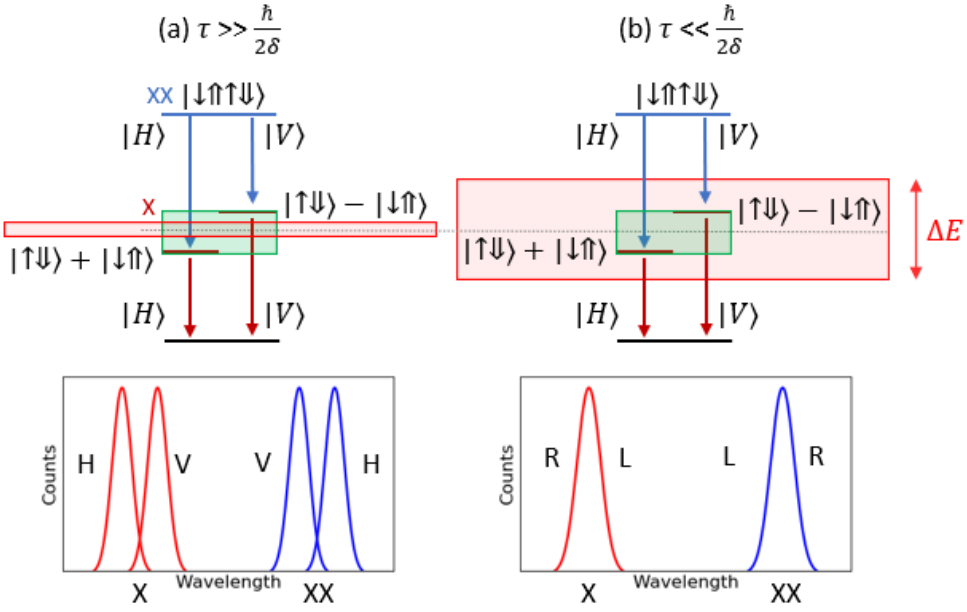

Figure 4.1: (a) The detector time resolution τ is lower than the characteristic time precession constant of the quantum state. Low uncertainty in energy ΔE (red box) is predicted with a slow detection and the exciton energy levels, split by the fine-structure splitting δ (green box), can be resolved. This results in a reduction of entangled correlations. (b) The detector system has a very high time resolution $\tau << \hbar/2\delta$, then the two electron-hole recombination processes become totally indistinguishable and the emitted photons are fully entangled in polarization space. With a fast detection, the uncertainty in energy becomes much higher, and the two non-degenerate states cannot be anymore resolved, pushing the Concurrence towards higher values.

We have seen that Concurrence depends to a high extent on two factors: the fine-structure splitting and the finite detection time resolution, once demonstrated that the fluctuating fields due to the nuclei spin are a negligible source of state dephasing. In fact, by exploiting the energy-time uncertainty, a high degree of entanglement was measured with a detection system of high temporal resolution showing that low jitter does indeed reduce the effect of the Qdot FSS bringing the concurrence value close to one [12].

Nonetheless, the Holy Grail for many applications is to erase completely this effect and eventually get rid of the time-evolving state:

$$|\Psi(t,\delta)\rangle = \frac{1}{\sqrt{2}}\left(|HH\rangle + e^{-i\frac{\delta}{\hbar}t}|VV\rangle\right), \tag{4.1}$$

and achieve:

$$|\Psi(t,\delta)\rangle = \frac{1}{\sqrt{2}}\left(|HH\rangle + |VV\rangle\right). \tag{4.2}$$

As proposed by Wang et al. [13], time-dependent phase difference of the two polarization modes can be removed by applying a linear voltage ramp to an electro-optic modulator (EOM). On one hand this approach faces that problem that an infinitely-long linear voltage ramp is impossible to generate. On the other, it underlies one big limitation: it requires expensive broadband RF equipment acting at time scales of nanoseconds down to hundreds of picoseconds. This speeds are dictated by the fine-structure splitting which lies typically in the hundreds of MHz until the lower GHz range. The need for an infinitely-long linear voltage ramp is overcome by replacing it with a sawtooth signal which has a finite duration by definition. Nevertheless, the speed requirement sets the need for fast RF electronics operating at GHz range. There are devices that can accomplish this task but besides being very expensive, they are anyway impacted by the limited bandwidth that does not allow for the generation of infinite harmonics. Bandwidth limitation in signal generation hinders the approach proposed by Wang due to the difficult task of delivering a high quality sawtooth at the desired speed.

We see below a comparison that motivates our statements by simulating the behavior of a near-to-perfect waveform generator and one that suffers from bandwidth limitation. A sawtooth signal $V_s(t)$ can be represented in time domain using a Fourier series of infinite harmonics:

$$V_S(t) = \frac{V}{2} - \frac{V}{\pi}\sum_{n=1}^{\infty}(-1)^n\frac{\sin(n\omega_f t)}{n}, \tag{4.3}$$

with ω_f being the fundamental frequency.

Fig. 4.2 shows an almost perfect sawtooth ramp generated by the addition of 200 harmonics whereas Fig. 4.3 shows a ramp generated by only 4 harmonics. In the second case we see from the Fast Fourier Transform (FFT) that the imperfect generator cuts the spectral components at 2 GHz and the output wave shows oscillations. These oscillations, in a optical phase modulation experiment, cause the onset of undesired sidebands during frequency translation.

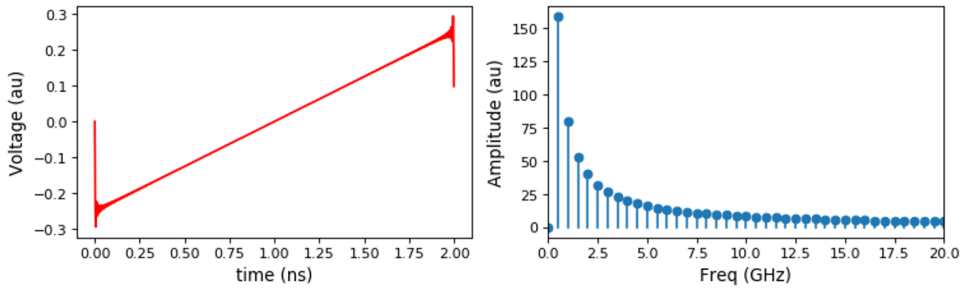

Figure 4.2: **(Left)** 500 MHz sawtooth wave composed by 200 harmonics in plotted time domain. **(Right)** Spectral components of the sawtooths after Fast Fourier Transform.

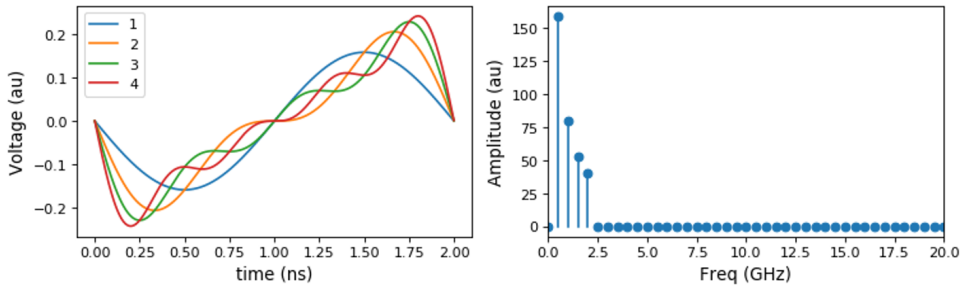

Figure 4.3: **(Left)** 500 MHz sawtooth wave composed by 4 harmonics in plotted time domain. **(Right)** Spectral components of the sawtooths after Fast Fourier Transform.

Nonetheless, off-the-shelf telecommunication equipment such as affordable arbitrary waveform generators still represent a workable solution. With high-speed digital-to-analog converters and Field-Programmable Gate Array (FPGA) processing, it becomes possible to generate the necessary signals in an affordable manner. The addition of electronic signals synchronization technology gives the chance to further quench the issue of bandwidth limitation. We claim that this technology provides the means to get entangled photons from Qdots at low cost while reducing the complexity of fabricating nearly-to-zero fine-structure splitting single photon sources.

In this chapter we will first explain why frequency translation can provide entangled photons. Secondly, we will discuss current arbitrary waveform generation technology along with the modern tools to achieve signals synchronization. Then, we will present the results of some simulations pointing out that signals synchronization is indeed beneficial for frequency translation. Finally we will show results of phase modulation experiments on a laser source emitting at 1550 nm.

4.3. FREQUENCY SHIFT OPERATOR FOR FSS COMPENSATION

The two-photon state decay provided in eq. 4.1 can be rewritten by stating explicitly the dependency on the cascaded photons' frequencies. Fig.4.4 (a) shows the quantum state described in the composite space of polarization and frequency:

$$|\Psi(t,\delta)\rangle = \frac{1}{\sqrt{2}}\left(|H_1H_2;\omega_{H1}\omega_{H2}\rangle + |V_1V_2;\omega_{V1}\omega_{V2}\rangle\right), \tag{4.4}$$

where H and V stand for the horizontal and vertical polarization, ω is the photon frequency for the first and second cascaded photon that are denoted with subscript 1 and 2. In order to retrieve a maximally entangled state, we want to apply an unitary operator U which has the capability to separate polarization and frequency space such that:

$$U|\Psi(t,\delta)\rangle = |\Psi(t)\rangle = \frac{1}{\sqrt{2}}\left(|H_1H_2\rangle + |V_1V_2\rangle\right) \otimes |\omega_{H1}\omega_{H2}\rangle\,. \tag{4.5}$$

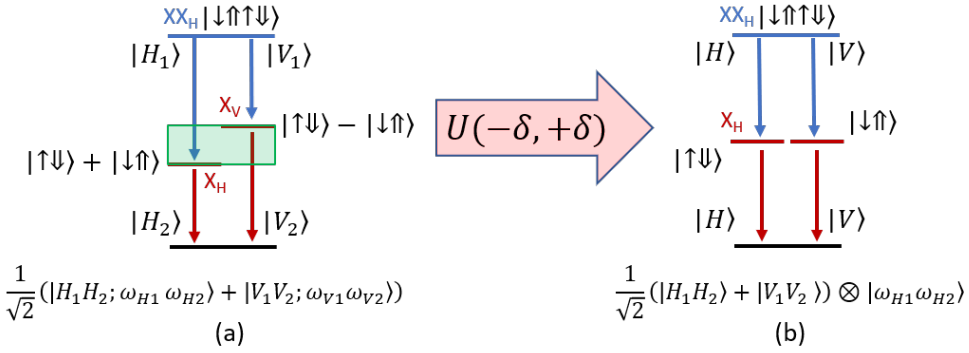

Figure 4.4: Sketch of the two-photon decay path before (a) and after (b) the application of the unitary frequency shift operator U with δ being the FSS depicted here as a green box. U splits the composite space of polarization and frequency by counteracting the precession given by the phase term in eq. 4.1. In (b) the exciton levels for both decay paths are degenerate and the state is described as the tensor product of the individual spaces.

The operator U has to act as a polarization-dependent frequency shift operator on one single polarization axis. For each cascaded photon, U results in:

$$U(\Delta_1,\Delta_2)\,|H_1H_2;\omega_{H1}\omega_{H2}\rangle = |H_1H_2;\omega_{H1}\omega_{H2}\rangle\,, \tag{4.6}$$

and

$$U(\Delta_1,\Delta_2)\,|V_1V_2;\omega_{V1}\omega_{V2}\rangle = |V_1V_2;\omega_{V1}+\Delta_1,\omega_{V2}-\Delta_2\rangle\,, \tag{4.7}$$

with Δ_1 and Δ_2 being the frequency shift on each photon respectively. Given 4.7 and 4.6, polarization and frequency space separation can be easily retrieved by fulfilling the following requirements:

$$\begin{aligned} \omega_{H1} &= \omega_{V1} + \Delta_1, \\ \omega_{H2} &= \omega_{V2} - \Delta_2. \end{aligned} \tag{4.8}$$

In conclusion, we have demonstrated the theoretical framework to achieve unity photon entanglement by applying to the quantum state the frequency shift operator U with a magnitude equal to the fine-structure splitting δ and opposite sign for each photon such that $U(-\Delta_1, +\Delta_2) = U(-\delta, +\delta)$. In such a way the effect of the fine-structure splitting can be completely compensated.

4.3.1. SETUP

In fig. 4.5 we propose a setup to achieve fine-structure splitting compensation. One question arises now: how to physically construct a frequency shift operator U?

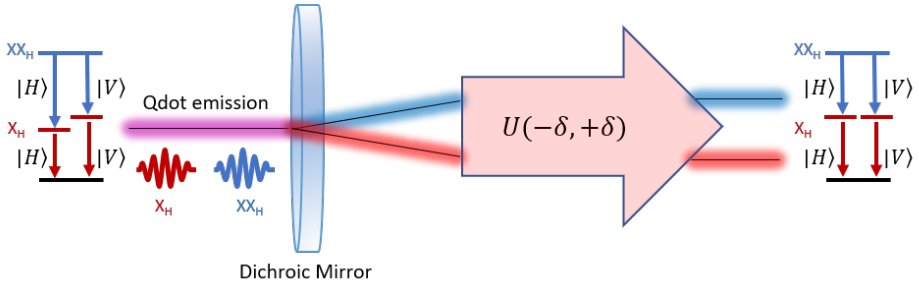

Figure 4.5: Sketch of the theoretical setup for FSS compensation. After the Qdot is excited by a pulsed laser, its emission is split at the dichroic mirror into the exciton (X) and biexciton (XX) components. The frequency shift operator U will compensate for the state precession thus getting rid of the time evolving state depicted in eq. 4.1. The exciton level for both decays will stay degenerate at all times.

As reported by Wang [13], spatial phase modulation is equivalent to performing an unitary phase transformation. Phase modulation changes the compensating phase at a fixed point in space by linearly varying the voltage applied to an electro-optic modulator provided that the phase shift is proportional to the scanning voltage. This applies to Pockels cells that can accomplish this task by changing the frequency of each cascaded photon by acting on its phase:

$$\phi(t) = \alpha V(t), \tag{4.9}$$

where α is the phase sensitivity of the Pockels cell. In light of the requirements derived in 4.8 we get that:

$$\phi(t) = \frac{\delta t}{\hbar} = \alpha V(t), \tag{4.10}$$

which leads finally to:

$$\frac{dV(t)}{dt} = \frac{\delta}{\hbar\alpha}. \tag{4.11}$$

This last equation demonstrates that to satisfy the fine-structure splitting compensation conditions we just need to apply a linear voltage. In the next section, we will discuss how to construct this unity operator in an experimentally implementable way.

4.3.2. CONSTRUCTION OF THE UNITARY FREQUENCY SHIFT OPERATOR

Until now we have discussed on how linear phase shifting of an optical signal allows its energy translation:

$$Ae^{-i\omega t+\phi(t)} = Ae^{-i\omega t+imt}, \tag{4.12}$$

such that:

$$\Delta\omega = -m. \tag{4.13}$$

One approach that allows for energy translation of optical pulses is phase modulation exploiting the approximate linear regions of single tone RF waves that are then fed to a $LiNbO_3$ modulator [14]. In this case, frequency translation is however limited to short optical pulses as sketched in fig. 4.6(b). In fact, as the frequency of single tone wave increases, its linear portion becomes steeper yet shorter in time. If the optical pulse is longer than this linear part, we witness the rise of spurious sideband in the output modulated signal. Therefore, this enforces a trade-off between the magnitude of the shift and the duration of the optical pulses to be shifted.

Recalling that the Qdot emission lifetime can have duration of several hundreds of picosecond, we can conclude that a better-off method for frequency translation is indeed sawtooth phase modulation. Here, there is theoretically no contribution from sine wave modulation with no concern on the timing arrival of the photon since this will always experience linear modulation as shown in fig. 4.6(a). Ideally, sawtooth phase modulation can produce frequency translation of either continuous-wave or pulsed optical signals but in reality this approach faces some limitations (see sec. 4.3.4).

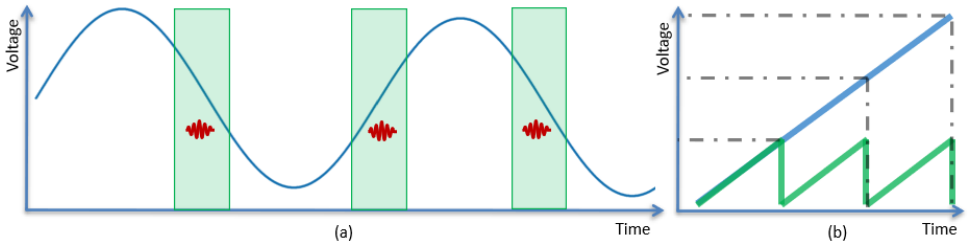

Figure 4.6: (a) Phase profile in time domain used for frequency translation of short optical pulses. The pulses are synchronized with the linear portion (highlighted in green) of the sine RF wave in order to avoid spurious sideband generation. (b) Phase profile in time domain used for serrodyne modulation. Frequency translation of continuous optical signals and longer pulses is achievable in this configuration. This sketch shows in a simple manner how to circumvent the fundamental issue of creating an infinitely long linear RF signal. The linear phase profile is composed by the sequence of shorter ramps.

Let's consider the case where a time-dependant phase shift is added to the optical signal. The wave-packet will exit the EOM with electric field:

$$E_{PM}(t) = E_0 e^{i\omega_c t + \beta\phi(t)} = E_0 e^{i\omega_c t} e^{i\beta\phi(t)}, \tag{4.14}$$

where ω_c is the carrier frequency and $\phi(t)$ is the linear additional phase. The frequency shift of the original signal can then be investigated by Fourier Transform:

$$\mathscr{F}(E_{PM}(t)) = \mathscr{F}\left(E_0 e^{i\omega_c t} e^{i\phi(t)}\right) = E_0 \mathscr{F}\left(e^{i\omega_c t}\right) * \mathscr{F}\left(e^{i\phi(t)}\right). \tag{4.15}$$

In the simplest case, we can replace $\phi(t) = \omega_m t$. We see directly that such a linear phase ramp shifts the frequency by $\pm\omega_m$ up or down depending if a negative or positive slope is selected. We can now derive $\phi(t)$ from eq. (4.11) which links the RF voltage to the phase change generated by the EOM. By replacing the fine-structure splitting δ with the modulation frequency ω_m, and adding the modulation index β that accounts for the steepness of the phase profile, the solution of eq. (4.15) can be found easily.

$$\mathscr{F}(E_{PM}(t)) = E_0 \mathscr{F}\left(e^{i\omega_c t}\right) * \mathscr{F}\left(e^{i\beta\frac{dV(t)}{dt}}\right) = E_0 \mathscr{F}\left(e^{i\omega_c t}\right) * \mathscr{F}\left(e^{\pm i\beta\omega_m t}\right). \tag{4.16}$$

The modulation depth β is strictly related to V_π that indicates the voltage needed to achieve a phase shift of π. To conclude:

$$\begin{aligned}\mathscr{F}(E_{PM}(t)) &= E_0 \delta(\omega - \omega_c) * \delta(\omega \pm \beta\omega_m) \\ &= \delta(\omega - \omega_c \pm \beta\omega_m).\end{aligned} \tag{4.17}$$

with δ being the Dirac function. According to eq.(4.17) the whole optical power in the carrier band will be shifted by $\omega = \omega_c \pm \beta\omega_m$. To ensure phase continuity, the peak-to-peak amplitude of the modulating sawtooth must be an integer multiple of $2V_\pi$. Once this condition is met, β is chosen to be an integer number. As a result, phase modulation with a sawtooth with fundamental frequency ω_m and peak-to-peak amplitude $2\beta V_\pi$, produces a frequency shift of $\beta\omega_m$. An upward or downward shift depends on the sign of slope.

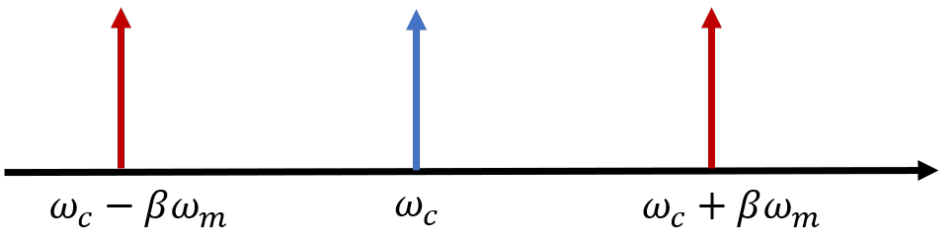

Figure 4.7: Simple sketch of frequency translation of monochromatic light. ω_c is the carrier frequency (blue Dirac pulse). This can be shifted up or down by an amount equal $\pm\omega_m$ (red Dirac pulses) according to the sawtooth slope's sign.

We can finally claim that the frequency shift operator U can be physically constructed through sawtooth phase modulation. U, that was sketched in the theoretical apparatus in 4.5 as an unknown physical entity, can be replaced in fig. 4.8 by the action of two phase modulators performing an upward or downward shift on the X and XX emissions.

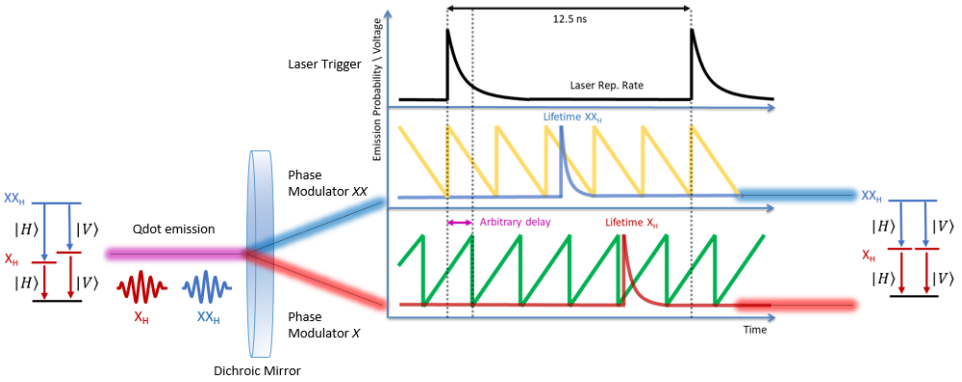

Figure 4.8: Sketch of the optical setup for FSS compensation. After the Qdot is excited by a pulsed laser, whose trigger is represented by a black trace with 12.5 ns repetition rate, the emission is split at the dichroic mirror into its exciton (X) and biexciton (XX) components. The two Pockels cell (X and XX), synchronized with Qdot emission, will imprint a reverse linear phase modulation to both emission lines (green and yellow traces). Comparing the photon energy before and after phase modulation, it is expected that the two emission lines have the same energy at all times, thus getting rid of the time evolving state depicted in eq. 4.1.

4.3.3. PHASE MODULATOR TECHNOLOGY

$LiNbO_3$ electro-optical modulators exploit the Pockels effect, a linear change of the refractive index as a function of the applied voltage. This effect comes from the displacement of charges in the presence of an external electric field $\vec{E}_0$ which induces a macroscopic polarization inside the material. According to the Pockels effect, an incident beam polarized parallel to one of the crystal axis will experience a phase retardation proportional to the electric field applied across it.

$$\Delta\Phi_x = \frac{2\pi}{\lambda}\Delta n_x L, \tag{4.18}$$

with l and Δn_x being the length of the crystal and the change in refractive index during the transit time of light through the $LiNbO_3$ waveguide. $LiNbO_3$ is known to have crystal symmetry of $3m$ [15] such that with beam propagation along the x axis we find:

$$\Delta n_x = n_e - \frac{1}{2} n_e^3 r_{33} E_0, \tag{4.19}$$

where n_e denotes the extraordinary refractive index of the material and E_0 stands for the external electric field. The integrated $LiNbO_3$ optical modulator uses a X-cut Y-propagating waveguide in order to exploit r_{33}, the highest electro-optic coefficient (30.8 pm/V). Strongest electro-optic interaction happens when both the electric field and the optical polarization are parallel to the Z-axis. Here's a sketch of the device:

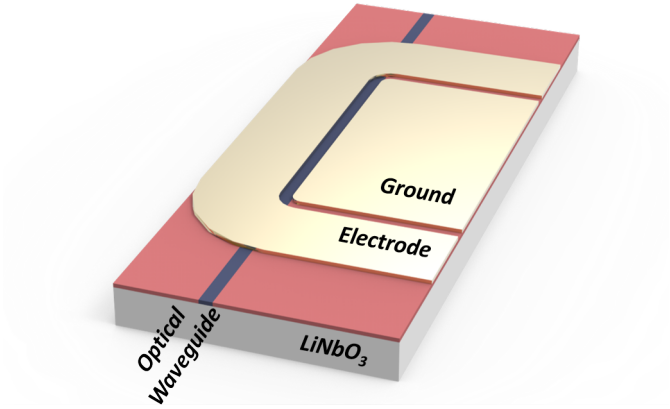

Figure 4.9: Sketch of integrated $LiNbO_3$ optical modulator in a X-cut substrate.

By substituting (4.19) into eq. (4.18) we find that:

$$\Delta\Phi_x = \frac{2\pi}{\lambda}\left[n_e - \frac{n_e^3 r_{33}\Gamma V}{2g}\right]L \approx \frac{\pi V}{\lambda g}\left[\Gamma n_e^3 r_{33}\right]L = \pi\frac{V}{V_\pi}, \tag{4.20}$$

with g being the gap between the coplanar electrodes driving the pockels cell and Γ the overlap coefficient between the optical mode and the applied electric field. V_π is the voltage that gives a phase retardation of π [16]:

$$V_\pi = \frac{\lambda g}{\Gamma n_e^3 r_{33} L}. \tag{4.21}$$

In this class of devices, known as travelling wave modulators, the phase velocities of both the optical and electrical modulation fields need to be equal to each other. As a result the optical wavefront will experience the same instantaneous electric field everywhere across the crystal, thus lifting concerns about phase retardation reduction due to the finite transit-time [15]. The Sumitomo T.PM1.5–40 phase modulator achieves this matching thanks to its transverse geometry.

4.3.4. EXPERIMENTAL CONSIDERATIONS

Although sawtooth modulation seems to be promising at compensating fine-structure splitting, it sets a few critical requirements concerning:

- the RF generation equipment,
- the amplification stage that feeds the signal into the EOM,
- and the EOM with an ideally linear optical response to the RF signal.

The main limitation when fulfilling the first requirement comes from the need of fast electronics with hundreds of picoseconds ramp duration and ideally zero reset time. Such equipment besides being very expensive, does anyway have an inner limited bandwidth.

Bandwidth limitation will eventually cut the contribution of the higher harmonics hindering the feasibility of reliable sawtooth generation and consequent modulation. In the next section, a description of an affordable arbitrary RF waveform generator is given. Such device has the additional capability to achieve phase locking to an external clock providing means to overcome the non-zero reset time and discard the edges of the ramp where the signal exhibits ringing behavior. Locking the sawtooth generation to the laser trigger clock will ensure that the photons experience mostly linear modulation. A detailed comparison of phase modulation with and without locking will be given to benchmark its utility.

4.4. ARBITRARY WAVEFORM GENERATION

Recent developments in RF engineering and digital signal processing enabled the realization of affordable Arbitrary Waveform Generators (AWG) into the several GHz range. Their primary purpose is in telecom applications. Great technological boost to AWGs has been given by higher performance digital-to-analog converters (DACs) thanks to the drastic increase in their output bandwidth, sampling rate and bit resolution.

AWGs working principle is depicted in fig. 4.10. The digital waveform is first loaded into the waveform memory. Then, the samples stored in memory are clocked at a fixed sampling rate by a FPGA and later converted by the DAC module. The DAC conversion rate is governed by a variable-frequency reference-clock VCO known as voltage controlled oscillator. The output sampling rate of the AWG is then determined by the reference clock's frequency, with a waveform sample converted to an output signal for every clock cycle. As a result, faster clock rates lead to faster readout of the samples stored in memory and faster generation of the RF signal.

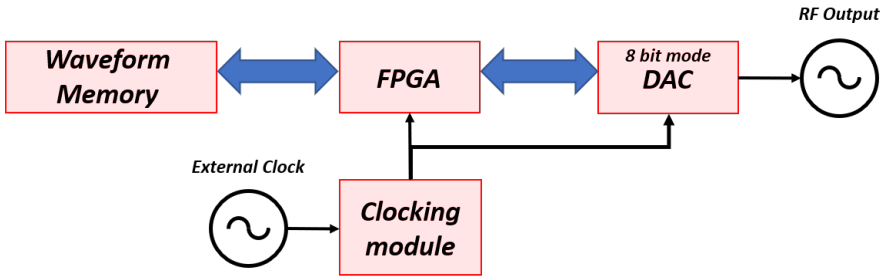

Figure 4.10: Block diagram of an AWG with DAC operating at 8-bits voltage level resolution.

As a proof of principle, we are using a DAC from Texas Instruments which can provide 9 Gsps at an affordable price. This features is very relevant for our application which requires the generation of high harmonics at the fastest possible conversion rate. On the other hand, the digital pattern generator is represented by the TSW14J56EVM. After receiving the digital waveform from the user, its FPGA module stores the data into the on-board DDR3 memory. The data from the memory is then read by the FPGA itself, converted to a serial format and finally sent to the DAC.

4.4.1. CLOCKING: LMK04828 WITH PHASE-LOCKED-LOOP TECHNOLOGY

The evaluation board is equipped with a time distribution chip (LMK04828) with a jitter cleaning device using dual Phase-Locked-Loop (PLL) technology. The PLL is a control system that generates an output signal whose phase is fixed to the phase of an input signal. Its electronic circuit is made by a variable frequency oscillator and a phase frequency detector (PFD) in a feedback loop. The oscillator generates a periodic signal and the PFD compares the phase of that signal with the one of the reference periodic signal. With its built-in charge pump, the PFD adjusts the oscillator frequency and locks the phases of the two independent signals.

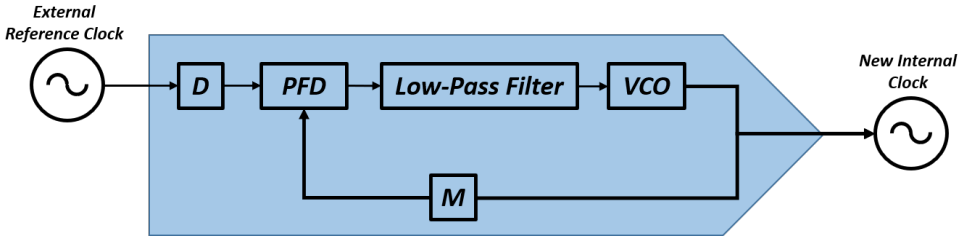

Figure 4.11: Schematic of Phase-Locked-Loop with D (divider), PFD (phase frequency detector), VCO (Voltage-controlled-oscillator) and M (multiplier).

In addition to synchronizing signals, the phase-locked loop tracks the input frequency and can synthesize new frequencies by mere multiplication and division from the original frequency through the divider *D* and multiplier *M* modules (fig. 4.11). In this way, fractional frequencies can be generated from the input signal.

In conclusion, this device realizes a fixed phase relationship between the external reference clock and the waveform generation output through the generation of a common clock (Clocking module at fig. 4.10) shared among all the building blocks of the AWG. Once this common clock is available, the LMK04828 feeds and binds all peripherals as shown in fig. 4.12 keeping a fixed phase relationship among them all.

4.4.2. NESTED 0-DELAY DUAL PLL WITH ON-BOARD VCXO CLOCK MODE

The LMK04828 is used here as a dual-loop jitter cleaner to "clean up" a "dirty" reference clock with good frequency accuracy but poor phase noise and to generate ultra-low jitter output clocks.

To do so, it makes use of a dual-loop architecture where two PLLs are cascaded in the so-called "nested zero delay dual-loop" configuration which routes the divided clock of PLL2 into the N-divider of PLL1 as shown in fig. 4.12. In this cascaded mode the LMK04828 establishes a deterministic phase relationship between the external coarse reference clock phase and clock output phase. Using the zero-delay mode, multiple LMK04828 can be cascaded to generate multiple output clocks, while maintaining fixed input-to-output phase throughout the whole chain of devices. This option is greatly relevant for our application given the necessity to synchronize the sawtooths signals output by two distinct AWGs driving their respective phase modulators where the coarse external clock is represented by the laser trigger.

In more details, a quartz-based voltage controlled oscillator (VCXO) oscillating at 122.88 MHz, with a tuning range of ±20 ppm, provides the reference clock to PLL2 that synthesizes the new high-frequency reference clock at 2.5 GHz. This is subsequently divided and fed to the DAC's internal PLL, the FPGA on the TSW14J56 pattern generator and back to PLL1. If the phases of the divided feedback clock and the pulsed laser trigger are comparable, PLL1 will slightly adjust the VCXO by means of the PFD output locking PLL2 to the external reference. As a result, the nested 0-delay dual loop mode guarantees that the laser trigger is phase locked to the AWG output samples by having the FPGA, DAC and laser synchronized with each other.

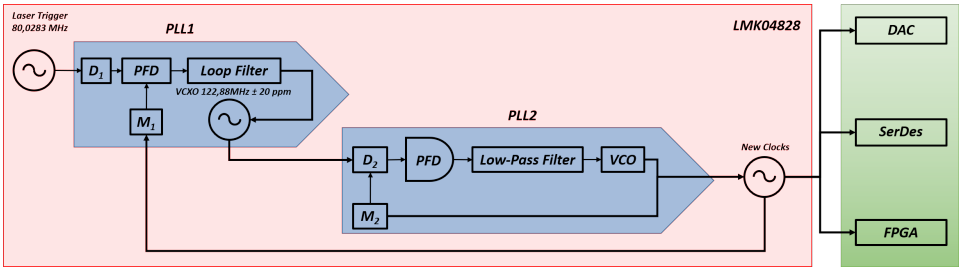

Figure 4.12: Sketch of the LMK04828 chain sequence operated in 0-delay nested loop configuration. PLL1 cleans the external clock whereas PLL2 synthesizes the new clocks that all share the same phase with the input clock. These clocks are fed to peripheral devices DAC and FPGA that are in turn phase-fixed to the laser trigger. All modules are synchronized.

We noted that the phase noise induced by the too noisy "dirty" clock has an impact on the clock alignment of both the internal DAC PLL and FPGA. The up-converted sampling clock rate will have its phase slightly off with respect to the external clock. "Dirty" clocks refer to clocks that are not perfectly single tone waves and in the case of the laser trigger, they resemble the shape of a distorted pulse. As a result, phase comparison in the PFD causes the rise of a leakage current that degrades the quality of the locking and consequently the quality of the common clock distributed to peripheral devices. Experimentally this is witnessed as a 2 ps/second drift on the output waveform with respect to the laser reference signal.

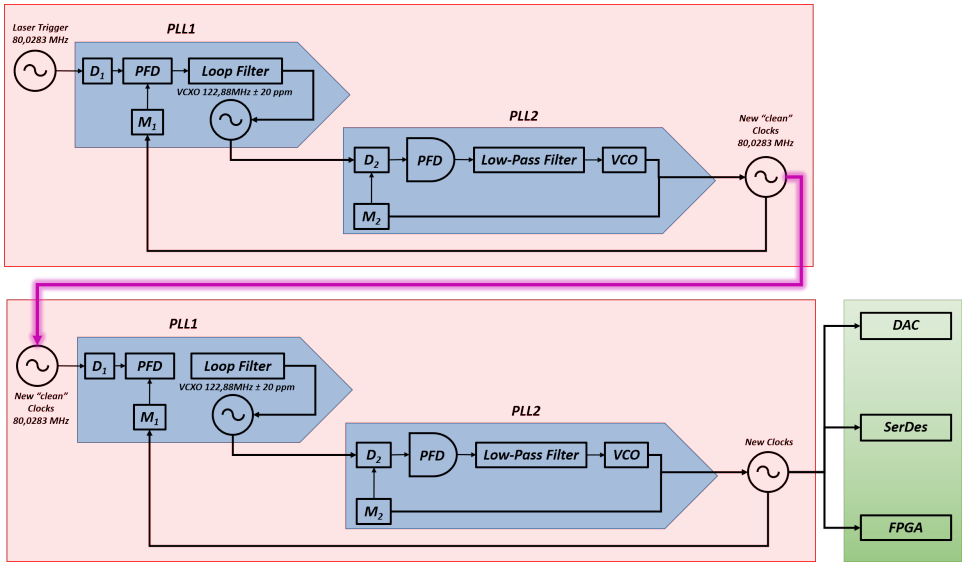

Figure 4.13: Double LMK04828 chain sequence operated in 0-delay nested loop configuration. The first LMK cleans the "dirty" laser trigger and generates a new "clean" clock (purple arrow) to be fed to the second evaluation board. The latter produces the clock for the peripheral devices. This solution fixes 2 ps/second drift.

To overcome this issue the use of a first stage LMK04828 ("Jitter cleaner PLL") is necessary. As shown in fig. 4.14, after the "Jitter cleaner PLL" is locked to the "dirty" clock, a new "clean" clock from PLL2 is synthesized with frequency equal to the original "dirty" clock with the former having a better phase noise figure compared to its parent one. The new cleaned-up clock will now drive the second stage LMK04828 which is the one in charge of the waveform generation.

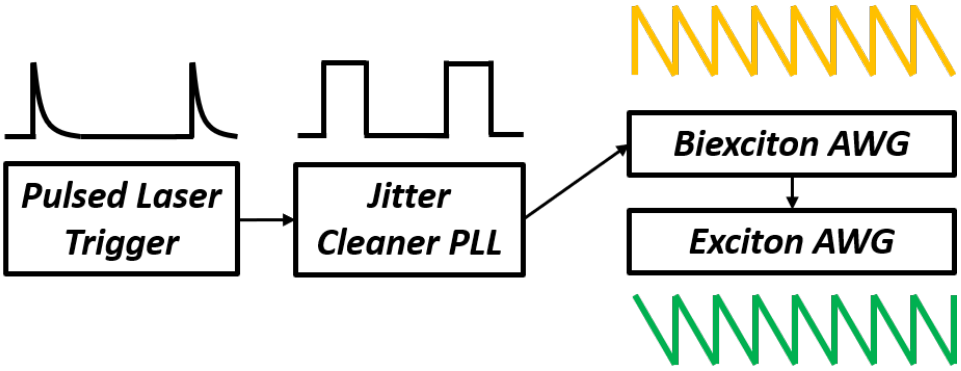

Figure 4.14: Sketch of RF chain from laser Sync signal to waveform generation.

By making use of this feature, the output waveform does not suffer from any drift. To prove the quality of the locking we measured the timing jitter between a 800 MHz sawtooth generated by the DAC and the PicoEmerald picosecond laser trigger. The synchronized traces are shown in fig. 4.15 with the sawtooths placed at exactly one laser cycle distance.

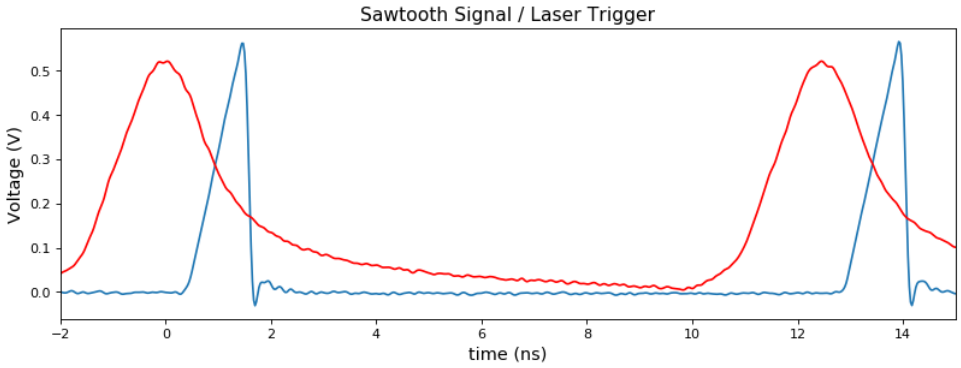

Figure 4.15: Traces of PicoEmerald laser trigger (red) and train of sawtooths (blue) used to perform jitter measurement in fig.4.16

Fig. 4.16 shows the histogram of the coincidences between the two RF signals along with the Gaussian fit. We can conclude that the locking accuracy is 38.7 ps. The fitted curve also suggests that the distribution does not fully resemble a Gaussian behavior.

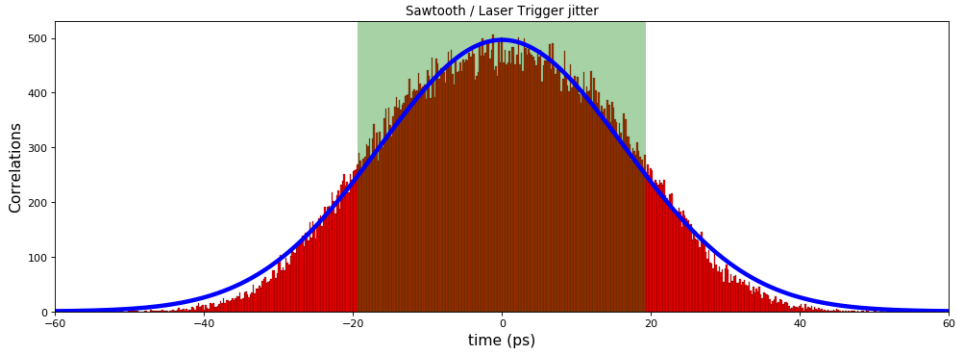

Figure 4.16: Measurement of locking accuracy between DAC output and PicoEmerald Laser 38.7 ps, highlighted in green. This value demonstrates the possibility to lock the quantum dot emission within the ramping of the time of the sawtooth.

An additional feature provided by the DAC38RF82EVM is the adjustable digital delay output. This feature closes the circle about the feasibility of matching the lifetime of the triggered Qdots emission with the sawtooth ramps. The output digital delay enables to fine adjust the output waveform samples position with respect to the external trigger with a resolution limited by the timing jitter. The core scheme of the experiment is shown in fig. 4.17(Left) with all its components whereas in (b) it is made clear that the goal is to synchronize the exciton X_H and biexciton XX_H emissions to the ramping signal.

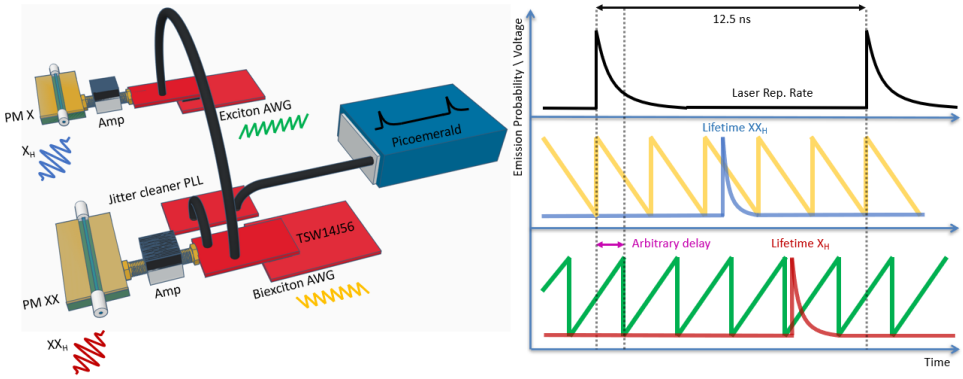

Figure 4.17: **(Left)** PicoEmerald laser trigger is fed to the jitter cleaner PLL that generates and distributes the core clock towards both AWGs driving the phase modulators (PM X and PM XX). Their task is to modulate the H component of the exciton X_H and biexciton XX_H electric field respectively. **(Right)** Description of signal locking: biexciton sawtooth signal (yellow) and exciton sawtooth signal (green), match the laser repetition rate by an exact integer multiple. The arbitrary delay (cyan) makes sure that the Qdot lifetime starts after the the sawtooth reset-time, improving the quality of the modulation.

4.4.3. HOW TO LOCK: A PRACTICAL GUIDE

The locking procedure starts by knowing the frequency bandwidth of the VCOs available in the LMK04828. Since the LMK04828 is not originally equipped with a VCO that can simultaneously deliver a DAC sampling rate close to 9 Gsps and oscillate an integer number of times within the pulsed laser cycle, we had to find a workaround.

Let's start with the **first requirement** which is finding the right settings to lock the DAC card to the LMK clock distribution. This must occur with the DAC clock frequency (sampling rate) oscillating as close to 9 GHz as possible. With the current VCOs installed we can reach a value of 8820.90037 MHz constrained by the reference laser clock frequency oscillating at 80.02833 MHz. The 8820.90037 MHz DAC sampling rate yields a combination for the DAC divider D_{DAC} and multiplier M_{DAC} equal to 9 and 992. With these values, the DAC clock frequency must be synthesized by the VCO in PLL2 oscillating at 2480.88 MHz. According to the specifications provided by the on-board VCO this task can be accomplished.

Having found the locking settings for the DAC card, the **second requirement** is to find the proper combination of LMK divider D_{PLL2} and multiplier M_{PLL2} in PLL2 that will generate the core clock at 2480.88 MHz starting from the base quartz clock at 122.88 MHz. This is done by using a script to calculate the best match with the least rest. Many combinations for D_{PLL2} and M_{PLL2} can be found, but to ensure locking the goal is to find the couple that minimizes the difference to the desired frequency. The script yields D_{PLL2} = 1024 and M_{PLL2} = 20674 and the rest is theoretically 0. With these values can foresee a very reliable locking.

Now, in order to close the locking loop we must feed a divided version of the core clock to PLL1. By choosing a final divider of 31 we can assure that the 2480.88 MHz will match the input laser reference signal of 80.02833 MHz. PLL1 on its hand does not multiply or divide the input reference signal because the dividing and multiplying procedure is already handled by PLL2.

There is only one last obstacle, namely that the laser frequency does not fit an integer amount of times within the DAC sampling clock. In fact, the exact fraction is $\bar{f}$ = 8820.90037 MHz / 80.02833 MHz = 110.222222. This can be solved in two ways: either replacing the current VCO with one that makes sure that the division yields an integer number, or to find the exact length of the digital frame of the waveform that counteracts this mismatch. Constrained by the fact that the digital frame can be only a multiple of 256 entries and that the maximum number of entries is 256000, we look for the number that multiplied by $\bar{f}$ yields the smallest rest to the sampling rate. This number is 1738, so that, to achieve locking, the digital frame needs to be 256*1738 = 222464 entries long.

With all these steps we can reach phase locking among all devices.

4.5. RESULTS AND DISCUSSION

4.5.1. SIMULATIONS

To further prove the rationale of our research, we show here the comparison of two simulations investigating the optical frequency translation for no-locking and locking configurations. To evaluate the purity of single sideband shifting, the optical field is simulated to be modulated with sawtooths oscillating at six different frequencies. To take into account the limited bandwidth of the electronics, the signal is filtered with a low-pass Butterworth filter with cut-off frequency at 4.5 GHz to mimic the AWG used. The pristine signal (blue-dashed line) and its filtered version (continuous-red line) are shown in fig. 4.18. As we approach higher frequencies, for instance 2.5 and 3.0 GHz, the impact of the system's limited bandwidth is more prominent and the sawtooth resembles completely a sine wave because the higher harmonics cannot be generated if the base frequency is already too high.

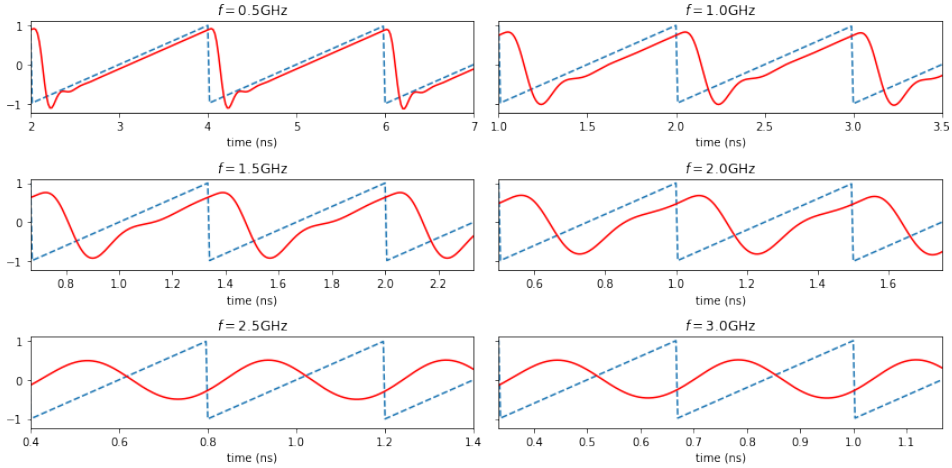

Figure 4.18: Comparison between pristine sawtooth (blue-dashed line) and filtered counterpart (continuous red-line) oscillating at 0.5, 1.5, 2.0 2.5, 3.0 GHz.

Assuming that the modulated light is monochromatic, the Qdot emission is represented by a δ function and eq. 4.16 reduces to the second Fourier term.

$$\mathscr{F}(E_{PM}(t)) = E_0 \mathscr{F}\left(e^{i\omega_c t}\right) * \mathscr{F}\left(e^{\pm i\beta\omega_m t}\right) = E_0 \mathscr{F}\left(e^{\pm i\beta\omega_m t}\right) \tag{4.22}$$

In case of locking the emission comes with a deterministic delay with respect to the start of the ramp signal. In non-locking the δ function is randomly placed in time. The simulation does then investigate the modulation term giving a phase shift equal to π.

Fig. 4.19 shows the FFT applied to the filtered signal in non-locking and locking configuration. For the locking case, the FFT is computed with the optical field synchronised to the part of the ramp where the modulation appears mostly linear: for each sawtooth, the optical field is turned on for a time interval equal to half of the ramp duration, namely

with a 50% duty cycle. In both cases we witness the rise of undesired sidebands, but it is apparent that the spurious spectral components generated in the locking configuration are roughly one order of magnitude lower if compared to the non-locking one.

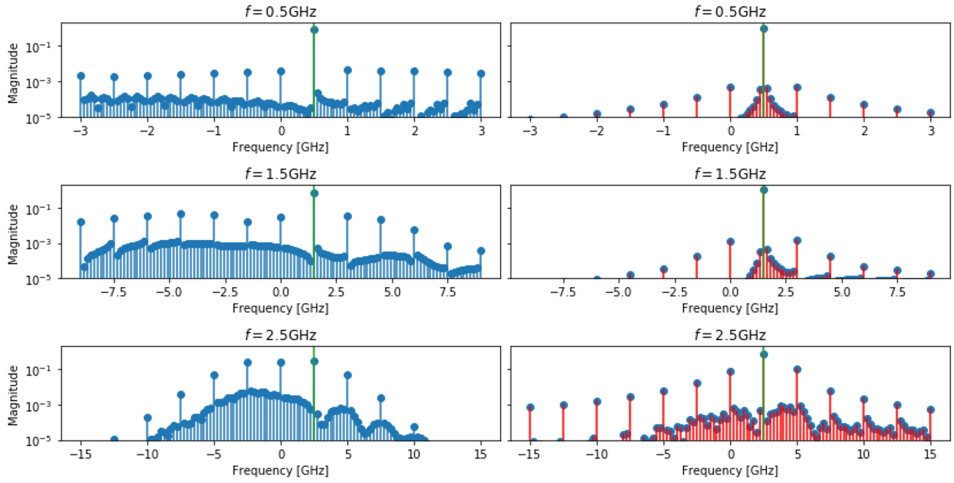

Figure 4.19: **(Left)** FFT spectra computed for non-locking and **(Right)** locking configuration. The green vertical lines show the center frequencies of the first sideband at a distance equal to sawtooth oscillation frequency.

In fig. 4.20 we compare the amount of optical power shifted into the sideband adjacent to the carrier for the locking and no-locking methods.

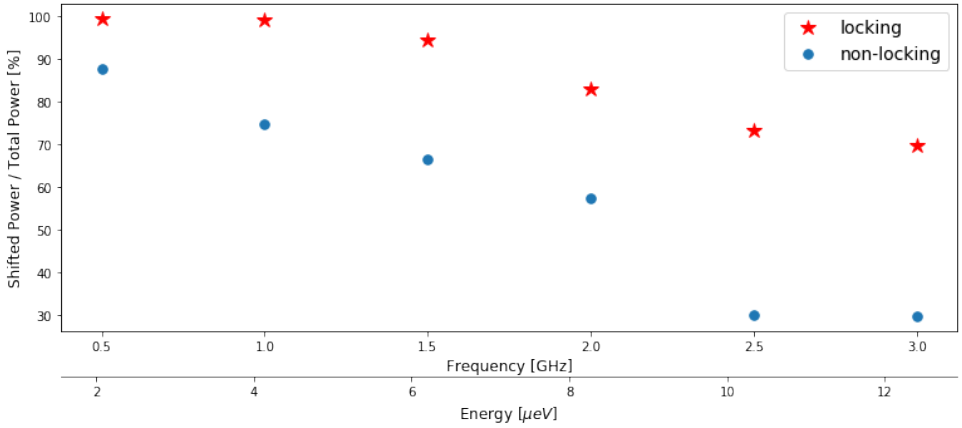

Figure 4.20: Comparison of optical power percentage shifted into the first sideband for the sawtooths oscillating at 0.5, 1.5, 2.5 GHz. Locking configuration predicts a roll-off between 2.0 and 2.5 GHz sawtooth frequency for an optical field with 50% duty cycle.

It is interesting to note that around 2.0 GHz there is a sudden drop in optical power transfer for the non-locking configuration. That is once again because of bandwidth lim-

itation which reduces the number of harmonics to one. What we witness after 2.0 GHz is indeed almost pure sine wave modulation. It is also remarkable that using the locking technique we can greatly suppress this limitation. The amount of power transferred into the desired band may in fact improve approximately from 10% to 40%.

To conclude, we discussed how continuous-wave signals can be ideally modulated by sawtooth modulation with single sideband generation. Nevertheless, RF modulating signals are not perfectly linear and face limitations due to the finite bandwidth of the electronic equipment. An alternative approach is though worth investigating: the locking technique that fixes the Qdot emission to the portion of the sawtooth that is mostly linear. In the next section, we will present measured spectra of modulated light for the non-locking case.

4.5.2. MEASUREMENTS

We start by showing the profile of the sawtooth oscillating at 500 MHz and 1 GHz along with their Fourier spectra generated with the AWG card and measured with a 4 GHz-bandwidth 40-Gsps oscilloscope. These profiles were used for modulation. It is evident from the comparison of the two waveforms that the 500 MHz sawtooth shows a better ramp profile given the higher number of harmonics that compose the signal. Unfortunately, we could not test the quality of the 500 MHz sawtooth because our amplifier did not allow to reach 2π shift, namely 1 GHz. Frequency translation of 1 GHz was in fact the bare minimum to appreciate an enough consistent shift with the Fabry-Perot tunable filter at our disposal.

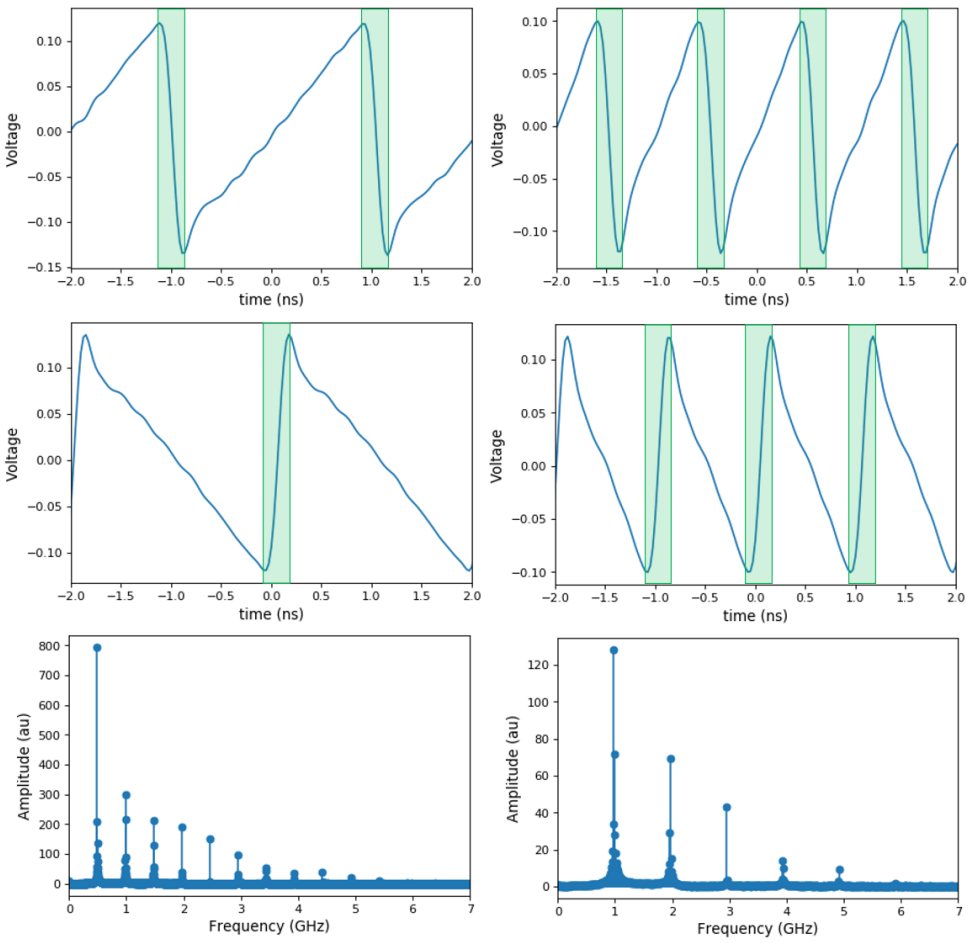

Figure 4.21: Measured sawtooths generated with the AWG card. **(Left Column)** Ascending and descending 500 MHz sawtooth. **(Right Column)** Ascending and descending 1 GHz sawtooth. Profiles in frequency space are shown at the bottom. Green shaded areas highlight time interval where modulation is harmed by the non-zero reset time of the AWG.

Once having tested the electrical waveforms, we fed them into the amplifier coupled to the phase modulator. The optical measurements were carried out using a continuous-wave laser emitting at 1550 nm that was polarized on the axis of the modulator. A Fabry-Perot tunable filter with free spectral range of 497.01 GHz and 0.476 GHz resolution was coupled to a fast InGaAs photodiode. Given the bandwidth of the Fabry-Perot tunable filter, a measurable shift was clearly visible for modulation frequencies above 500 MHz that is roughly the linewidth of the laser emission. Spectra were taken for increasing values of gain amplification that directly translates into deeper modulation.

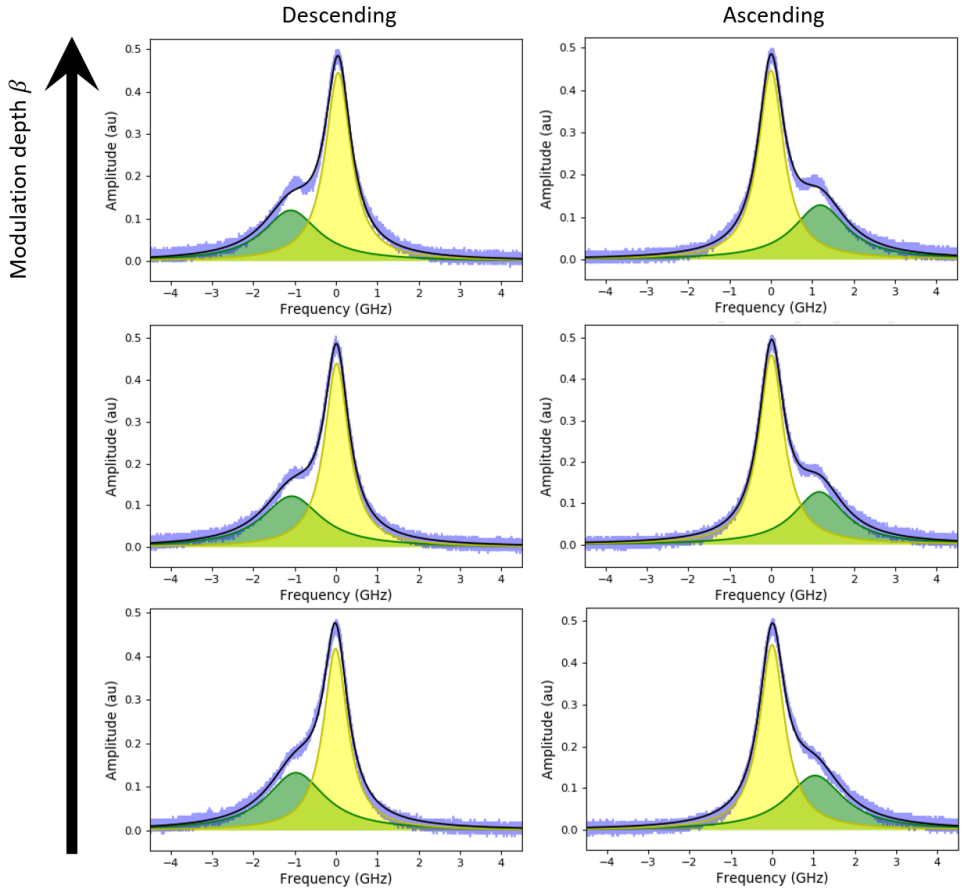

Figure 4.22: **(Left Column)** Spectra of the laser modulated with an ascending sawtooth for increasing value of modulation depths β. **(Right Column)** Spectra of the laser modulated with a descending sawtooth. Double Lorentzian peak fitting (Black line) shows a Lorentzian around the carrier frequency (yellow peak) and another roughly ± 1 GHz apart (green peak).

From the measurements we witness the rise of most likely two peaks that we cannot separate completely. Hence, we fitted the data with a double Lorentzian peak.

To explain this behavior we ran a simulation similar to the one explained in the previous section where we kept the oscillation frequency of the sawtooth fixed at 1.0 GHz and

varied the modulation depth β by steps of 0.1 from 0.1 to 1. What we experienced was the onset of sine-wave-like phase modulation for which the modulation index tunes the amount of power from the carrier to the sideband without suppressing completely the baseband. Fig. 4.23 shows indeed the power carried by the baseband and sideband as the modulation is increased. From this graph we can infer that the applied modulation has its index lying at about 0.3.

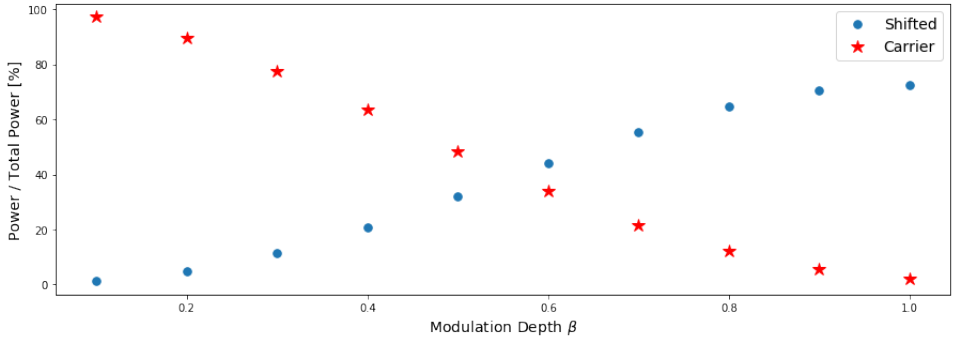

Figure 4.23: Power held by the carrier and the sideband at 1 GHz as modulation index increases.

For comparison, we also performed a measurement with pure sine-wave modulation. Results are shown below:

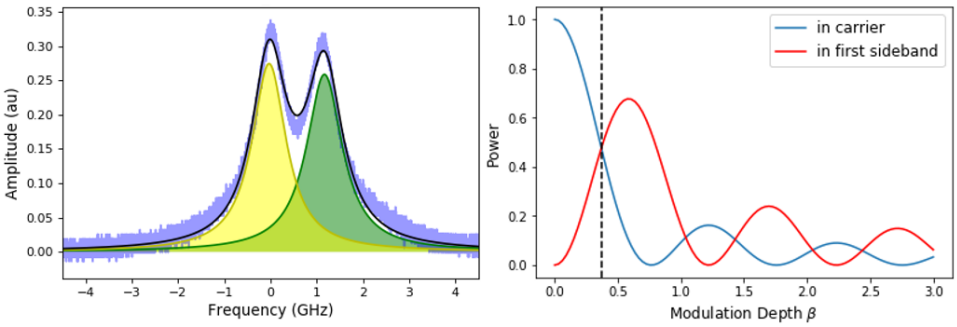

Figure 4.24: **(Left)** Spectra of the laser modulated with an pure sine oscillating at 1 GHz. we witness the rise of two peaks. **(Right)** Sideband power transfer following Jacobi-Anger expansion. Same amount of power held in both bands occurs for a modulation index equal to 0.37 which is sketched with a dashed vertical line.

Expanding the generated field from a signal whose phase is modulated with a pure sine-wave, the Jacobi-Anger expansion foresees the rise of multiple sidebands. This is simulated in fig. 4.24(right) which depicts the power transferred from the carrier into the first sideband as the modulation depth increases. In fig. 4.24(left) we see that both measured peaks carry similar power indicating that the modulation index is around 0.4. This confirms the value of the modulation depth applied for the sawtooth.

Although our equipment did not let us reach higher modulation depth than roughly 0.4π, the results point out that the undesired modulation shown in fig. 4.21 turn fre-

quency translation into sine-wave like phase modulation and suggests that locking the signal to the linear part of sawtooth may rule out the onset of bad modulation intended as the finite duration for the sawtooth to drop to zero.

The last comment concerns the locking technique which we could not test unfortunately. This is because the Fabry-Perot spectra of a short laser pulse will cover the whole free spectral range of the instrument and the task of selecting a sharp line from this broadband emission is very challenging. One could eventually measure the modulated signal with a very fine grating and a camera after having stretched the laser pulse with a pulse shaper to the maximum provided by the instrumentation. Then, a proper Gaussian fit of the optical profile could quantify the quality of the modulation. Unfortunately, we faced a breakdown of the camera in our laboratory that ruled out this possibility.

4.6. CONCLUSION

Frequency translation of single photons while preserving their quantum characteristics is an important technology for flexible networking of photonic quantum communication systems. Here, we have investigated an affordable scheme to change the energy of the photons with a commercial phase modulator. We have pointed out the technological limitations and provided a possible solution to overcome undesired phase modulation. We have seen that by changing the radio-frequency signal that drives the modulator, the optical power can be translated into other frequencies. We claim that upgrading the RF amplification stage and synchronizing the light emission to the "sweet spot" where the sawtooth has almost perfect linearity will be beneficial to shift all the photons in the desired band. However, due to broken equipment, it could not be verified within this project. We can anyway foresee to erase the frequency distinguishability of the non-degenerate photon pairs and counteract the quantum state precession governed by the fine-structure splitting.

REFERENCES

[1] P. Senellart, G. Solomon, and A. White. High-performance semiconductor quantum-dot single-photon sources. *Nature Nanotechnology*, 12(11):1026–1039, 11 2017.

[2] L. J. Bissell, C. R. Stroud, and S. G. Lukishova. *Experimental Realization of Efficient, Room Temperature Single-Photon Sources with Definite Circular and Linear Polarizations*. PhD thesis, University of Rochester, 2011.

[3] O. Voskoboynikov, C. P. Lee, and O. Tretyak. Spin-orbit splitting in semiconductor quantum dots with a parabolic confinement potential. *Physical Review B - Condensed Matter and Materials Physics*, 63(16), 4 2001.

[4] T. Kuroda, T. Mano, N. Ha, H. Nakajima, H. Kumano, B. Urbaszek, M. Jo, M. Abbarchi, Y. Sakuma, K. Sakoda, Ikuo Suemune, Xavier Marie, and Thierry Amand. Symmetric quantum dots as efficient sources of highly entangled photons: Violation of Bell's inequality without spectral and temporal filtering. *Physical Review B - Condensed Matter and Materials Physics*, 88(4), 7 2013.

[5] S. Seidl, M. Kroner, A. Högele, K. Karrai, R. J. Warburton, A. Badolato, and P. M. Petroff. Effect of uniaxial stress on excitons in a self-assembled quantum dot. *Applied Physics Letters*, 88(20), 5 2006.

[6] A. Muller, W. Fang, J. Lawall, and G. S. Solomon. Creating polarization-entangled photon pairs from a semiconductor quantum dot using the optical stark effect. *Physical Review Letters*, 103(21), 11 2009.

[7] R. Trotta, J. Martín-Sánchez, J. S. Wildmann, G. Piredda, M. Reindl, C. Schimpf, E. Zallo, S. Stroj, J. Edlinger, and A. Rastelli. Wavelength-tunable sources of entangled photons interfaced with atomic vapours. *Nature Communications*, 7, 1 2016.

[8] M. A.M. Versteegh, M. E. Reimer, K. D. Jöns, D. Dalacu, P. J. Poole, A. Gulinatti, A. Giudice, and V. Zwiller. Observation of strongly entangled photon pairs from a nanowire quantum dot. *Nature Communications*, 5(5298), 10 2014.

[9] X. Ding, Y. He, Z. C. Duan, N. Gregersen, M. C. Chen, S. Unsleber, S. Maier, C. Schneider, M. Kamp, S. Höfling, Chao Yang Lu, and Jian Wei Pan. On-Demand Single Photons with High Extraction Efficiency and Near-Unity Indistinguishability from a Resonantly Driven Quantum Dot in a Micropillar. *Physical Review Letters*, 116(2), 1 2016.

[10] D. M. S. Johnson, J. M. Hogan, S.W. Chiow, and M. A. Kasevich. Broadband optical serrodyne frequency shifting. *Optics Letters*, 35(5), 3 2010.

[11] C. Qin, H. Lu, B. Ercan, S. Li, and S.J.B. Yoo. Single-Tone Optical Frequency Shifting and Nonmagnetic Optical Isolation by Electro-Optical Emulation of a Rotating Half-Wave Plate in a Traveling-Wave Lithium Niobate Waveguide. *IEEE Photonics Journal*, 9(3), 6 2017.

[12] A. Fognini, A. Ahmadi, S. J. Daley, M. E. Reimer, and V. Zwiller. Universal finestructure eraser for quantum dots. *Optics Express*, 26(19), 9 2018.

[13] C.X. Yang, Y.B. Liu, and X.B. Wang. On-demand Entanglement Source with Polarization-Dependent Frequency Shift. *Applied Physics Letters*, 96(20), 9 2009.

[14] D. A. Farías and J.N. Eckstein. Dynamic electrooptic frequency shifter for pulsed light signals. *IEEE Journal of Quantum Electronics*, 41(1):94–99, 1 2005.

[15] A. Yariv and Y. Pochi. *Photonics: Optical Electronics in Modern Communications (The Oxford Series in Electrical and Computer Engineering)*. Oxford University Press, Inc., 2006.

[16] N. Courjal, M.-P. Bernal, A. Caspar, G. Ulliac, F. Bassignot, L. Gauthier-Manuel, and M. Suarez. Lithium Niobate Optical Waveguides and Microwaveguides. In *Emerging Waveguide Technology*. InTech, 11 2018.

5

SPECTROMETER APPLICATIONS WITH SNSPDS

In this chapter we are going to compare three different types of spectrometers, by means of which superconducting single photon detectors can be used as the detection technology. These are the grating spectrometer, the Fabry-Perot and the superconducting single photon detector itself. This chapter introduces as well the principles that have led to the wide deployment of web-based applications and presents two examples custom-made for the specific applications used within this project.

5.1. THE ERA OF WEB-BASED APPLICATIONS

The fast development in the field of Internet of Things (IoT) has accelerated the transition from Desktop Applications to web-based ones. Once the embedded WebServers, integrated into the hardware, appeared on the scene, it seemed natural for the industrial and laboratory environment to opt for devices and instrumentation accessible via the local network and controllable simultaneously. This is the reason why it is common for many instruments nowadays to come equipped with an Ethernet port. The user can then address the instrument with command strings from a remote PC and perform the desired actions.

For embedded WebServers, since the WebServer resides in the hardware, the user can build a WebClient application that opens connections with all devices and simply control the platform by a graphical-user-interface. Since web-browsers are nowadays very standard, WebClient applications, that are designed to run on web-browsers, solve cross-platform compatibility problems arising from different computer environments. Moreover there is no need for the vendor to ship a separate Desktop application along with the instrumentation.

At their early development stage, however, browsers were unable to dynamically react to the user's input and especially to transfer large amount of data in real-time. This is crucial when working with high-performance instruments such as cameras and oscilloscopes for instance, that acquire large amount of data in very short time. The necessity to transfer and visualize huge chunks of complex data in real-time has outdated the Hypertext Transfer Protocol (HTTP), designed to display static content at a slow refreshing rate triggered by user requests. So, how to tackle the issue of big data transfer in the other direction, namely from the Server to the user? To this end a few tools have turned IoT into reality: HTML5 and Javascript together with the latest improvement in socket connection, have enabled the real-time communication between WebServers and WebClients using the so-called "WebSocket protocol".

WebSocket is a protocol build on top of the Transmission Control Protocol (TCP) layer that has been specifically designed to tackle the performance issues of HTTP in real-time bidirectional communication. In fact, WebSocket protocol ensures that while packets are sent over TCP, that is a full-duplex protocol where both the client and the server can send messages simultaneously, the communication uses another messaging frame created by fragmenting large buffer data into small bits. Specifically, each frame contains a header with length, type of message-format and indication whether the transferred frame is the final one.

Moreover, WebSockets is compatible with web browsers. So, it combines the high performance of a close-to-raw TCP socket, ideal for instrument data transfer where the integrity of large chunks of messages is crucial, with the flexibility of web programming. After the "handshake" between WebClient and WebServer is established, multiple connections with clients are handled and messages are sent over in parallel. These connections between the instruments and the user's browser are long lasting and bidirectional. Furthermore, once inside the browser, the developer can make use of powerful tools provided by modern JavaScript frameworks, with libraries such as d3.js for advanced graphics in complex data visualization, and Flot.js which provides high-performance plotting

features ideal for real-time monitoring. Last but not least, the use of web-browsers does not require the payment of license fees to third parties that offer systems engineering software, since all the relevant software is open source.

So, the presence of a sturdy and reliable messaging platform have pushed the realization of industrial applications also facilitated by the advent of Application Programming Interface (API) provided by the vendors. API is just an abstract level in software programming that acts as intermediate between the developer needs and the complexity of operations at the instrument level, namely the lowest "back-end" layer, by providing a simple set of commands. The user can then neglect what is happening "behind the scene" of the instruments control because the API is taking care of everything, and quickly run the experiments.

Below, we will showcase this exciting new technology that we have used to build two different applications: one to control the Fabry-Perot Interferometer for the light modulation experiment and the Single Quantum Iris-S19 spectroscopy system.

5.2. SOFTWARE DEVELOPMENT

In order to acquire the spectra of the modulated light and to perform spectroscopy analysis on Quantum Dots, we developed two software programs that integrated the functionalities of the instruments involved. Three main software tools were used to achieve this task: Tornado [1], WebSockets [2] and ZeroMQ [3]. Only for Fabry-Perot control software we used LabVIEW for the front-end part.

Tornado is a python-based web framework and asynchronous network library developed to handle thousands of open connections simultaneously. It can hold thousands of long living connections and it is convenient to use since it hosts the core program and opens/closes the WebSocket connections once a client requests/disconnects. Its core property is the so-called "event-driven programming". The change of paradigm with respect to previous standard HTTP protocol comes because the flow of the program is determined by events such as user actions, or external events in general. In an event-driven application, the main loop listens for events, and triggers a callback function when one of those events is detected. This "real-time" exchange of input and output data triggered by events necessitate no latency and needs to be bidirectional. In that sense, WebSockets comes as an evolution over the standard HTTP protocol by upgrading these functionalities.

Sketch in fig. 5.1 shows the complete layout of the applications and is divided in three main blocks:

- the *front-end* that receives data from the server side and plots them real-time,
- the *graphical user interface* (GUI) developed in HTML 5 and Javascript and handles the input/output stream of data with the WebServer through WebSockets,
- the *back-end* block made of the WebServer which interacts with the front-end and the Instrument server loop. Here, the Instruments are called to operation by means of their own application programming interface. The API is located into the Instrument Client block that runs in a virtual environment. It is accessed by

means of ZeroMQ, another communication protocol enabling server/client over TCP/IP connection that has low latency and is especially suited to control devices over the local network.

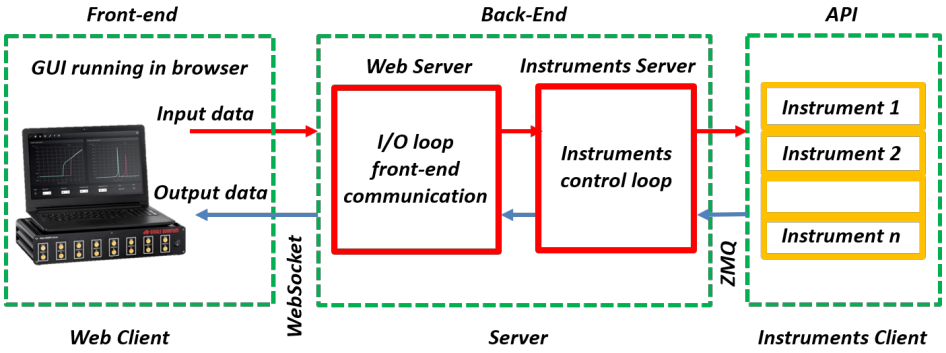

Figure 5.1: Layout of the application. Each layer is in a green box. The front-end with its GUI drives the event-system and handles the input/output stream of data with the WebServer through WebSockets. In the back-end block, the WebServer hosts the Instrument server loop that triggers the API when requested.

5.3. IRIS-S19

This section showcases the Single Quantum Iris-S19 GUI. Iris-S19 is a Czerny-Turner spectrometer ideal for applications such as photon source characterization and correlation measurements, time-resolved and single molecule fluorescence spectroscopy. One example application is reported [4] by Gourgues et al. where the Iris-S19 was used to measure the emission spectrum and correlations of a PbS/CdS Qdot source.

The most convenient feature of the Iris-S19 is that it can be coupled to a superconducting single-photon detector at its exit slit. This happens via previous coupling of the light into single mode fiber. In order to perform time-correlated measurements, the Iris-S19's software enables to optimize the alignment of the beam using a scan function for the grating angle while the SNSPD acquires the emission profile of the emitter. Iris-S19 is equipped with a Kimera 193i spectrometer from Oxford instrument and the native software allows to control the CCD camera and the grating. However, in order to facilitate the alignment process, the communication with the superconducting single-photon detector needs to be integrated. This is why the new Iris-S19's software comes as an upgrade by integrating the communication with the SNSPD's control driver. Iris-S19 can be operated in three different modes: Imaging, Full vertical binning and Scan.

5.3.1. IMAGING MODE

Iris-S19 can be operated in *Imaging mode* where the CCD camera image is directly read out. To read, process and display all the data coming from 1600X200 active pixels we made use of the Library GPU.js [5] that processes the images on the GPU of the computer

and makes the image processing much faster, hence avoiding any lagging and enabling "real-time" data display.

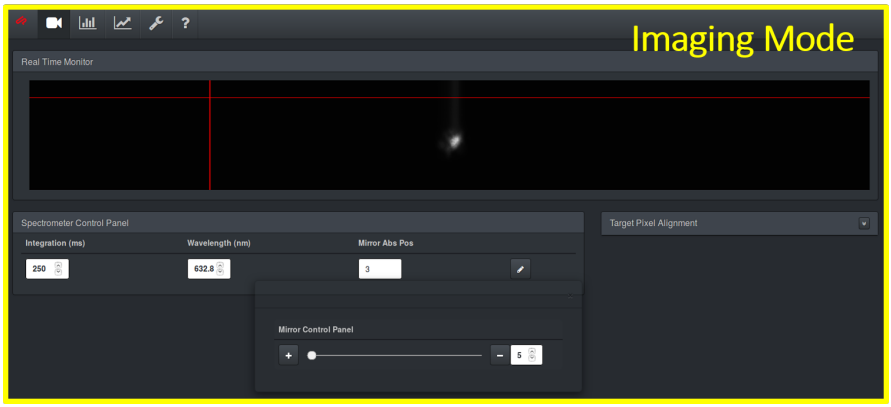

Figure 5.2: Modes of light exiting a multimode fiber from an HeNe laser. The buttons allow to control the camera Integration time, the grating angle and the parabolic mirror for the best focus.

5.3.2. FULL VERTICAL BINNING MODE

In *Full Vertical Binning* mode, the 200 vertical pixels are summed up for each of the 1600 bins to acquire a spectrogram of the signal.

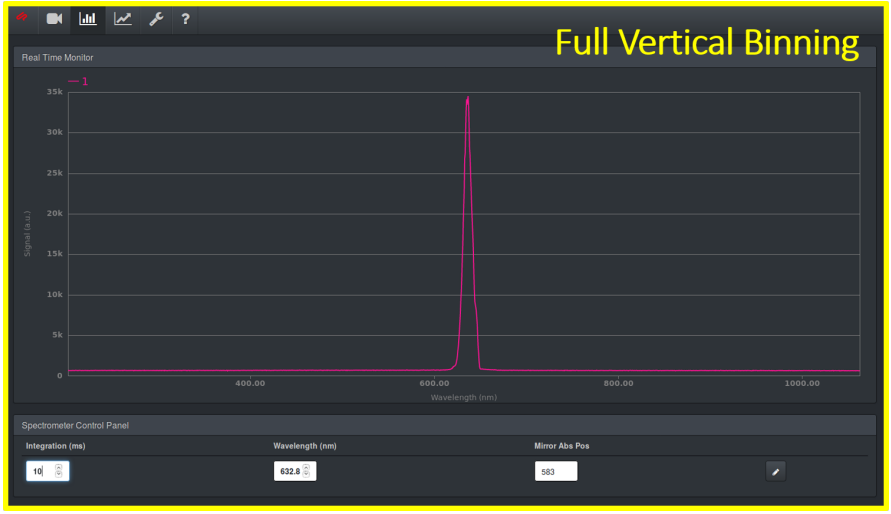

Figure 5.3: Spectrogram of a HeNe laser in Full Vertical Binning mode. Same as in Imaging mode, the buttons control the camera Integration time, grating angle and the parabolic mirror.

5.3.3. SCAN MODE

In *Scan mode* the light is coupled to single-mode fiber and directed towards a SNSPD. Scan mode is used to tune the grating and center it where coupling is at its best. "Coupling is at its best" starts with the knowledge that the CCD camera lies in the conjugate plane of the spectrometer's exit slit. As such, to properly align the beam at center of the exit slit, we must displace the beam spot at the center pixels of the CCD. Then, to enhance the coupling into single-mode fiber, the beam-size profile on the CCD must be minimized. This can be done by fine-tuning the position of the parabolic mirror. Once the system is prepared in such configuration, we can flip the mirror next to the CCD plane and direct the light towards the exit slit. Typically at this point it is advisable to add a system of lenses to focus the light towards a parabolic mirror fiber-coupler.

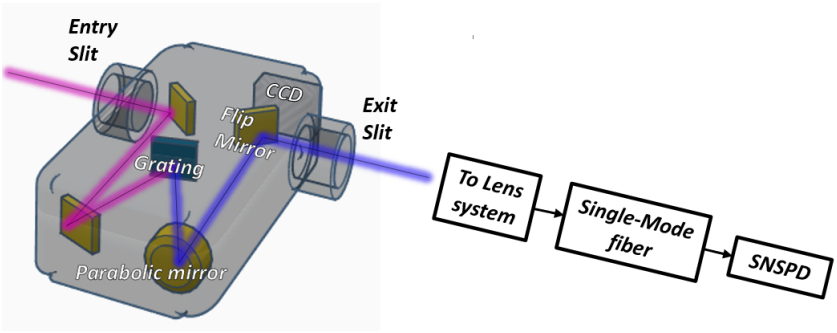

Figure 5.4: Sketch of the Czerny Turner spectrometer when flipped mirror is turned to direct the light towards the CCD conjugate plane.

Photons are then sent to the SNSPD and displayed by the GUI through the connection with the SNSPD driver.

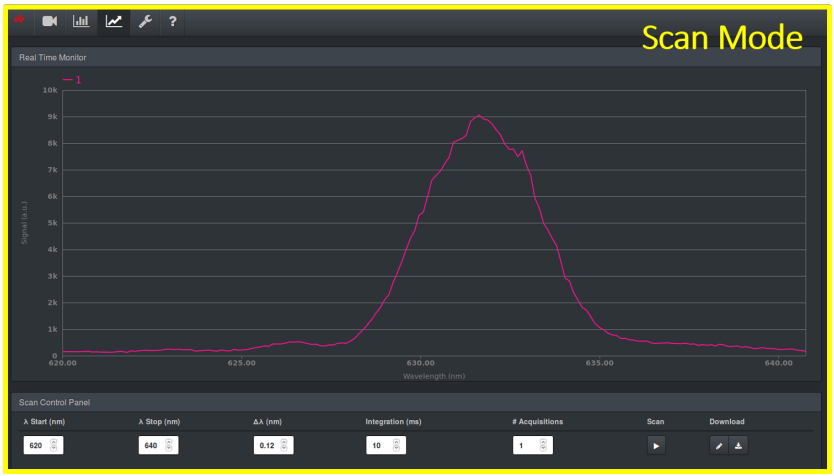

Figure 5.5: Scan of grating position to find the angle of maximum coupling to single mode fiber.

To summarize, the built software allows to connect a spectrometer together with the SNSPD system directly over the internet. This allows to control the measurement setup in any operating system, even with the use of a mobile phone.

5.4. FABRY-PEROT INTERFEROMETER

A Fabry-Perot Interferometer-based tunable filter is an optical cavity made of two parallel reflecting surfaces that are displaced in opposite directions by means of piezoelectric stages. In such a way the optical cavity is modified to let through other wavelengths. Optical waves of specific wavelength can cross the optical cavity only when exact resonance condition is met, namely at wavelengths at which the beam exhibits constructive interference after one round-trip due to the reflection. The Fabry-Perot Interferometer possesses different qualities compared to the previous spectrometer solutions, namely a much higher spectral resolution in the order of a few picometers at the cost of narrower optical bandwidth. It is typically used for high resolution measurements or noise filtering given its great wavelength selection properties. Because of these properties, this device was used to measure the outcome of sawtooth phase-modulation which is indeed expected to produce a wavelength shift in the order of several picometers at the center wavelength of 1550 nm.

This section showcases the Fabry-Perot Tunable filter software specially made to control its driver board and displays the collected photocurrent generated by the photons impinging on an InGaAs photodiode. The driver board creates a triangular RF wave that is fed to the piezoelectric stages and sets the parallel reflecting surfaces in motion. As the triangular wave descends and rises, several phase modulated peaks are measured by the oscilloscope. These peaks always occur at a specific time during rise and descend. By knowing the exact *Free Spectra Range* we can convert time into frequency shift. Data collection and broadcast are provided by a RaspberryPi that hosts the WebServer and handles communication with all devices involved. The RaspberryPi was configured to work over WiFi to avoid using an Ethernet cable. This way, the setup is easily movable around the lab. Its complete sketch is given in fig. 5.6.

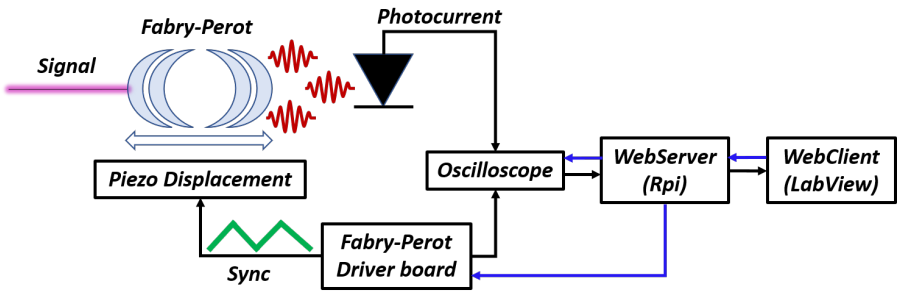

Figure 5.6: Sketch of the Fabry-Perot tunable filter setup. Signal is filtered by the movable mirrors driven by a triangular wave (green signal) generated by the driver board. The light impinges onto the InGaAs photodiode that develops a photocurrent measured by the oscilloscope. The driver board has another sync connected to the oscilloscope. Data transmission and devices control is provided by the RaspberryPi through WebSocket protocol. Blue arrows highlight backward stream during simultaneous bidirectional communication.

The Fabry-Perot has a Free Spectral Range of 497.01 GHz and 0.476 GHz resolution. All electrical signals, namely the sync and the photodiode current, are acquired by a cheap oscilloscope with 8 Ksps. Data is processed in the WebServer and sent to LabVIEW over the WebSocket protocol. Besides controlling the scan rate of the filter, the GUI (see fig. 5.7) enables to play with the voltage offset and peak-to-peak scan voltage in order to find the emission wavelength range. Since the sampling rate is rather low, we also added a knob to tune the oscilloscope delay in order to seek the emission together with a knob to change the oscilloscope timebase to zoom out. The Free spectral Range was provided by the manufacturer and it was used to convert time scale into frequency.

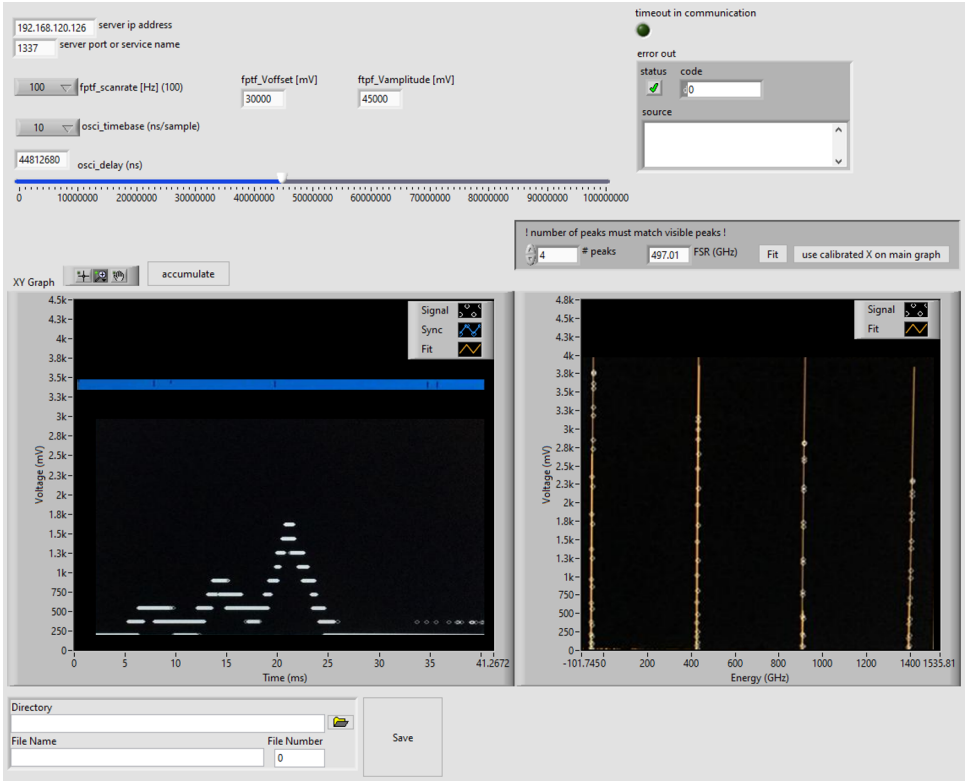

Figure 5.7: GUI built with LabVIEW. Left panel shows real time measurement of sine wave modulation and right panel shows the peaks over 3 FSRs and is used to calibrate the device.

Picture 5.8 shows the physical infrastructure controlled by the application. In the top view we see the input fiber going into a polarization controller before entering the Fabry-Perot tunable filter. The output is coupled to the InGaAs photodiode whose electrical signal is read-out by the Oscilloscope (middle layer in the lateral view). In the lowest layer we find the driver board of the interferometer that generates a triangular wave fed to the piezos.

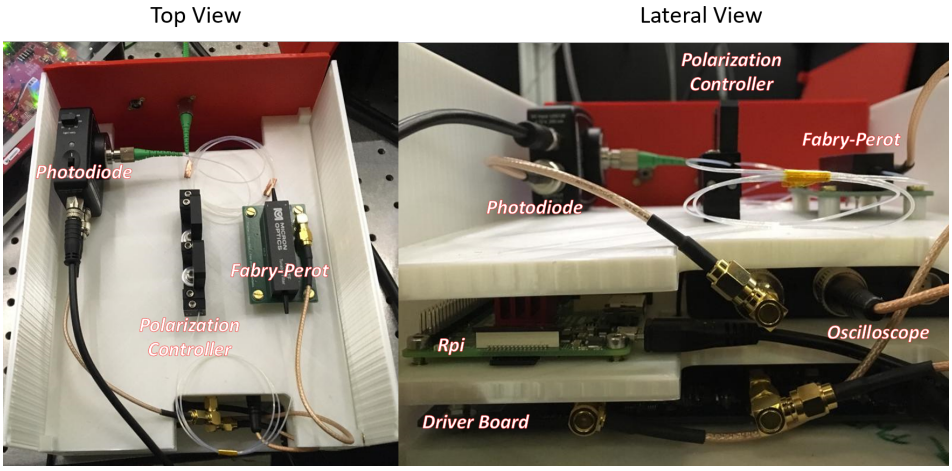

Figure 5.8: Picture of the instrumentation used to acquire the phase modulated spectra.

5.5. SNSPD SPECTROMETER

There is another approach to measure the energy of a photon, namely with the superconducting single photon detector itself. In this last section we will show the energy resolution capabilities of SNSPDs and discuss its possible utilization as a compact wavelength-multiplexing-free spectrometer that can achieve 1 nm spectral resolution.

5.5.1. SPECTRAL RESOLUTION

Several publications [6, 7] reported the photon-wavelength dependence on the efficiency curve versus bias-current of a superconducting-single photon detector. The most interesting consequence of wavelength dependence is the shift of the inflection point of the efficiency curve. This is the bias current value for which the curve changes its curvature.

To understand this fact we must think in terms of energy deposited in the superconducting film. In fact, heuristically, we can imagine that to reach the same level of detection probability when lower energy photons impinge on the detector, a higher bias current is needed to compensate for this energy "gap" and vice versa. According to this reasoning we can expect that there is at least a linear relationship between the photon energy and the bias current.

To confirm this heuristic reasoning we ran efficiency measurements on a SNSPD by acquiring count-rate versus bias-current sweeps with a tunable laser for 21 different wavelengths. We performed two sweeps, one for a wider wavelength interval with bigger step sizes and another one over a narrower interval where the wavelength had varied by only 1 nm. Then we fitted the curves with a sigmoid function that statistically models the detection probability. The results are shown in fig. 5.9.

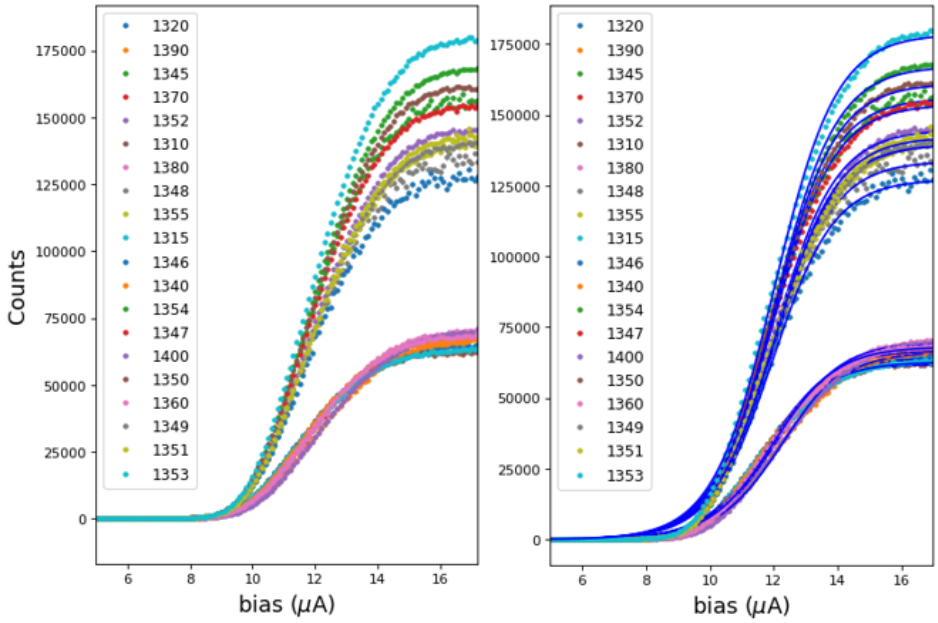

Figure 5.9: **(Left)** Raw data of the efficiency curves. **(Right)** Fitted data with a sigmoid function. The two sweeps were run with a different count rate which leads to a mismatch in peak counts value.

Looking beyond the peak efficiency, that is mainly related to the SNSPD cavity, fig. 5.9 demonstrates that the inflection point does indeed shift depending on the photon wavelength. This is better visualized in fig. 5.10 which also verifies that the shift has a linear relationship with the bias level confirming our initial hypothesis.

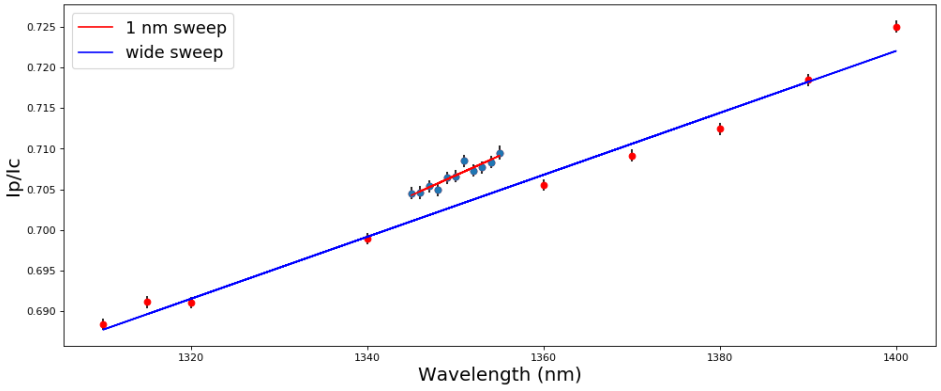

Figure 5.10: Ip/Ic stands for inflection point value divided by the superconducting threshold current. Linear dependence is demonstrated by linear regression for both sweeps. The two dataset were acquired with different photon count-rates which have led to a variation in superconducting threshold current with a consequent vertical offset in the Ip/Ic ratio.

The linear behavior is confirmed for both sweeps by a linear regression which yield a R^2 value of 0.89 and 0.98 for the 1 nm and the wide sweep respectively. We notice a vertical offset between the two sweeps. We argue that this is due to the different photon count-rates used for the two experiments which lead to a change in superconducting threshold current. For the 1 nm sweep the slope of the linear fit is 4.67 x 10^{-4} nm^{-1}. This value differs from the value extracted from the other fit that is 3.66 x 10^{-4} nm^{-1}. We think that this mismatch occurs mainly because of the laser fluctuation during the measurement. However, it is advisable to acquire more data in order to gain more statistical sampling and for a more meaningful evaluation.

With these findings we foresee the possibility to design a spectrometer without the need for wavelength multiplexing optics such as a grating or a Fabry-Perot interferometer. We could then reduce the complexity and size of the optical hardware. However, besides the broadband response capabilities of the SNSPD, we still miss a readout scheme that could make use of multiple pixels biased at different levels. Multiple pixels will give us more information about the spectrum of the light source that can be processed computationally.

5.6. CONCLUSION

The advent of WebSockets in 2011 together with other web-based open-source frameworks made the bidirectional communication between the server and the client to come true. WebSockets also allow the streaming of large chunks of binary data to and from web-browsers to fulfill all the requirements to build highly interactive web-applications that can even outperform their desktop counterparts. We have reported here two examples that showcase this modern and very flexible approach of interfacing scientific instrumentation with web-based technology. Besides software engineering on spectrometer devices, we have also shown that superconducting single photon detectors are good candidates to replace bulky optical devices based on wavelength multiplexing and allow for fine spectral resolution, namely of 1 nm or even lower.

As a final remark, it is interesting to compare the resolution of this new-concept device with the grating spectrometer equipped in the Iris-S19. Let's give some numbers. The Kimera 193i spectrometer enables a resolution of 0.21 nm with a 1200 l/mm grating or a resolution of 0.96 nm with a 300 l/mm grating. The preliminary research on the SNSPD spectrometer have shown comparable performances to this last grating option, with the additional advantage that the SNSPD spectrometer does not require any wavelength multiplexing optics. With this in mind we can foresee possible applications for this new-concept device when easiness and readiness of operation are required without sacrificing on resolution.

REFERENCES

[1] Tornado Web Server. Retrieved from https://www.tornadoweb.org.

[2] WebSockets. Retrieved from https://websockets.readthedocs.io/en/stable/.

[3] ZeroMQ. Retrieved from https://zeromq.org/.

[4] L. Elsinger, R. Gourgues, I.E. Zadeh, J. Maes, A. Guardiani, G. Bulgarini, S.F. Pereira, S.N. Dorenbos, V. Zwiller, Z. Hens, and D. Van Thourhout. Integration of Colloidal PbS/CdS Quantum Dots with Plasmonic Antennas and Superconducting Detectors on a Silicon Nitride Photonic Platform. *Nano Letters*, 19(8), 7 2019.

[5] GPU.js. Retrieved from https://github.com/gpujs/gpu.js/.

[6] A. G. Kozorezov, C. Lambert, F. Marsili, M. J. Stevens, V. B. Verma, J. A. Stern, R. Horansky, S. Dyer, S. Duff, D. P. Pappas, A. Lita, M. D. Shaw, R. P. Mirin, and Sae Woo Nam. Quasiparticle recombination in hotspots in superconducting current-carrying nanowires. *Physical Review B - Condensed Matter and Materials Physics*, 92(6), 8 2015.

[7] A. G. Kozorezov, C. Lambert, F. Marsili, M. J. Stevens, V. B. Verma, J. P. Allmaras, M. D. Shaw, R. P. Mirin, and S. W. Nam. Fano fluctuations in superconducting nanowire single-photon detectors. *Physical Review B*, 96(5), 2 2017.

6

CONCLUSION AND FUTURE WORK

This thesis has shown how semiconductor quantum dots can generate single photon pairs that show very high entanglement. Despite their limitations in terms of entanglement level of the photon pairs, we still envision a future where Qdots are deployed in quantum photonic applications. Indeed, we have seen that such limitations can be mitigated by further development in single photon detection technology, especially regarding time resolution, and by correcting the properties of the emitted photons with commercial electro-optical devices. The good quality in electrical signal generation provided by cost-effective radio-frequency equipment may represent the route towards the solution of the challenges faced by Qdots, namely an easy and universally valid fine-structure splitting compensation scheme that is also scalable to all the Qdots on a sample. The rationale is to outperform the current post-growth techniques which do not act at the single Qdot level and cannot anyway fully correct for the quantum state precession. Hereon, we present a brief summary of results achieved during this PhD thesis and provide a possible outlook for future research in this field.

6.1. ACHIEVEMENTS

During this PhD work, we have once more confirmed that the model proposed by Fognini et al. in [1] consistently predicts the entanglement evolution for an AlGaAs Qdot when pumped with two-photon resonant excitation. We could infer that the behavior of these solid state emitters only depends on the exciton precession, especially considering that AlGaAs Qdots do possess significant nuclear spin. It follows that the interaction between the charge carriers involved in the emission and the nuclei is not a relevant dephasing mechanism within the radiative decay time of the exciton. We have also shown that although there is no dephasing occurring during the decay of the excitons in the investigated Qdot, reaching perfect entanglement does still remain a challenge. These findings have pushed us to research on two possible workarounds.

First, we acted at the detection system level with the aim of increasing the measured degree of entanglement. In fact, according to our model the concurrence is lowered by the timing jitter of the detection system. In chapter 3, we have demonstrated the benefits of a new generation of cryogenic amplifiers that outperform the room temperature ones given the reduction in Johnson thermal noise. We used a Vector Network Analyzer to investigate the scattering parameters and properly engineered the radio-frequency matching to the input and output termination of the amplifier. After accurately tuning the elements in the network we validated our hypothesis by performing jitter measurements and witnessed a consistent reduction in timing-jitter. However, given that the physical time resolution will always be finite and never reach zero, an entanglement measurement can never have a steady value of one over the whole radiative lifetime.

This reasoning have moved us towards the second research direction, namely to engineer the properties of the exciton and biexciton emission by changing their frequencies. This approach has the major benefit to avoid difficult post-growth techniques usually acting at the sample level such as uniaxial strain induced by piezoelectric materials [2, 3], electric field induced quantum confined Stark effect [4], or magnetic field induced Zeeman shifts [5]. To this end we discussed that engineering single photons through phase modulation is a valuable alternative to achieve fine-structure compensation. We have given a hint of this by testing the current commercial phase modulation technology available and performing frequency translation experiments on a laser source. The measured spectra show that sawtooth phase modulation can reach the target despite the technological limitations, but further improvements are needed. Thus, we have proposed a possible solution to overcome undesired phase modulation using the well-established phase-locked loop technology. Upgrading the radio-frequency amplification stage and synchronizing the light emission to the "sweet spot" where the sawtooth has almost perfect linearity will improve photon frequency translation towards the desired energy. Despite the necessary development in quantum repeater technology, with this thesis we can foresee at least the feasibility in the realization of a quantum photonic infrastructure where the photons are fully entangled enabling the exchange of photon qubits in long-range quantum communication.

6.2. OUTLOOK

Based on the results obtained, I can envision some research possibilities in this field. The first applies to research in single photon detection technology especially for superconducting single photon detectors. Until now, SNSPDs present the best capabilities in terms of time resolution if compared to photomultipliers tubes and avalanche photodiodes. It was shown in several articles [6, 7] that this competitive advantage can be enhanced by shrinking the size of these devices to less than 10 μm. Fabricating even smaller SNSPDs will hinder the ability of these devices to detect the photons with high efficiency. There is in fact a limiting value chosen for the diameter of the SNSPDs which results in a the trade-off between efficiency and time resolution. Nevertheless, there are two possible solutions to this trade-off, namely the realization of smaller multipixel detectors and novel approaches to enhance light coupling into smaller core fibers. Of course, both approaches comes with limitations: in the first case relative to the increasing number of radio-frequency readout channels and, in the second, relative to the light coupling losses.

Optical resonant excitation techniques are crucial to observe the best possible quality of single, indistinguishable and entangled photons [8]. Once again, the thesis work confirmed the beneficial impact of two-photon resonant excitation for dephasing free Qdot emission. However, the increasing experimental complexity in the realization of quantum photonic platforms, that require a lot of bulk optical components, needs to be tackled to achieve reliable and scalable quantum communication. Integrated quantum photonics is most likely the viable approach to face these problems since all the building blocks are placed on a single chip. Although integrated optical components, other than single photon sources, such as electro-optic phase shifters [9] and single-photon detectors [10, 11] have been proven effective in various experiments, a whole-circuit with single-photon generation, manipulation and detection on a single chip has not been realized yet. This can be explained by the fact that single photons, until now, are preferably generated using resonant optical pumping of plain Qdot structures without auxiliary structures around it.

First, there is a relevant background emission arising from the excitation of these structures and from other shells which is detrimental in providing the best single-photon purity. We have also discussed how fluctuating fields in the surroundings of the emitter can generate dephasing and worsen the photon distinguishability. This effect can be partially quenched to a certain extent by incorporating the source in a microcavity [12]. However, unlike optical π pulse excitation, which allows direct control of the exciton and biexciton population resonantly flipping the state of quantum emitter with "the push of a button", the electrical excitation process lacks of a similar excitation mechanism. Attempts with resonant electrical injection [13], made by tuning the applied bias to have the carriers in the doped regions resonant with the s-shell energy level in the Qdot, allowed to suppress the background light but did not demonstrate coherent control of the quantum state. One possible solution may be to combine the resonant injection with latest scheme of "Active reset" of the radiative exciton-biexciton cascade proposed by Müller et al. in [14], which relies on a high-frequency pulsed excitation to control the biexciton population. Similarly to two-photon resonant excitation where the

pulse width plays a critical role in biexciton population inversion and exciton population suppression, it is imaginable that the electrical radio-frequency pulse width in a future "resonant active reset" experiment may augment the entanglement level. So, further development in radio-frequency engineering is very much desired to realize tunable-width pulse generators in the order of the picosecond range.

Further research in this field is very interesting and impactful because we need to try to disclose the power of the electrical excitation scheme to finally bring quantum optics into the era of lab-on-a-chip.

Finally, as far as concerns phase modulation technology for fine-structure splitting compensation, we witnessed in our experiments a significant transmission loss of about 5 dB by the phase modulator. Given the hard task of fabricating bright single photon sources based on Qdot technology, electro-optical modulators with low coupling losses are needed. Commonly this electro-optic devices present propagation losses of a few dB/cm due the mode mismatch between the single-mode fiber and the waveguide. Recently, an on-chip $LiNbO_3$ bilayer inversely tapered mode size converter was demonstrated to improve the mode match, and the fiber-to-chip coupling losses to be as low as 1.7 dB per facet at 1550 nm [15]. A recent publication [16] of an efficient and cost-effective technique to properly taper a standard single-mode fiber to match the mode of $LiNbO_3$ waveguide demonstrated coupling losses down to 1.32 dB, but further improvements in this field are certainly desirable. For what concerns the radio-frequency generation equipment, the well established phase-locked loop technology along with fast digital-to-analog conversion capabilities appear to be promising in fine-structure splitting compensation schemes. Utilizing devices with broad bandwidth will certainly help to boost the fine-structure splitting compensation scheme towards a mature technology.

Even though the technology is not yet mature enough to readily enable quantum communication on large scale, I look forward to and wish to see further effort in this field of research to finally turn this technology into an industrial wide-scale application that society can benefit from.

REFERENCES

[1] A. Fognini, A. Ahmadi, M. Zeeshan, J. T. Fokkens, S. J. Gibson, N. Sherlekar, S. J. Daley, D. Dalacu, P. J. Poole, K. D. Jöns, V. Zwiller, and M. E. Reimer. Path to perfect photon entanglement with a quantum dot. *arXiv preprint arXiv:1710.10815*, 10 2017.

[2] J. Martín-Sánchez, R. Trotta, A. Mariscal, R. Serna, G. Piredda, S. Stroj, J. Edlinger, C. Schimpf, J. Aberl, T. Lettner, Johannes Wildmann, Huiying Huang, Xueyong Yuan, Dorian Ziss, Julian Stangl, and Armando Rastelli. Strain-tuning of the optical properties of semiconductor nanomaterials by integration onto piezoelectric actuators. *Semiconductor Science and Technology*, 33(1), 1 2018.

[3] S. Seidl, M. Kroner, A. Högele, K. Karrai, R. J. Warburton, A. Badolato, and P. M. Petroff. Effect of uniaxial stress on excitons in a self-assembled quantum dot. *Applied Physics Letters*, 88(20), 5 2006.

[4] A. Muller, W. Fang, J. Lawall, and G. S. Solomon. Creating polarization-entangled photon pairs from a semiconductor quantum dot using the optical stark effect. *Physical Review Letters*, 103(21), 11 2009.

[5] R. M. Stevenson, R. J. Young, P. Atkinson, K. Cooper, D. A. Ritchie, and A. J. Shields. A semiconductor source of triggered entangled photon pairs. *Nature*, 439(7073):178–182, 1 2006.

[6] M. V. Sidorova, A. V. Divochiy, Y. B. Vakhtomin, and K.V. Smirnov. Ultrafast superconducting single-photon detector with a reduced active area coupled to a tapered lensed single-mode fiber. *Journal of Nanophotonics*, 9(1):093051, 9 2015.

[7] N. Calandri, Q. Y. Zhao, D. Zhu, A. Dane, and K. K. Berggren. Superconducting nanowire detector jitter limited by detector geometry. *Applied Physics Letters*, 109(15), 10 2016.

[8] D. Huber, M. Reindl, J. Aberl, A. Rastelli, and R. Trotta. Semiconductor quantum dots as an ideal source of polarization-entangled photon pairs on-demand: A review. *Journal of Optics*, 20(7), 7 2018.

[9] R. Noe and D.A. Smith. Integrated-optic rotating waveplate frequency shifter. *Electronics Letters*, 24(21), 10 1988.

[10] L. Elsinger, R. Gourgues, I.E. Zadeh, J. Maes, A. Guardiani, G. Bulgarini, S.F. Pereira, S.N. Dorenbos, V. Zwiller, Z. Hens, and D. Van Thourhout. Integration of Colloidal PbS/CdS Quantum Dots with Plasmonic Antennas and Superconducting Detectors on a Silicon Nitride Photonic Platform. *Nano Letters*, 19(8), 7 2019.

[11] W. H.P. Pernice, C. Schuck, O. Minaeva, M. Li, G. N. Goltsman, A. V. Sergienko, and H. X. Tang. High-speed and high-efficiency travelling wave single-photon detectors embedded in nanophotonic circuits. *Nature Communications*, 3, 12 2012.

[12] Yating Lin, Yongzheng Ye, and Wei Fang. Electrically driven single-photon sources. *Journal of Semiconductors*, 40(7), 2019.

[13] M. J. Conterio, N. Sköld, D. J.P. Ellis, I. Farrer, D. A. Ritchie, and A. J. Shields. A quantum dot single photon source driven by resonant electrical injection. *Applied Physics Letters*, 103(16), 10 2013.

[14] Jonathan R. A. Müller, R. Mark Stevenson, Joanna Skiba-Szymanska, Ginny Shooter, Jan Huwer, Ian Farrer, David A. Ritchie, and Andrew J. Shields. Active reset of a radiative cascade for entangled-photon generation beyond the continuous-driving limit. *Physical Review Research*, 2(4), 11 2020.

[15] Lingyan He, Mian Zhang, Amirhassan Shams-Ansari, Rongrong Zhu, Cheng Wang, and Marko Loncar. Low-loss fiber-to-chip interface for lithium niobate photonic integrated circuits, 2 2019.

[16] Ni Yao, Junxia Zhou, Renhong Gao, Jintian Lin, Min Wang, Ya Cheng, Wei Fang, and Limin Tong. Efficient light coupling between an ultra-low loss lithium niobate waveguide and an adiabatically tapered single mode optical fiber. *Optics Express*, 28(8):12416, 4 2020.

List of Publications

3. Jin Chang, Johannes W. N. Los, Jaime Oscar Tenorio-Pearl, Niels Noordzij, Ronan Gourgues, **Antonio Guardiani**, Julien R. Zichi, Silvania F. Pereira, H. Paul Urbach, Val Zwiller, Sander N. Dorenbos, Iman Esmaeil Zadeh, *Detecting Infrared Single Photons with Near-Unity System Detection Efficiency*, arXiv e-prints arXiv:2011.08941 (2020).

2. Iman Esmaeil Zadeh, Johannes W. N. Los, Ronan B. M. Gourgues, Jin Chang, Ali W. Elshaari, Julien Romain Zichi, Yuri J. van Staaden, Jeroen P. E. Swens, Nima Kalhor, **Antonio Guardiani**, Yun Meng, Kai Zou, Sergiy Dobrovolskiy, Andreas W. Fognini, Dennis R. Schaart, Dan Dalacu, Philip J. Poole, Michael E. Reimer, Xiaolong Hu, Silvania F. Pereira, Val Zwiller, Sander N. Dorenbos, *Efficient Single-Photon Detection with 7.7 ps Time Resolution for Photon-Correlation Measurements*, ACS Photonics **7**, 7 (2020).

1. Lukas Elsinger, Ronan Gourgues, Iman E. Zadeh, Jorick Maes, **Antonio Guardiani**, Gabriele Bulgarini, Silvania F. Pereira, Sander N. Dorenbos, Val Zwiller, Zeger Hens, Dries Van Thourhout, *Integration of Colloidal PbS/CdS Quantum Dots with Plasmonic Antennas and Superconducting Detectors on a Silicon Nitride Photonic Platform*, Nano Letters **19**, 8 (2019).